

INVESTIGATIONS INTO PHASE EFFECTS  
FROM DIFFRACTED GAUSSIAN BEAMS FOR  
HIGH-PRECISION INTERFEROMETRY

by  
DEEPALI LODHIA

A thesis submitted to the  
University of Birmingham  
for the degree of  
DOCTOR OF PHILOSOPHY

Astrophysics and Space Research Group  
School of Physics and Astronomy  
College of Engineering & Physical Sciences  
University of Birmingham  
May 2013

UNIVERSITY OF  
BIRMINGHAM

**University of Birmingham Research Archive**

**e-theses repository**

This unpublished thesis/dissertation is copyright of the author and/or third parties. The intellectual property rights of the author or third parties in respect of this work are as defined by The Copyright Designs and Patents Act 1988 or as modified by any successor legislation.

Any use made of information contained in this thesis/dissertation must be in accordance with that legislation and must be properly acknowledged. Further distribution or reproduction in any format is prohibited without the permission of the copyright holder.



# Abstract

Gravitational wave detectors are a new class of observatories with the aim of detecting gravitational waves from cosmic sources. All-reflective interferometer configurations have been proposed for the next generation of gravitational wave detectors, with conventional transmissive optics replaced by diffractive elements, thereby reducing thermal issues associated with power absorption. However, diffraction gratings introduce an additional phase noise which creates more stringent conditions for alignment stability. In order to determine whether all-reflective interferometers are a viable alternative, further investigations are required.

A suitable mathematical framework using Gaussian modes is required for analysing the alignment stability using diffraction gratings. Such a framework was successfully created, whereby small displacements of the beam (or grating) are modelled using a modal decomposition technique. It was confirmed that the original modal-based model does not contain the phase changes associated with grating displacements. Experimental tests were carried out to measure the phase of beams diffracted by a grating, verifying that the phase of a diffracted Gaussian beam is in fact independent of the beam shape. Phase effects from grating diffraction were further examined using a rigorous time-domain simulation tool.

The findings from the research presented here show that the perceived phase difference is based on an intrinsic change of coordinate system within the modal-based model, and that the extra phase can be added manually to the modal expansion.

This thesis provides a well-tested and detailed mathematical framework that can be used to develop simulation codes to model more complex layouts of all-reflective interferometers with diffractive components.



## Acknowledgements

I feel extremely fortunate to have had Andreas Freise as my supervisor to guide me through the perils of being a PhD student and a Graduate Technologist. His ability to see right through me meant there was nowhere to hide, which was probably a good thing. His mentoring over the past eight years has transformed me, and important life-lessons were learnt along the way. I sincerely thank Andreas for all his help, and more importantly for believing in me.

The post-docs deserve huge thanks, starting with Frank Brückner, whose support and kind words helped me jump the final hurdle in writing up this thesis. Also to Keiko Kokeyama and Simon Chelkowski for their tremendous help in the lab and making things actually work, and Ludovico Carbone for his assistance with Advanced LIGO work.

I was lucky to be surrounded by an amazing and varied group of postgraduates to whom I am very grateful. Paul Fulda, Mengyao Wang and Antonio Perreca - discussions with them were always fun and insightful, and they had the ability to bring sense and order into a world of complete chaos (usually caused by me in the lab). Huge thanks to Daniel Brown - without his genius simulations, I probably would never have completed my research. Thanks to Jonathan Hallam for keeping me company in the lab, and also to Charlotte Bond, Chiara Mingarelli and Konstantinos Kolokythas, who turned many social gatherings into rather more interesting and often lively events.

On the technical side of my work, I express my gratitude to Mike Cruise who gave me this opportunity to study in the first place. Also thanks to Alberto Vecchio, who proved to be an excellent Advanced LIGO project manager - between the constant whirlwind of project deadlines on an international scale and almost drowning in

---

what seemed like an infinite sea of screening devices, I like to think I didn't cause him too much distress. A big thank you to Stuart Aston, who had good faith in my abilities and from whom I learnt a great deal. I also wish to acknowledge the technical staff: David Hoyland (who always put a smile on my face), Steve Brookes, Anthony Page, John Bryant and Ron Cutler. A mention also to David Stops, whose constant supply of laptops meant that I had no excuse not to work.

A special thanks goes to my office-mate and fellow grad tech Matthew Holder, who started this journey with me and was a pillar of support. We shared plenty of laughter and tears, and despite the pressures of our work schedules, he always kept me focused on the end goal.

Thanks to my very good friends Crystal Tse, Jas Purewal and Linda Lee for the occasional and much-needed escape from the world of academia, and my Taekwondo family for providing the perfect stress-buster during my studies and allowing me to let off steam and excess energy (legally), as well as for putting up with my random rants about invisible lasers and imaginary numbers.

I am deeply grateful to my parents for their incredible support that kept me going over the years, who appreciated all the hard work that went into this thesis and who couldn't be more proud. And a massive thanks to my brother, Dipesh Gorecha, for always making me laugh and forget about the grown-up world. I offered many times to swap my PhD studies with his GCSEs and A-levels, but he was having none of it.

Finally to Saf Jeevanjee, who was there from the beginning to the end, witnessed the highs and lows, and continuously encouraged and supported me in so many ways. Thank you for sharing this crazy adventure - I couldn't have done it without you.

Thank you all - this has been a journey I'll never forget.

---

*I dedicate this thesis to the memory of Master Suh Ki Young,  
who showed me the path to true strength and wisdom.*



## Statement of originality

This thesis presents research work carried out at the University of Birmingham between October 2005 and May 2013.

Chapter 1 provides an introduction to the subject of gravitational wave detection and includes a brief overview of gravitational waves and their sources, the concept of interferometric detection and the noise sources which limit the sensitivity of current detectors. This chapter proceeds to a discussion of thermal effects due to power absorption in optical elements, followed by a description of diffraction gratings and associated phase effects in Gaussian beams.

Chapter 2 describes an analytical framework which is used to examine the phase changes in a displaced Gaussian beam after grating diffraction. Two methods of displacement are considered: firstly through a geometric beam displacement, and secondly a modal technique by adding a higher-order mode. The absence of the intrinsic phase factor from the analytical model is also confirmed.

Chapter 3 details a table-top experiment designed to compare the interference patterns between zero-order and first order modes, and thereby establish that the phase of a beam after grating diffraction is independent of its beam shape.

Chapter 4 introduces a rigorous time-domain simulation tool developed by Daniel Brown at the University of Birmingham. The simulation tool was used by me to investigate the diffraction of Gaussian beams and compare phase measurements of beams displaced geometrically or modally. The conditions required in order to correctly obtain phase measurements which include the intrinsic phase factor are also discussed.

Chapter 5 reports a concluding summary based on the research presented here.

---

The work described in Chapters 2-4 and the concluding results are presented in D. Lodhia, F. Brückner, L. Carbone, P. Fulda, K. Kokeyama, and A. Freise, *Phase effects in gaussian beams on diffraction gratings*, Journal of Physics: Conference Series **363** 012014 (2012), and

D. Lodhia, D. Brown, F. Brückner, L. Carbone, P. Fulda, K. Kokeyama, and A. Freise, *Phase effects due to beam misalignment on diffraction gratings*, Optics Express (2013) (to be published).

Chapter 6 presents an outline of the research carried out as part of the Advanced LIGO Suspensions Working Group, and in particular on the development and manufacture of the BOSEM devices at the University of Birmingham. An overview of the test mass suspension system and key features of the upgraded BOSEMs are provided. This chapter also includes an evaluation of the flag mount tests, a report on the preparation of the infra-red LEDs and photodiodes, and a description of the testing procedures carried out on the part-assembled and fully-assembled BOSEMs.

Appendix A depicts the output of beam-shapes and lens properties using a mode-matching tool for Gaussian beams, a measured profile of a collimated beam, and a Matlab script used to determine new Gaussian beam parameters after diffraction by a grating, as stated in Chapter 3.

Appendix B describes the concept of a feedback control system using the Pound-Drever-Hall technique as detailed in [1].

Appendix C presents electronic schematics for the servo, which I fabricated and used as part of the experiment.

Appendix D provides a computation to determine the waist size and waist position of a Gaussian beam in the first-diffraction order using only the radius of curvature and beam spot size parameters from a zeroth-diffraction order.

---

Appendix E firstly illustrates a CAD drawing of the magnetic-mounted flag, an improved feature in the design of the BOSEM. The second section conveys data specifying the number of BOSEMs to be delivered by the University of Birmingham for installation in the Advanced LIGO detectors. The third section contains a script which imports the BOSEM log files (created from the automated testing described in Chapter 6) and converts them into spreadsheets. This script was primarily adopted from [2].



# Contents

<b>Contents</b>	<b>i</b>
<b>List of Figures</b>	<b>v</b>
<b>Glossary</b>	<b>ix</b>
<b>1. INTRODUCTION</b>	<b>1</b>
1.1. Theory of gravitational waves and their origin . . . . .	2
1.1.1. Characteristics of gravitational waves . . . . .	2
1.1.2. Fundamental sources . . . . .	4
1.2. Gravitational wave detection . . . . .	6
1.2.1. Principles of interferometry . . . . .	7
1.2.2. Current ground-based detectors . . . . .	12
1.3. Noise sources and sensitivity . . . . .	16
1.3.1. Seismic and Newtonian noise . . . . .	18
1.3.2. Quantum noise . . . . .	20
1.3.3. Thermal noise and limitations . . . . .	22
1.4. Thermal effects due to power absorption . . . . .	27
1.4.1. Thermal lensing . . . . .	28
1.5. Diffractive elements in interferometry . . . . .	30
1.5.1. Diffraction gratings . . . . .	31

## Contents

---

1.5.2. All-reflective interferometer configurations . . . . .	33
1.5.3. Grating-related phase effects in plane waves . . . . .	34
1.5.4. First attempts to mitigate phase noise . . . . .	40
1.5.5. An analytical framework for grating-related phase noise in simulations . . . . .	43
1.6. Structure of this thesis . . . . .	44
<b>2. ANALYTICAL FRAMEWORK FOR DIFFRACTED GAUSSIAN BEAMS</b>	<b>46</b>
2.1. Gaussian optics . . . . .	47
2.1.1. Gaussian beam profile . . . . .	47
2.1.2. Fundamental and higher order modes . . . . .	49
2.2. Beam displacement . . . . .	51
2.2.1. Modal decomposition . . . . .	53
2.3. Beam comparison . . . . .	55
2.3.1. Identifying the phase components . . . . .	55
2.4. Grating diffraction . . . . .	58
2.4.1. Beam displacements within a grating period . . . . .	59
2.5. Comparison of electric field amplitudes . . . . .	61
2.6. Analytical results . . . . .	63
<b>3. EXPERIMENTAL DEMONSTRATION OF PHASE-MODE INDEPEN-</b> <b>DENCY</b>	<b>66</b>
3.1. Blazed gratings . . . . .	67
3.2. A Mach-Zehnder setup to observe phase effects . . . . .	69
3.2.1. Mode cleaner . . . . .	69
3.2.2. Mach-Zehnder, grating path . . . . .	71
3.2.3. Mach-Zehnder, piezoelectric transducer path . . . . .	74
3.3. Cavity resonance stabilisation techniques . . . . .	75
3.3.1. Analogue cavity resonance stabilisation . . . . .	76

## Contents

---

3.3.2. Mode-cleaner control loop . . . . .	79
3.3.3. Mach-Zehnder control loop . . . . .	82
3.4. Dual-mode locking technique . . . . .	84
3.4.1. Method of dual-mode locking . . . . .	85
3.4.2. Dual-mode fringe pattern . . . . .	86
3.5. Experimental results . . . . .	88
<b>4. TIME-DOMAIN SIMULATION FOR GRATING DIFFRACTION</b>	<b>90</b>
4.1. Introduction to the finite-difference time-domain tool . . . . .	92
4.1.1. Concept of the simulation tool . . . . .	93
4.2. Main parameters and defining the optical layout . . . . .	95
4.2.1. Waist position discrepancy . . . . .	97
4.3. Phase change for grating/beam displacement . . . . .	100
4.3.1. Grating displacement . . . . .	102
4.3.2. Beam displacement . . . . .	105
4.4. Modal decomposition . . . . .	106
4.4.1. Mode combination . . . . .	107
4.4.2. Translation of reference planes . . . . .	109
4.5. Grating/beam displacement vs. modal decomposition . . . . .	111
4.6. Simulation results . . . . .	113
<b>5. CONCLUSIONS</b>	<b>116</b>
<b>6. ADVANCED LIGO BOSEM DEVELOPMENT AND TESTING</b>	<b>118</b>
6.1. Suspension system . . . . .	119
6.1.1. BOSEMs . . . . .	123
6.2. Magnetic-mounted flag test . . . . .	124
6.3. Infra-red LED and photodiode preparation . . . . .	128
6.3.1. Burn-in testing . . . . .	129

## Contents

---

6.3.2. Screening . . . . .	131
6.4. BOSEM testing procedure . . . . .	133
6.4.1. Part-assembled testing . . . . .	134
6.4.2. Fully-assembled testing . . . . .	134
6.4.3. BOSEM characterisation . . . . .	140
<b>A. Beam profile and parameters</b>	<b>143</b>
A.1. Mode-matching the beam . . . . .	143
A.2. Beam characterisation . . . . .	146
A.3. Matlab script to determine new beam parameters after grating diffraction . . . . .	147
<b>B. Pound-Drever-Hall laser frequency stabilisation</b>	<b>150</b>
B.1. Modulation concept . . . . .	150
B.2. Carrier and sidebands . . . . .	151
B.3. Power in the reflected beam . . . . .	153
B.4. Obtaining the error signal . . . . .	157
B.4.1. High frequency modulation . . . . .	157
B.4.2. Low frequency modulation . . . . .	158
<b>C. Electronic schematics for the servo</b>	<b>161</b>
<b>D. Parameter computation using the sagitta</b>	<b>166</b>
<b>E. BOSEM testing and distribution</b>	<b>173</b>
E.1. Cross-section of the magnetic-mounted flag . . . . .	173
E.2. BOSEM count . . . . .	175
E.3. Script to import BOSEM data log files . . . . .	177
<b>Bibliography</b>	<b>180</b>



# List of Figures

1.1. Visual effect of a gravitational wave . . . . .	3
1.2. A simple Michelson laser interferometer . . . . .	8
1.3. Topology of an advanced interferometric gravitational wave detector .	9
1.4. Schematic of the Advanced LIGO detector . . . . .	14
1.5. Predicted noise curve for Advanced LIGO . . . . .	17
1.6. Increased power absorption in transmissive optics . . . . .	29
1.7. Diffraction of light caused by a reflective diffraction grating . . . . .	32
1.8. Diffraction gratings in cavity couplers . . . . .	34
1.9. All-reflective interferometer in a non-Littrow configuration . . . . .	35
1.10. Changes in optical path length due to grating displacement . . . . .	37
1.11. Phase noise due to grating displacement . . . . .	39
1.12. Schematic for 2-port and 3-port grating cavities . . . . .	41
1.13. Sensitivity measurements for grating cavity displacement . . . . .	42
2.1. Gaussian beam profile . . . . .	49
2.2. Coordinate change for a misaligned Gaussian beam . . . . .	52
2.3. Phase profile for beam displacement within a grating period . . . . .	60
2.4. Comparison of factors for increasingly displaced beams . . . . .	62
2.5. Relative difference of factors for increasingly displaced beams . . . . .	64
3.1. Diffraction in blazed gratings . . . . .	68

## *List of Figures*

---

3.2. Schematic of a grating Mach-Zehnder interferometer . . . . .	70
3.3. Orientation of the blazed grating . . . . .	73
3.4. Modulation around a resonance peak from a Fabry-Perot cavity. . . .	77
3.5. Feedback control loop using a linear cavity . . . . .	78
3.6. Feedback control system for the triangular mode cleaner . . . . .	80
3.7. Error signal and resonance peaks for the mode cleaner . . . . .	81
3.8. Feedback control system for the Mach-Zehnder setup . . . . .	82
3.9. Error signal and interference fringes for the Mach-Zehnder arms . . .	84
3.10. Zero-order and first-order mode beam shapes . . . . .	86
3.11. Mode cleaner locked to the square-wave ramp signal . . . . .	87
3.12. Interference fringes from the dual-mode lock . . . . .	88
4.1. Cell array of the simulation space . . . . .	93
4.2. Cell updates during simulation . . . . .	94
4.3. Diffraction pattern for a TEM <sub>00</sub> beam . . . . .	97
4.4. Beam waist size discrepancy due to diffraction . . . . .	98
4.5. The sagitta parameter . . . . .	100
4.6. Diffraction pattern for a TEM <sub>00</sub> beam with corrected waist positions	101
4.7. Phase change in a TEM <sub>00</sub> beam . . . . .	103
4.8. Diffraction pattern for a TEM <sub>10</sub> beam . . . . .	104
4.9. Phase change in a TEM <sub>10</sub> beam . . . . .	106
4.10. Comparison of modal decomposition methods . . . . .	108
4.11. Modal phase change - reference planes for one mode shifted . . . . .	110
4.12. Modal phase change - reference planes for both modes shifted . . . .	111
4.13. Comparison of phase behaviour for all cases . . . . .	112
4.14. Effects of shifting and stationary reference planes . . . . .	114
6.1. Structure of a quadruple suspension system. . . . .	120
6.2. Actuator and sensor locations on the suspension. . . . .	122

## *List of Figures*

---

6.3. Design model of a BOSEM. . . . .	123
6.4. Design model of a magnetic flag within a BOSEM. . . . .	124
6.5. Magnetic flag with magnetic and Vacsealed mounts. . . . .	125
6.6. Schematic of the magnetic-mounted flag. . . . .	126
6.7. Weight suspension and displacement testing. . . . .	127
6.8. Properties of the infra-red LED and and photodiode. . . . .	129
6.9. Infra-red LED burn-in test setup. . . . .	130
6.10. Screening jig setup. . . . .	131
6.11. Distribution of infra-red LED intensities. . . . .	133
6.12. The part-assembled coilformer and fully-assembled BOSEM. . . . .	134
6.13. Testing the part-assembled BOSEM. . . . .	135
6.14. High-voltage testing for the fully-assembled BOSEM. . . . .	136
6.15. Automated test equipment for testing the fully-assembled BOSEM. . . . .	137
6.16. Display of measurements from the automated test equipment. . . . .	138
6.17. Output file from the automated test equipment. . . . .	139
6.18. Distribution of intensities, resistances and inductances from testing. . . . .	142
A.1. Mode-matching into the mode cleaner . . . . .	144
A.2. Mode-matching the circular beam to an astigmatic beam . . . . .	145
A.3. Measured beam profile after the mode cleaner . . . . .	146
B.1. Feedback control relative to the signal phase . . . . .	152
B.2. PDH error signal for high and low modulation frequencies . . . . .	160
C.1. Servo schematic 1/4 . . . . .	162
C.2. Servo schematic 2/4 . . . . .	163
C.3. Servo schematic 3/4 . . . . .	164
C.4. Servo schematic 4/4 . . . . .	165
D.1. Visual description of the sagitta . . . . .	167

*List of Figures*

---

E.1. BOSEM count. . . . .	176
---------------------------	-----

## Glossary

ATE	Automated test equipment
BOSEM	Birmingham optical sensor and electro-magnetic actuator
BS	Beam-splitter
CCD	Charge coupled device
EOM	Electro-optic modulator
ET	Einstein Telescope
ETM	End test mass
FDTD	Finite-difference time-domain
FFT	Fast-Fourier transform
FSR	Free spectral range
FWHM	Full-width half-maximum
GW	Gravitational wave
HG	Hermite-Gauss
HV	High voltage
IRLED	Infra-red light-emitting diode
ITM	Input test mass
LIGO	Laser interferometer gravitational wave observatory
MC	Mode cleaner
MZ	Mach-Zehnder
PD	Photodetector/Photodiode
PDH	Pound-Drever-Hall
PRM	Power recycling mirror
PZT	Piezoelectric transducer
SRM	Signal recycling mirror
TEM	Transverse electro-magnetic

# Chapter 1.

## INTRODUCTION

The existence of gravitational waves (GWs) first emerged from Albert Einstein's theory of General Relativity (GR) in 1916 [3]. The changing gravitational field around accelerating bodies generates gravitational radiation in the form of ripples in the curvature of space-time. These gravitational waves travel at the speed of light isotropically from their source. Despite being the weakest of the four fundamental forces in nature, gravity offers an important advantage in that its long range allows it to penetrate further than electromagnetic radiation. The interaction of gravitational waves with matter is extremely weak, and so they retain much of the information from their sources, unlike electromagnetic radiation. The detection of gravitational waves would not only confirm GR, but also signify a new branch of gravitational wave astronomy; the unique nature of GWs could open up an entirely new window through which we can observe the universe, and in particular the very early universe.

Indirect observations, such as the findings by Hulse and Taylor in 1975 of a pulsar in a binary system which was losing energy through gravitational radiation [4], provide strong evidence of the existence of gravitational waves. However, a direct observation

has not been possible so far, and the difficulty lies in the fact that the interaction of gravitational waves with matter is extraordinarily weak. While there has been an overwhelming effort over the decades to develop increasingly sensitive gravitational wave detectors and push the boundaries of science, the hunt for a direct detection of gravitational waves still continues.

Section 1.1 presents an overview of the nature of gravitational waves and potential sources. Section 1.2 describes the latest topology of a ground-based interferometric gravitational wave detector and key features. The limiting noise sources affecting the sensitivity of the instrument are considered in Section 1.3, while thermal effects due to power absorption are examined in further detail in Section 1.4. In Section 1.5, the topic of diffraction gratings is reviewed and their use in all-reflective configurations for detectors. The concept of the *intrinsic phase factor* is introduced, used to describe the phase changes a diffracted beam experiences due to beam misalignment (for distances within a grating period), and previous efforts to reduce grating-related phase noise. Lastly, the aims of the thesis are addressed - these include the development of an analytical framework incorporating grating-related phase effects for use in interferometry simulation tools and investigations into the missing intrinsic phase factor from modal-based simulation techniques.

## 1.1. Theory of gravitational waves and their origin

### 1.1.1. Characteristics of gravitational waves

An object responds to a passing gravitational wave by alternating length perturbations orthogonal to the direction of wave propagation. This effect is demonstrated more clearly with a ring of free particles in Figure 1.1: when a GW travels along

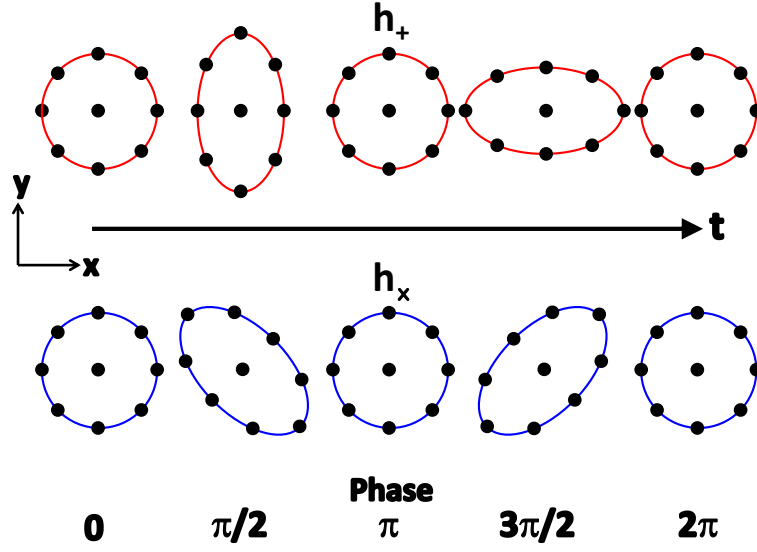


Figure 1.1.: A gravitational wave passing through a ring of free particles causes the arrangement to stretch and squeeze alternately along the vertical and horizontal for the  $h_+$  polarisation (red), and diagonally for the  $h_\times$  polarisation (blue), during one period. The phase is also shown along the bottom.

the  $z$ -axis (perpendicular to the plane of particles), spacetime is squeezed along the  $x$ -direction and stretched in the  $y$ -direction during the first half of a gravitational period. As the wave continues into the second half of the period and the phase rotates by  $\pi$ , spacetime expands in the  $x$ -axis and contracts along the  $y$ -axis. The overall result is an oscillatory motion in the arrangement of the particles.

Two polarisations exist for gravitational waves: plus polarisation,  $h_+$ , and cross polarisation,  $h_\times$ , and the distinction between the two is that the axes of motion in the latter is rotated by  $45^\circ$ , clearly seen in Figure 1.1. It is interesting to note that the area bounded by the particles remains unchanged during the oscillations.

The strength of a gravitational wave is measured in terms of the strain,  $h$ , felt by



the object it encounters [5]:

$$h = \frac{2\delta L}{L}, \tag{1.1}$$

where  $L$  is the original length of the object and  $\delta L$  is the absolute change in length. The measured strain of a gravitational wave diminishes as  $1/r$  for a source at distance  $r$ , and the strain expected from the strongest sources is generally of the order  $h = 10^{-21}$ .<sup>1</sup> An overview of these gravitational wave sources is given in the next section.

### 1.1.2. Fundamental sources

The fact that gravitational waves induce such a weak response means that our efforts are concentrated on astrophysical sources which emit the strongest waves. The single-sign nature of mass (which can only be positive) means that gravitational waves are emitted as a result of its quadrupole moment, whereas dipole radiation does not exist<sup>2</sup> [7]. In other words, any accelerating body will radiate gravitational waves, provided that the mass distribution is not spherically or cylindrically symmetric - this can include non-uniform spinning stars, binary systems and exploding supernovae. Ground-based instruments aim to detect frequencies as low as 1 Hz up to a few kilohertz [8]. Within this frequency range, the most promising astrophysical sources for gravitational waves can be categorised into four types: *continuous*, *inspiral*, *burst* and *stochastic* [9].

---

<sup>1</sup>Assuming an inspiral binary system of two neutron stars, where the stars are separated by 90 km, have a combined mass of  $2.8 M_{\odot}$  and at a distance of 15 Mpc, at a frequency of 100 Hz [6].

<sup>2</sup>According to general relativity.

### **Continuous wave sources**

These are continuous gravitational waves with slowly evolving frequencies, originating from non-axisymmetric spinning neutron stars (pulsars) or a combination of white dwarf, neutron star and black hole binary systems in orbit (before merging). Although gravitational waves of this type are generated over a long period of time and are subsequently weak, monitoring these signals for longer durations can allow for improved signal-to-noise ratios [10].

### **Inspiral**

Gravitational waves emitted from a binary system carry away energy, causing the two compact objects to inspiral, and the faster they evolve, the higher the frequency and strength of GW emission. Up until the moment of coalescence, the rising frequency and amplitude of the GWs produce a ‘chirp’ signal, and it is during the final stage of the merger that the GW frequencies lie within the range of detection. Due to the characteristics of this waveform and the distribution of compact binaries in the Universe, ground-based detectors are most likely to observe gravitational wave signals from inspiral sources [10], with a predicted strain in the order of  $h = 10^{-23}$  [11].

### **Burst sources**

Burst sources describe unexpected and abrupt releases of gravitational radiation. These can occur in supernova explosions during non-symmetrical core collapse, and possibly even gamma ray bursts. Gravitational waves from burst sources are unstructured and therefore much more difficult to model and detect since they occur at

random and for very short periods of time. The expected strain from these sources could reach  $h = 5 \times 10^{-22}$  [11].

### **Stochastic sources**

A cosmic background of stochastic gravitational radiation may exist as a remnant of the Big Bang, analogous to the cosmic microwave background (CMB). This stochastic background would also have contributions from a combination of continuous, inspiral and burst sources resulting from unresolved astrophysical events. Due to their weakly interacting nature with matter, any gravitational waves detected from the stochastic background may provide clues about the nature of the early Universe, some  $10^{-34}$  seconds after the Big Bang, whereas the CMB was produced 300,000 years after the Big Bang [12]. Strains detected from stochastic sources are approximated to be  $h = 2.4 \times 10^{-25}$  [13].

The predicted levels of strain presented in this section give a sense of the immensely tiny effects of gravitational waves, even for strong sources. In the next section we present the concept of gravitational wave detectors and concentrate on the efforts to optimise the design of ground-based instruments.

## **1.2. Gravitational wave detection**

In order to improve the likelihood of observing gravitational waves, we require a sufficiently large enough detector to better increase the signal - the longer the length of the instrument, the larger the change in length will transpire according to Equation (1.1).

Monochromatic laser light is the most suitable device to measure gravitational waves, seeing as any physical measuring tool will itself experience the effects of stretching and squeezing. Michelson interferometers are an ideal topology for gravitational wave detectors as the L-shaped arms of the instrument maximises the compression and expansion effects of a gravitational wave - the measurement of the relative length of orthogonal arms is well-suited to the quadrupole nature of the waves. The relative arm lengths can be measured, and any change may indicate the presence of gravitational waves. Described here is an outline of the interferometer design, however a more useful discussion can be found in *Pitkin et al.* [14].

### 1.2.1. Principles of interferometry

Figure 1.2 shows a simple laser Michelson interferometer which is an intrinsic part of a gravitational wave detector. A laser beam with a fixed carrier frequency,  $\omega_0$ , is split into two identical beams by a 50/50 beamsplitter (BS), each of which travel along the interferometer arms of approximately equal length. The mirrors reflect the beams back along the arms to meet and interfere at the beamsplitter, and any interference signal is detected at the output by a photodetector (PD).

In the absence of gravitational waves and for arms of equal length, the interfering beams cancel each other and no signal is observed. If a gravitational wave were to pass through the detector (orthogonal to the plane of the arms), one arm would experience a shortening in length while the other experienced an elongation, and a signal is detected.

This is an over-simplified example of a gravitational wave detector - the expected change in the arm lengths is equivalent to a thousandth of the diameter of a proton, and therefore any instrument capable of detecting gravitational waves must be

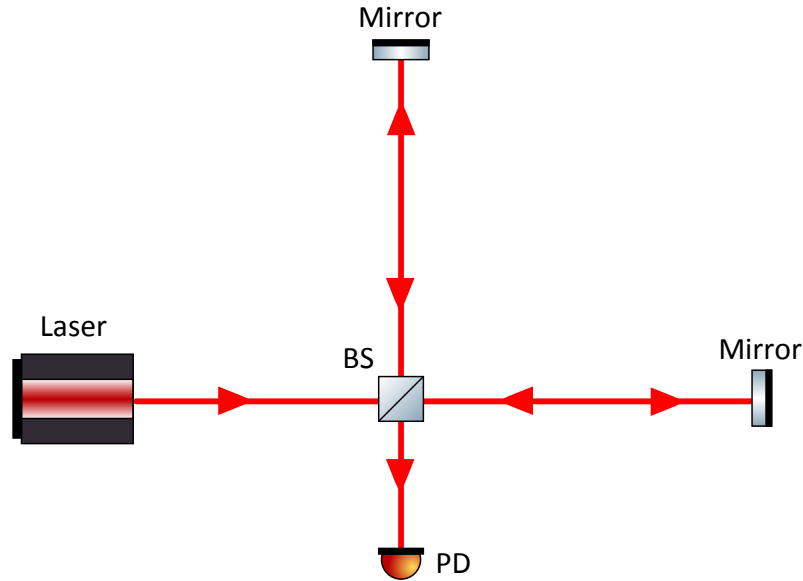


Figure 1.2.: A simple Michelson laser interferometer. Two identical laser beams from a beamsplitter (BS) travel along the interferometer arms, reflect off mirrors and recombine at the BS to form an interference signal, detected by the photodetector (PD).

immensely sensitive, stable and efficient. This is achieved by the addition of a number of important components to this core interferometer design, namely the mode cleaner, Fabry-Perot cavities and power/signal recycling, as illustrated in Figure 1.3 and which are reviewed below.

## Mode cleaners

The laser beam usually consists of a mixture of transverse electromagnetic (TEM) modes, each with slightly varying frequencies and beam shapes - not only does this lead to frequency instabilities thus affecting the ability of the detector to lock to a single frequency in the optical cavities, but the interference contrast of the intersecting beams at the BS is reduced. Instead, the beam passes through a cavity known as a *mode cleaner* (MC) before entering the main interferometer [15], as

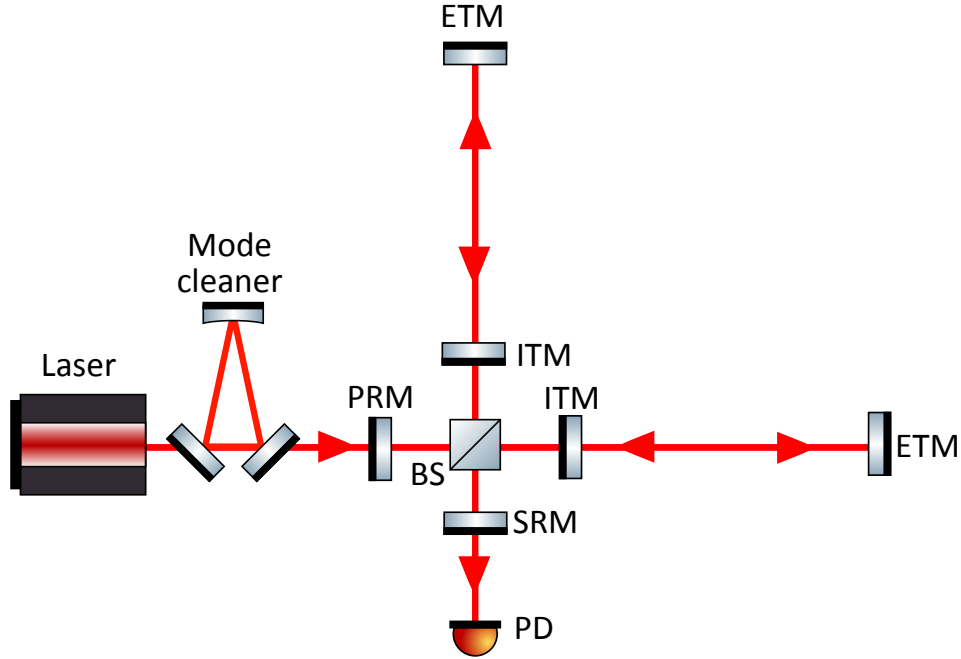


Figure 1.3.: General layout of an advanced interferometric gravitational wave detector. A mode cleaner removes higher order modes in the laser beam. Following the beamsplitter (BS) are the interferometer arms consisting of input test masses (ITMs) and end test masses (ETMs) to create Fabry-Perot arm cavities. The inclusion of a power recycling mirror (PRM) and signal recycling mirror (SRM) helps to avoid light wastage.

shown in Figure 1.3. Tiny adjustments to the optical path length within the MC causes different frequencies, and therefore different modes, to resonate inside. The MC effectively ‘cleans’ the laser beam by reflecting higher-order modes and allowing only a specific mode frequency to exit, and therefore a pure and stable  $\text{TEM}_{00}$  Gaussian beam can be obtained. The quality and alignment of the output beam and cavity stability is defined by the properties of the MC mirrors. A further description of MCs is provided in Section 3.2.1.

## Fabry-Perot arm cavities

As mentioned at the beginning of this section, longer detector arms will result in a larger change in absolute length (as indicated by Equation 1.1). Ideally, detectors would have arms hundreds or even thousands of kilometres long<sup>3</sup>, however this is impractical - due to the curvature of the Earth, the increased pitch angle of the end test masses would also increase the coupling of vertical motion into the longitudinal motion of the mirrors. Ground-based detectors are therefore currently limited to arm lengths of a few kilometres, with details specified in Section 1.2.2.

The arms could instead be folded in on themselves, such as the GEO600 detector (Section 1.2.2), to create path lengths twice as long as the physical arm lengths. An even more effective method is to include an additional mirror in each arm just after the BS, superimposing the optical paths to create *Fabry-Perot cavities* [8]. These cavities are represented by the *input test masses* (ITMs) and the *end test masses* (ETMs), in Figure 1.3. The objective is to enable the light to bounce back and forth between the ITMs and the ETMs to increase the number of round-trips of the photons during interactions with a gravitational wave, thereby virtually increasing the arm length of the detector. For a more quantitative understanding, consider a search for gravitational wave signals at 1 kHz (see Figure 1.5 for the detection range). The gravitational waves would have a wavelength in the order of  $10^5$  m, and consequently each gravitational wave cycle has an interaction with the detector on a timescale of approximately 1 msec. This requires around 50 ‘bounces’ of each photon in a 3 km length arm cavity.

Furthermore, the multiple round-trips of the photons eventually lead to a considerable build-up in laser power within the arm cavities. Increased laser power not

---

<sup>3</sup>For a gravitational wave with a frequency of 100 Hz, the ideal arm length would be 750 km, providing a photon round-trip of 1500 km.

only helps to amplify gravitational wave signals, but also reduces shot noise (see Section 1.3.2). Using the arm cavities in the example given above, an initial laser power of only a few kilowatts would be required to reach detectable strain sensitivity levels (as opposed to an input laser power in the order of megawatts for a simple Michelson interferometer without Fabry-Perot arm cavities [14]).

### Power and signal recycling

The detector arms are normally set such that destructive interference occurs at the output; in other words, the detector is locked to the dark fringe of the interference pattern. The output PD is said to be at the ‘dark port’, and in this state, all of the recombined light is in fact travelling back towards the laser. The inclusion of a *power recycling* (PR) mirror in the path of the input laser beam before the BS creates a PR cavity between the PR mirror and the rest of the interferometer, as indicated in Figure 1.3. As with the Fabry-Perot cavities, the PR cavity experiences a build-up in laser power, further enabling reduction in the shot noise. For correctly chosen parameters and mirror transmissions, laser power can be further reduced from an order of kilowatts down to 10-100 W, and still generate kilowatts of light power at the BS [14].

Gravitational wave signals at frequency  $\Omega$  will cause length changes in the arm cavities, creating sideband signals around the carrier frequency with  $\omega_0 \pm \Omega$ . In contrast to the carrier light field, these sidebands form constructive interference at the output port, due to their phase relations. These signals are extremely weak, but the insertion of a *signal recycling* (SR) mirror before the output PD will reflect these signals back into the arms, where they can circulate back and forth between the cavities. This allows for a longer interaction with the gravitational wave signal, and the resonating sidebands increase in power. A signal recycling cavity is formed



between the SR mirror and the interferometer, as shown in Figure 1.3. The reflectivity of the SR mirror, and thus the finesse of the SR cavity, controls the extent to which the signals are amplified and the narrowing of the detection bandwidth. The length tuning of the SR cavity determines the frequency at which the centre of the detection bandwidth sits [14].

The concept of ground-based gravitational wave detectors is detailed further in the following section.

### 1.2.2. Current ground-based detectors

Gravitational wave detection is undertaken by a huge international collaboration with institutions from around the world. Since 2002, long-baseline gravitational wave detectors have been in operation, however many are currently undergoing upgrades from first generation to second generations detectors. The Michelson interferometer forms the central basis of the design of all current ground-based detectors.

*Virgo*, a French and Italian joint effort [16, 17], is a detector with 3 km long arms and is situated in Cascina, Italy; modifications are underway for *Advanced Virgo*. *GEO 600* is a German-British detector [18, 19], located in Germany near Sarstedt, with arm lengths of 600 m. The arms contain no cavities and are in fact delay lines, folded up on themselves so that each arm is 1200 m long in total. The Japanese cryogenic detector, *KAGRA* (Kamioka Gravitational Wave Telescope), previously known as LCGT (Large Cryogenic Gravitational Wave Telescope) [20, 21], is due to be built underground at the Kamioka mine with arms 3 km long.

LIGO (Laser Interferometer Gravitational Wave Observatory) [22] is an international collaboration based in the U.S. and consists of three instruments. Two detectors are

co-located in Hanford, Washington, at the LIGO Hanford Observatory (LHO) - one has arm lengths of 4 km (LHO 4K or H1) and the other with 2 km (LHO 2K or H2). The third resides in Livingston, Louisiana, at the LIGO Livingston Observatory also with 4 km long arms (LLO 4K or L1).

LIGO began its first science run (S1) in 2002. In 2009 the detector entered an intermediate phase as *enhanced LIGO*, having undergone some modifications. 2010 saw the last science run (S6), before the first generation detector was shut down and the installation of *Advanced LIGO* commenced. Advanced LIGO and Advanced Virgo are scheduled to begin operation in 2014 for joint science runs [23, 24], and KAGRA will join them in 2018 [21].

Improvements to the so-called ‘initial’ LIGO towards Advanced LIGO are currently underway, including plans to move the H2 detector to India and increasing the arms to 4 km as part of the proposed LIGO-India project[25, 26]. Due to my involvement with the Advanced LIGO suspensions group, and in particular my contribution to the development of the Advanced LIGO BOSEMs (see Chapter 6), the framework of this thesis will be relevant specifically to the Advanced LIGO detector rather than ground-based detectors in general, unless specified otherwise. The noise sources considered in Section 1.3 are in accordance to the predicted performance of Advanced LIGO. The concept of Advanced LIGO as a second-generation detector is discussed next.

## **Advanced LIGO**

The main features of the Advanced LIGO gravitational wave detector are summarised here and are illustrated in Figure 1.4, but further particulars are described in [27] and [28].

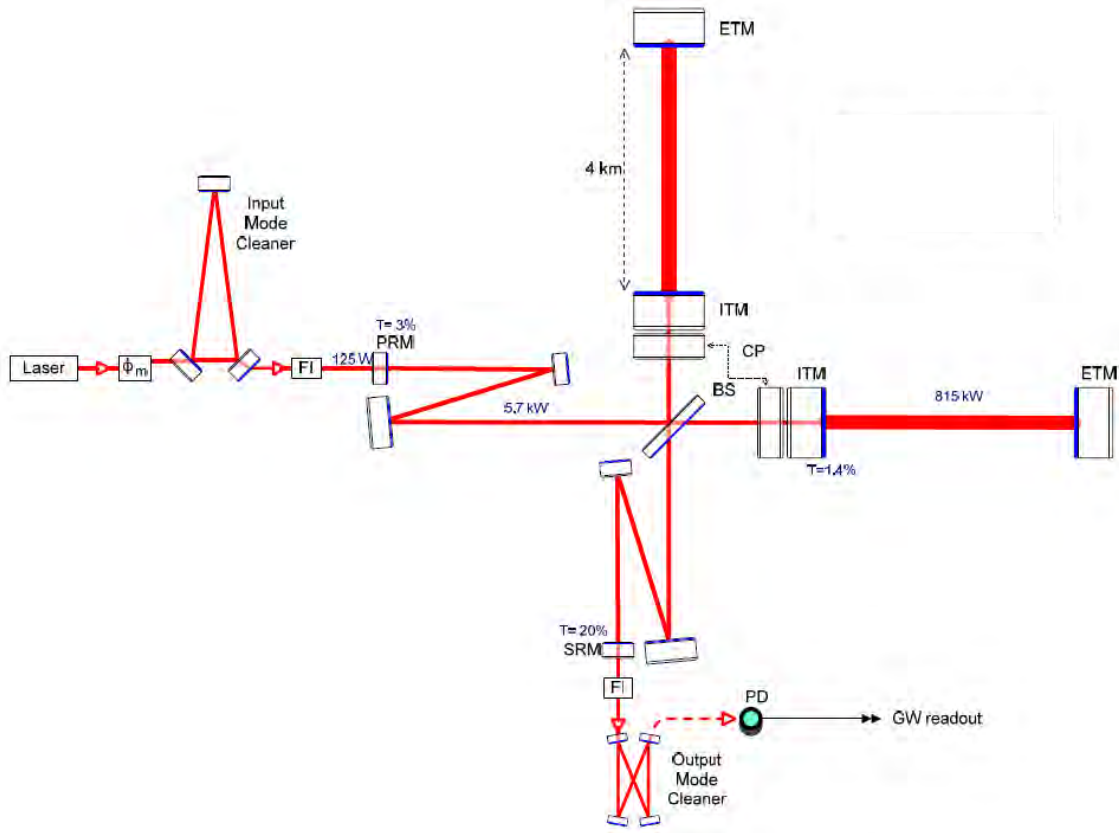


Figure 1.4.: General schematic of the Advanced LIGO detector [28]. The new additions include a higher laser power, signal recycling mirror (SRM), output mode cleaner, larger input and end test masses (ITM and ETM respectively), compensation plates (CP) for thermal lensing and a DC readout system. Other components shown are: power recycling mirror (PRM), faraday isolator (FI), beamsplitter (BS) and output photodetector (PD). Transmission values for certain mirrors and light power in various sections are also indicated.

### *Detector infrastructure*

The current LIGO detectors are located in remote areas away from cities. Each instrument is entirely enclosed in a vacuum system (H1 and H2 lie alongside each other and share the same vacuum housing) to reduce residual gas noise [29]. The detector will be able to operate over a wider frequency range, spanning 10 Hz to just under 10 kHz.

*Laser system and configuration*

A Nd:YAG laser with a wavelength of 1064 nm will provide a power of 180 W (increased from 10 W in initial LIGO), expected to generate a light power of around 850 kW in the arm cavities, as seen in Figure 1.4. A signal recycling mirror (SRM in Figure 1.4) will be introduced to the pre-existing power recycling scheme, and is designed for wide-band sensitivity centred around 100 Hz. At this frequency, signal recycling will enable Advanced LIGO to reach noise strain levels of  $3 \times 10^{-24} \text{ Hz}^{-1/2}$ . Instead of heterodyne detection, homodyne detection (DC readout) will be employed to reduce noise couplings, although this adds the need for an additional output mode cleaner [30], situated between the SRM and output PD in Figure 1.4. Techniques involving squeezed light are presently being tested on the H1 detector, and may potentially be implemented as part of the Advanced LIGO upgrade [31].

*Optics and suspensions*

The test masses made from fused silica will have a diameter of about 32 cm and a mass of 40 kg - larger and heavier than those in initial LIGO to cope with the increased radiation pressure noise from the high laser power (see Section 1.3.2), and with finer polished surfaces and improved coatings. Compensation plates (denoted as CP in Figure 1.4) have been added to the input test masses to actively correct for thermal lensing [32]. Advanced sensors and actuators will be used to apply actuation to the test masses [33] (this topic is covered more thoroughly in Chapter 6). The test masses will be suspended on fused silica fibres, replacing the original steel wires, on pendulum suspension systems with either 3-stages (for the recycling mirrors and MC mirrors) or 4-stages (for the ETMs, ITMs, BS and folding mirrors) [34].

## A global network of detectors

To date, there has been no detection of gravitational waves while the first generation detectors were in operation, and therefore every effort has been made to maximise the probability of detecting such waves. Gravitational waves which reach the Earth from space could be travelling from any direction for any duration of time. It is therefore beneficial to have detectors positioned around the globe to increase the chances of at least one of the instruments catching the signal; the data can then be verified with the other detectors. It is with this intention that detectors H1 and L1 (with the exact same construction) are set in their chosen locations: the arms of both detectors are aligned (L1 is rotated by  $90^\circ$  with respect to H1) to increase sensitivity for the same GW polarisation [35], and there is sufficient distance between H1 and L1 that any noise disturbances which accidentally trigger a detection in one detector will not register in the other.

As well as increasing the likelihood of detecting gravitational waves, the global network of detectors is also important for future gravitational wave astronomy since more information about the gravitational wave signal can be acquired by triangulation, such as the sky location and specific parameters of the source [24].

## 1.3. Noise sources and sensitivity

Figure 1.5 illustrates predicted noise levels for the major noise sources for the Advanced LIGO detector. It was created using the Gravitational Wave Interferometer Noise Calculator (GWINC) [36]. Below 10 Hz, seismic noise acts as the primary limit, while gravity gradient (Newtonian) noise is expected to be a limiting factor at about 10 Hz. In the low-frequency regime between 10 Hz and 40 Hz, a combina-

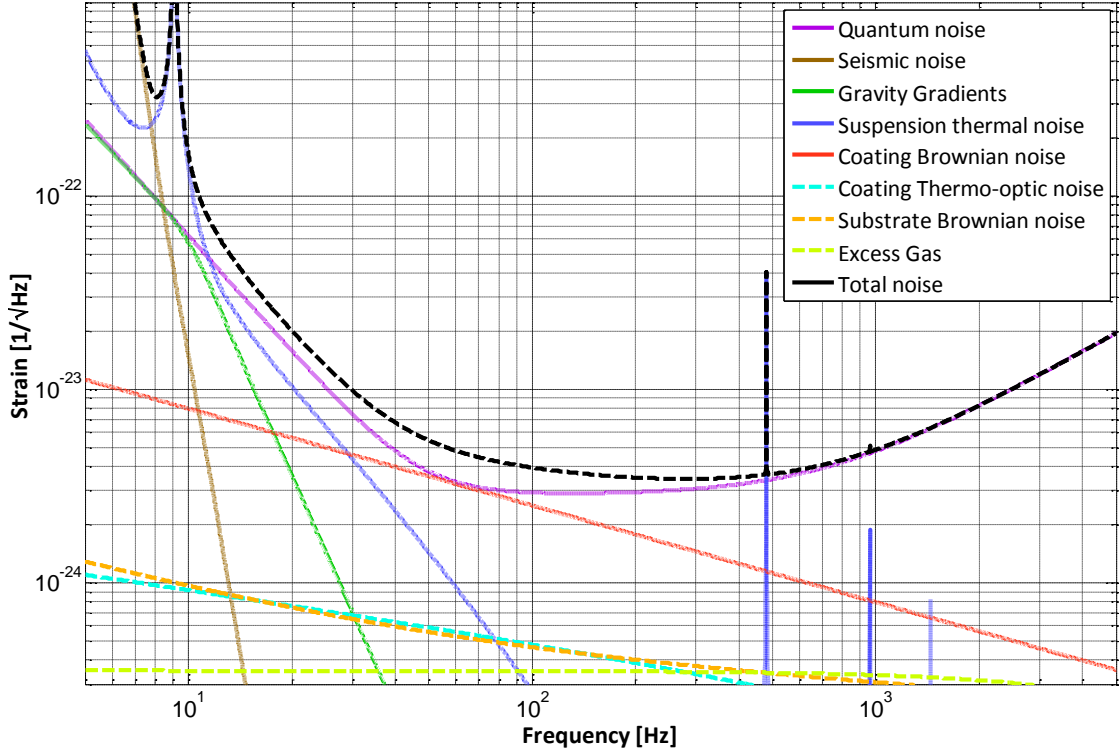


Figure 1.5.: Predicted noise curve for Advanced LIGO using GWINC resulting from various noise sources for an input laser power of 125 W.

tion of suspension thermal noise and radiation pressure noise will restrict sensitivity levels. Mirror thermal noise and quantum noise (both radiation pressure and shot noise) will dominate in the intermediate range from 40 Hz to around 200 Hz. Finally, shot noise will be the restraining noise source above 200 Hz [27]. The black trace represents the total noise in the detector, setting the overall sensitivity limit of the detector from all noise contributions across the frequency band. We now look at the main noise sources in more detail.

### 1.3.1. Seismic and Newtonian noise

Noise sources with seismic origin can induce motions of the test masses causing changes in the length of the arm cavities, and quite possibly masking potential gravitational wave signals. Seismic noise can affect the test masses either directly or via Newtonian effects.

#### Seismic noise

Seismic noise refers to ground vibrations due to human activity and environmental factors (such as oceanic, geophysical and atmospheric occurrences). Even if a detector was situated in a remote location, then due to the presence of ambient seismic noise, the test masses would typically be subject to motions in the order of  $10^{-9} \text{ m Hz}^{-1/2}$  at 10 Hz [8], which is still considerably larger than the signal of the gravitational wave strain.

Two forms of seismic noise exist: *bulk waves*, which propagate through the interior of the Earth with longitudinal and transverse motions, and the more disruptive *surface waves*, which travel along the surface of the Earth in the form of Rayleigh waves and Love waves [37].

While the effects of seismic noise are strong at low frequencies, the noise weakens at higher frequencies. Therefore seismic isolation techniques concentrate on reducing large disturbances at lower frequencies while being sensitive enough at higher frequencies, allowing test masses to respond to gravitational waves.

Advanced LIGO aims to reduce the seismic cut-off frequency from 40 Hz (Initial LIGO) to 10 Hz (shown as the brown trace in Figure 1.5). The complex seismic isolation and suspension systems will ensure that motions imparted on the test masses

from seismic noise are lowered to amplitudes of the order of  $10^{-19} \text{ m Hz}^{-1/2}$  [28].

Seismic isolation is achieved through two integrated mechanisms: the *seismic isolation subsystem* (SEI) and the *suspension subsystem* (SUS) [38]. The SEI is designed to attenuate seismic noise due to ground motion in both vertical and horizontal directions. It is formed of seismic isolation platforms resting on spring stacks, which offers sensing and control in 6 degrees of freedom. The SUS suppresses mainly horizontal motion (and some vertical motion) by suspending the test mass on a pendulum, on account that for a simple pendulum, any vibrations above its resonant frequency are attenuated. The pendulum is suspended within the seismic isolation platform, and further improvement is made by introducing multiple stages to the pendulum structure, thereby filtering out a range of frequencies.

Sensing and controlling the length of the detector arm cavities is crucial and relies on precise mirror positioning through the use of sensors and actuators, known as *BOSEMs* (Birmingham Optical Sensor and Electro-Magnetic actuators) [33]. The subject of suspension systems will be revisited in Chapter 6, where the development of BOSEMs in particular will be discussed in further detail.

### **Newtonian noise**

Also referred to as gravity gradients, Newtonian noise is generated through environmental mass density fluctuations, and is an indirect effect of seismic noise (although acoustic and atmospheric activities also contribute) [37]. For example, if a nearby object is exposed to seismic noise, its gravitational field will fluctuate and induce motion in the test masses. For current gravitational wave detectors at ground level, surface waves with seismic origin are expected to be the most harmful in comparison to other Newtonian noise sources [39].



In Figure 1.5, the contribution from Newtonian noise (depicted by the green trace as ‘gravity gradients’) lies below the total noise, suggesting that second generation detectors will most likely be unaffected by Newtonian noise, but more sensitive third generation detectors such as the Einstein Telescope (ET) will be susceptible [39].

Newtonian noise cannot be isolated but it can be reduced by positioning the gravitational wave detector in a quiet location. A better option would be to build the detector underground, with the advantage of greatly reducing surface waves. Another method of reducing Newtonian noise is through the use of *noise subtraction*, which involves placing seismometers around the test masses, monitoring the relative ground motion and applying a subtraction signal to the feedback control signal [14, 40].

### 1.3.2. Quantum noise

Interferometry precision is fundamentally limited by quantum noise (purple trace in Figure 1.5). Consider a laser beam incident on a test mass: if the relative change in the mirror positions are observed to a high degree of accuracy, then according to the Heisenberg uncertainty principle, the momenta of the test masses will be disturbed, leading to uncertainties in the phase difference between the two arm cavities [41]. These perturbations could potentially conceal gravitational wave signals. The effect of quantum noise is attributed by *radiation pressure* and *shot noise*.

#### Radiation pressure

Radiation pressure occurs when the surface of the mirror test masses are exposed to a fluctuating number of photons, resulting in random perturbations of the test

mass position. The strain due to detector radiation pressure,  $h_{rp}$ , for frequency  $f$  is described by [8]:

$$h_{rp}(f) = \frac{1}{mf^2L} \sqrt{\frac{\hbar P_{in}}{2\pi^3 c \lambda}}, \quad (1.2)$$

where  $m$  is the mass of the mirror,  $L$  is the length of the cavity arm,  $\lambda$  is the wavelength of the laser beam and  $P_{in}$  is the input power.

Although radiation pressure rises with increased  $P_{in}$ , it falls in proportion to  $1/f^2$ . Radiation pressure also decreases with increased mirror masses, as heavier objects are less inclined to move from photon collisions.<sup>4</sup>

### Shot noise

Shot noise arises from the discreteness of photons and the statistical uncertainty in the number that will be detected at the output photodetector. If the mean number of photons in a given time interval is  $N$ , then the uncertainty in the number of photons is given by  $\sqrt{N}$ .

The strain due to detector shot noise,  $h_{shot}$ , for a given frequency can be expressed as [8]:

$$h_{shot}(f) = \frac{1}{L} \sqrt{\frac{\hbar c \lambda}{2\pi P_{in}}}. \quad (1.3)$$

Since power is directly proportional to  $N$ , it stands to reason that increasing  $P_{in}$  will a) proportionally increase the measured gravitational wave signals, and b) decrease

---

<sup>4</sup>There has to be a compromise between a test mass heavy enough to reduce radiation pressure yet not too heavy for the suspension systems supporting it.

the shot noise proportionally to  $\sqrt{P_{in}}$ . In other words, although the absolute shot noise increases, the relative shot noise decreases, and so the signal-to-shot noise ratio improves. Increased power, however, comes at the cost of increased radiation pressure noise.

### 1.3.3. Thermal noise and limitations

A fundamental limit to detector sensitivity is thermal noise, and is important because it is limiting in the most sensitive detection band, in the region of about 10 - 200 Hz for Advanced LIGO, as seen in Figure 1.5. Thermodynamical fluctuations of molecules occur in suspensions and test masses, causing thermally induced motions of the suspended test mass in the form of rotation, translation and vibration. These motions affect the length of the detector arms and can ultimately mask potential gravitational wave signals.

Detector thermal noise can be categorised into two types: *suspension* thermal noise and *mirror* thermal noise. Suspension thermal noise is due to dissipation in the suspension wires which support the test mass - the wires are susceptible to Brownian noise and thermoelastic noise (dark blue trace in Figure 1.5). The test masses themselves are prone to mirror thermal noise, resulting from fluctuations in the mirror surface [42] and internal vibrations. Both the mirror coatings and substrates are affected by Brownian (red and orange dashed traces, respectively), thermoelastic and thermorefractive noise, the latter being applicable only to transmissive substrates.

Brownian noise refers to the absolute temperature of the optical element, whereas thermorefractive and thermoelastic noise relates to the fluctuation of temperature differences within the optical element. In some cases thermoelastic and thermorefractive noise can be combined and treated coherently as one noise source, referred

to as *thermo-optic* noise [43] (light blue dashed trace).

The most effective way of reducing overall thermal noise is by reducing the temperature of the test masses and suspensions via cryogenic cooling [44], and will be employed in future generation detectors such as the *Einstein Telescope* [45].

### Brownian noise in optics and suspensions

Brownian motion is a thermodynamic phenomenon that can also be interpreted as internal friction. It is a thermodynamic phenomenon referring to the drift of molecules due to random collisions, and as a result each degree of freedom obtains energy corresponding to  $\frac{1}{2}k_B T$ . The distance,  $x$ , a particle drifts<sup>5</sup> over a period of time,  $t$ , obeys

$$\langle x^2(t) \rangle = 2k_B T B t, \quad (1.4)$$

where  $k_B$  is the Boltzmann constant,  $T$  is the temperature of the optic and  $B$  describes the mobility of the particle (i.e. the response to a force applied externally). The kinetic energy of a given particle dissipates over time, and this leads to the Fluctuation-Dissipation theorem [46],

$$\langle S_F(f) \rangle^2 = 4k_B T \Re[Z(f)]. \quad (1.5)$$

The power spectral density of the fluctuating force (due to thermal excitations) is given by  $S_F(f)$  with  $f$  being the fluctuation frequency,  $Z(f)$  is the mechanical impedance of the optic, and  $\Re[Z(f)]$  represents the real part of the the mechanical

---

<sup>5</sup>In the case of solid materials, this refers to the movement of an atom due to vibration, since particles are not free to move around as they are in liquids and gases.

impedance, equivalent to the dissipative part [47, 48]. Equation (1.5) describes the relation between random thermal excitations of molecules and their velocity fluctuations.

Using the mechanical admittance,  $Y(f)$ , given by  $Y(f) = Z^{-1}(f)$ , we obtain the following expression for the thermal noise spectral density [49]:

$$S_x(f) = \frac{k_B T}{\pi^2 f^2} \Re[Y(f)]. \quad (1.6)$$

The term  $Z(f)$  (and therefore  $Y(f)$ ) contains the frequency-dependent mechanical loss angle,  $\phi(\omega)$ , which defines the ratio of the dissipated energy,  $E_d$ , with the stored energy,  $E_s$ , per oscillation as:

$$\phi(\omega) = \frac{1}{2\pi} \frac{E_d}{E_s}. \quad (1.7)$$

The mechanical quality factor  $Q$  describes the extent to which a material is damped, and at resonance it is given as the reciprocal of the mechanical loss angle:

$$Q = \frac{1}{\phi(\omega)} = 2\pi \frac{E_s}{E_d}. \quad (1.8)$$

Alternatively,  $Q$  can be thought of as the relation between resonance frequency,  $f_0$ , and the bandwidth (full width half maximum) of the resonance peak  $\Delta f$ :

$$Q = \frac{f_0}{\Delta f}. \quad (1.9)$$

In order to reduce Brownian noise, most of the energy dissipation must occur at frequencies concentrated around the resonant frequency of the material. This is

achieved by using materials with a high Q-factor (and hence narrow bandwidth) whose resonance peaks lie outside of the measurement band for gravitational wave detection.<sup>6</sup>

Brownian noise in the suspension wires induce a physical motion of the test masses, whereas Brownian noise in the test masses themselves cause displacement of the mirror surface. The largest contribution to overall mirror thermal noise is Brownian noise in the coating (shown by the red trace in Figure 1.5), and this is owed in general to the poor Q-factors of mirror coating materials [50].

In addition to using materials with optimal properties, other methods to reduce Brownian noise include the use of alternative beam shapes [51], Khalili cavities [52] and waveguide coatings [53].

### **Thermoelastic noise in optics and suspensions**

Thermoelastic noise is also known as thermoelastic damping because it refers to the energy lost due to heat flow within the material [54]. Thermal fluctuations within the test mass or suspension wires are transformed into internal vibrations, giving rise to contortions of the material. Different regions experience compression or expansion which heat up or cool down respectively according to the Le Châtelier principle [55], and a temperature gradient is created. In an attempt to dissipate some of the mechanical energy generated by the flexing material, a heat flow within the material is triggered. When the temperature gradient changes through each vibration cycle, so too does the direction of the heat flow, and this changing process of dissipation leads to a fluctuation of the system and hence either a non-uniform

---

<sup>6</sup>Note that violin modes in the suspension wires lie within the GW detection band, but a long pendulum length ensures that these modes lie in the high-frequency region for control purposes [27].

mirror surface or length variations in the suspension wire, which ultimately stems from the fluctuation-dissipation theorem.

The linear strain of a material is related to its temperature by its linear thermal expansion coefficient,  $\alpha$ :

$$\alpha = \frac{1}{L} \frac{dL}{dT}, \quad (1.10)$$

where  $L$  corresponds to the length of the material and  $T$  is the temperature.

### **Thermorefractive noise in optics**

All mirror coatings and substrates of transmissive optics, namely the beamsplitter and the arm cavity input mirrors, are subject to thermorefractive noise, which stems from the temperature-dependent nature of the refractive index of the material [56]. When an optic is exposed to a laser beam, thermodynamical fluctuations in temperature lead to variations in the optical thickness (of the coating layers or substrate) causing the refractive index to change, and the reflected or transmitted laser beam subsequently suffers from phase-related fluctuations.

The change in the refractive index,  $n$ , relative to temperature variations is described by the thermorefractive coefficient,  $\beta$ :

$$\beta = \frac{dn}{dT}. \quad (1.11)$$

In order to reduce thermoelastic and thermorefractive effects, lower possible coefficients of  $\alpha$  and  $\beta$  are required. It is interesting to note that both of these noise sources are highly correlated since they originate from the same temperature fluc-

tuations, therefore raising the possibility that thermoelastic and thermorefractive mechanisms could cancel each other out to a certain extent [57, 58].

Transmissive optics with increased optical thickness are more sensitive to thermorefractive noise. In addition to thermal noise, however, transmissive optics are also highly prone to thermal effects from power absorption, which will be discussed further in the next section.

## 1.4. Thermal effects due to power absorption

As mentioned in Section 1.3.2, the relative shot noise is reduced by increasing the laser power and the circulating light power in the detector arm cavities. The laser power in the Advanced LIGO detector is set to increase from 10 W (Initial LIGO) to approximately 200 W. The power recycling cavity will further increase this power to about 2 kW, while the circulating power within the Fabry-Perot cavities is expected to reach around 800 kW [32].

The requirement for high laser power means that transmissive optical elements, such as the beamsplitter and the arm cavity input mirrors, are subject to greater power absorption. As with thermorefractive noise, absorption also occurs in all mirror coatings and transmissive substrates, leading to a non-statistical thermal deformation of the optics, an effect known as *thermal lensing*.

It is important to note the distinction between thermal noise and thermal lensing: the thermal noise effects described in Section 1.3.3 are due to statistical fluctuations, whereas thermal effects due to absorption are an ordered and systematic effect. Thermal lensing is not a noise source but an effect which distorts the wavefront of the laser beam causing modal mismatch and a reduced interference contrast.



### 1.4.1. Thermal lensing

Thermal lensing occurs in a combination of two ways. The first is a geometric distortion, whereby the Gaussian profile of a laser beam induces local heating concentrated around the centre of the optic. The coating and transparent substrate undergo thermal expansion, also with a greater effect at the centre, thus creating an additional lens at the optic, as indicated by the central ‘bulge’ in the optic in the lower half of Figure 1.6. The resulting change in the optical path length,  $\delta s_L$ , can be described as [59]:

$$\delta s_L \approx \frac{\alpha}{4\pi\kappa} P_a, \quad (1.12)$$

where  $\kappa$  is the thermal conductivity of the material and the total absorbed power is  $P_a$ .

The second distortion process takes place as a result of the Gaussian temperature distribution; the temperature gradients are coupled with corresponding gradients in refractive index (within the coating material and substrate) according to Equation (1.11). The change in refractive index instigates a change in the optical path length,  $\delta s_n$ , according to the relation [60]:

$$\delta s_n \approx \frac{\beta}{4\pi\kappa} P_a. \quad (1.13)$$

The effects of wave-front distortion due to the changing refractive index is signified in the lower half of Figure 1.6 by the altered beam parameters exiting the optic in comparison to the low power case shown in the upper half of Figure 1.6. It is worth noting that the ramifications of a varying refractive index are far more severe than those from geometric distortions. Using fused silica as an example, the ratio  $\alpha/\kappa$

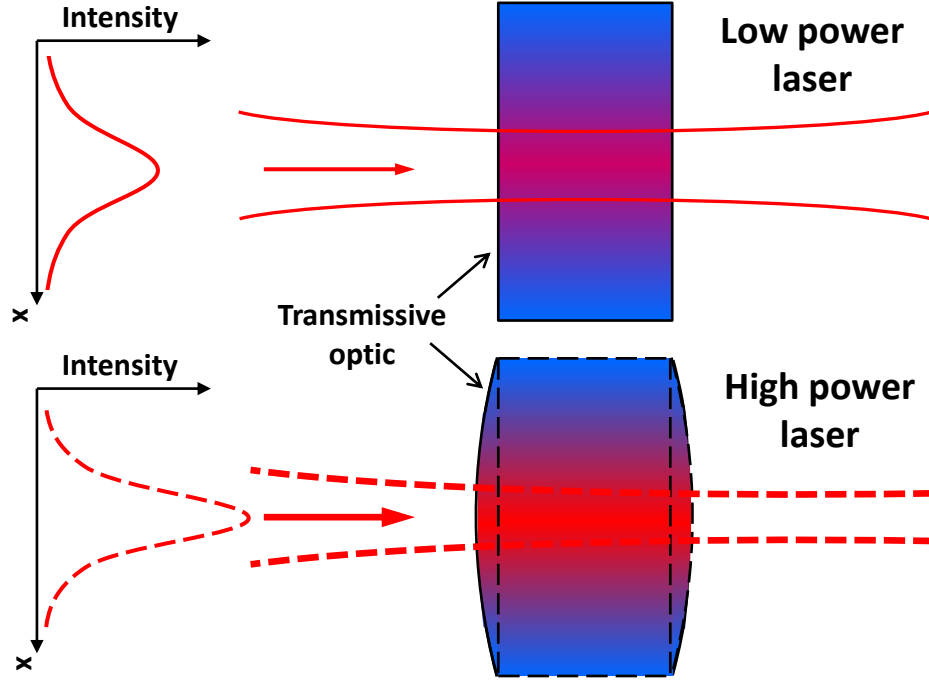


Figure 1.6.: Effects of increased power absorption in transmissive optics. The top half of the diagram shows a relatively low power laser beam penetrating the optic. In the lower half of the diagram, a higher laser power induces thermal lensing: firstly, thermal expansion of the optic material occurs in the form of a slight ‘bulge’, similar to an additional lens; secondly, the refractive index of the material is altered. As a result, the wave-front is distorted and changes the beam parameters of the exiting beam.

for thermal expansion is in the order of  $10^{-8} \text{ mW}^{-1}$ , whereas the ratio  $\beta/\kappa$  for the refractive index is higher at  $10^{-5} \text{ mW}^{-1}$  [59], and so the change in optical path due to a changing refractive index is greater.

Thermal lensing distorts the curvature of the wave-front of the reflecting or transmitting beam (the latter applies to transmissive optics), ultimately altering the beam parameters and the focal length (see Figure 1.6). Considering the long length of the cavity arms, the implications for wave-front distortion are crucial: modematching in the cavities will degrade, interference contrast of the laser beams deteriorate (lowering the recycling gain), cavity conditions may become unstable, and more light

may leak out of the dark port. Increased power absorption may also contribute to double refraction, or *birefringence*, in transmissive optics. The result is a decrease in the contrast of the output interference fringes [61]. The effects of aberrated optical elements due to power absorption will mainly be detrimental to the performance of second-generation interferometers: the lower laser power in initial LIGO meant that thermal lensing effects were not too problematic, however the strain sensitivity levels aimed by Advanced LIGO (in the order of  $10^{-24} \text{ Hz}^{-1/2}$ ) using higher laser power will be difficult to reach due to greater power absorption [60, 62].

One method to compensate for thermal lensing is through *active wave-front correction* (or thermally adaptive optics), and involves the application of an external heat source, for example by placing heated compensation plates inside the Fabry-Perot cavity arms in an attempt to cancel out the wave-front distortion [32, 63]. These techniques will be implemented in second-generation gravitational wave detectors, however they will only work to a certain extent and will not completely remove the effects of thermal lensing. Although high quality fused-silica substrates have been shown to have bulk absorption as low as  $25 \pm 0.1 \text{ ppm cm}^{-1}$ , thermal lensing effects still remain [64, 65]. Power absorption in transmissive optics will therefore continue to be a critical problem for future detectors operating with increased laser power.

## 1.5. Diffractive elements in interferometry

By replacing partially transmissive mirrors and beamsplitters with reflective diffraction gratings, the problem of thermal lensing and distortions due to power absorption can be reduced. Moreover, reflection gratings eliminate the need for optically transparent substrate materials, allowing for opaque (or less transmissive) materials with more favourable mechanical and thermal properties [66, 67]. One such example is

silicon, which exhibits increased thermal conductivity and a higher mechanical Q-factor than the currently used fused silica. However, at 1064 nm it has a higher optical absorption coefficient in comparison to fused silica, and so although silicon substrates cannot be used for conventional transmissive optics<sup>7</sup>, it would be suitable for reflective optics [68, 69]. In light of these advantages, the notion of interferometers based on all-reflective topologies are promising alternatives.

### 1.5.1. Diffraction gratings

A diffraction grating is an optical element consisting of a one-dimensional periodic structure of grooves, allowing light to be diffracted either through reflection or transmission. From now on we will consider only reflective devices, which can for instance be realised by etching a grating structure into the top-most layer of a dielectric high reflection (HR) coating<sup>8</sup> [70]. A standard *phase* diffraction grating is illustrated in Figure 1.7 - for a grating period of  $d$ , an incident beam with wavelength  $\lambda$  is diffracted into  $m$  diffraction orders. According to the grating equation

$$\sin \alpha + \sin \beta_m = \frac{m\lambda}{d}, \quad (1.14)$$

the diffraction angle  $\beta_m$  of a certain functional output coupling port will be different from the incident angle  $\alpha$ , with an exception for  $m = 0$ . This zero-order specular beam is simply the reflected beam as if the grating were a mirror and obeys  $\beta_0 = -\alpha$ . Note that the angle convention is such that  $\alpha$  and  $\beta$  are measured as positive when to the left of the normal, and negative when to the right of the normal.

---

<sup>7</sup>Note that silicon is considered to be an ideal material in transmission at 1550 nm, due to greatly reduced optical absorption.

<sup>8</sup>Etched gratings with an application of a smooth coating on top have also been proposed but were found to scatter more light power than those gratings with grooves etched directly into the top layer [67].

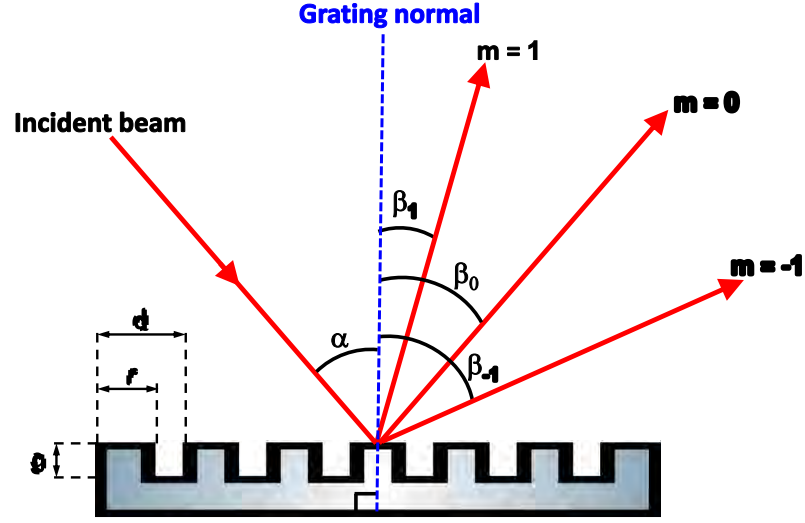


Figure 1.7.: Diffraction of light by a reflective diffraction grating. Light incident at an angle  $\alpha$  diffracts into  $m$  diffraction orders at angles of  $\beta_m$ , all angles being with respect to the grating normal. The groove profile is characterised by the groove spacing  $d$ , ridge width  $r$  and groove depth  $g$ .

Diffraction gratings can be adapted for various applications by adapting the parameters in the grating equation in Equation (1.14) for specific requirements, such as  $d$ , number of ports and diffraction angles, an example being the different grating configurations seen in Section 1.5.2.

The groove profile is described using certain parameters which are not given by the grating equation. These include the groove depth  $g$ , ridge width  $r$  and fill factor  $f = r/d$  (as seen in Figure 1.7), a combination of which determines the actual efficiency of the diffraction into each exiting port of the grating. These parameters can be designed to create a specific desired grating functionality [71].

### 1.5.2. All-reflective interferometer configurations

Diffraction gratings were first proposed as replacements for transmissive optics such as the beamsplitters and input mirrors in interferometric gravitational wave detectors by Drever [72]. These all-reflective interferometers were experimentally demonstrated by Sun and Byer [66] using configurations based on the Michelson, Sagnac and Fabry-Perot interferometers. The latter was a concept for a cavity coupler using high-efficiency diffraction gratings in the 1st order Littrow configuration, seen in Figure 1.8(a). However, in this configuration the light inside the cavity is diffracted, and so a grating with a high diffraction efficiency is necessary. This requires the grating profile to be fabricated with a high degree of accuracy and restricted tolerances, which in practice is extremely difficult to achieve perfectly.

Drever proposed that overall losses for a cavity coupler would be lower if low-efficiency diffraction gratings were employed in the 2nd order Littrow configuration, shown in Figure 1.8(b). Here, the light within the cavity is mostly reflected while the overall amount of light being diffracted is low. This allows for gratings with low diffraction efficiencies whose profiles have larger tolerances, and hence are easier to manufacture.

The replacement of the beamsplitter with a diffraction grating in a Michelson interferometer was demonstrated experimentally [73, 74]. Provided that a non-Littrow configuration was used, the diffraction grating acts as a beamsplitter by generating 4 ports, as shown in Figure 1.9. The concept becomes clear by treating the diffraction stages separately. Figure 1.9(a) shows diffraction of the initial input beam diffracted into mirrors 1 and 2, representing the interferometer arms. Since the classical Michelson design consists of perpendicular arms, an angle of  $90^\circ$  between mirrors 1 and 2 is ideal [75]. In Figure 1.9(b), the reflected beam from the first mirror is diffracted towards the source of the initial beam and the output, and in

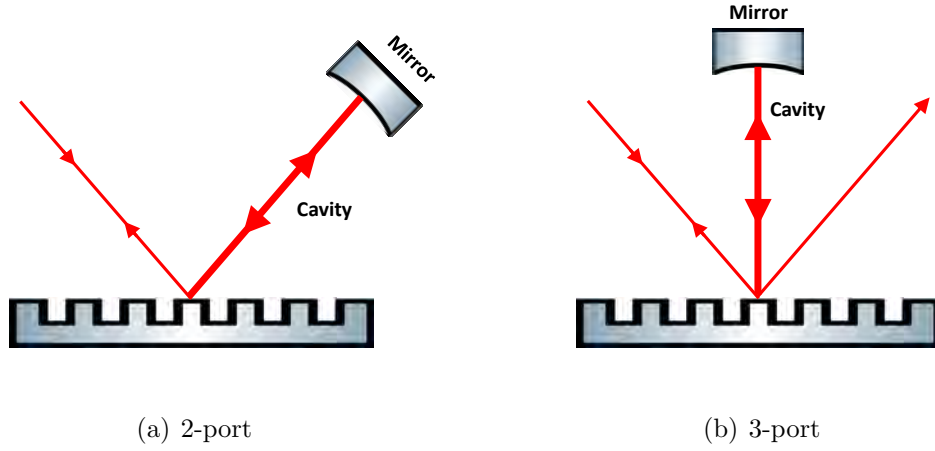


Figure 1.8.: Cavity couplers using diffraction gratings as alternatives to linear Fabry-Perot cavities. Cavities with (a) 2 ports, and (b) 3 ports are achieved using 1st and 2nd order Littrow configurations respectively.

Figure 1.9(c) the reflected beam from the second mirror is also diffracted towards the source and the output.

All-reflective interferometers benefit largely from the reduction of thermal issues, thus helping to increase sensitivity in future gravitational wave detectors. However, the implementation of diffraction gratings requires an in-depth understanding of the phase relations, which we discuss in the next section.

### 1.5.3. Grating-related phase effects in plane waves

The reduced symmetry in diffraction gratings means that the phase of light will be affected differently in the event of any grating movement or beam movement on the grating, compared to mirrors and beamsplitters. Mirrors are unaffected by roll movement due to their cylindrical symmetry, but grating rotation around the grating normal introduces an extra degree of freedom. More importantly though, a translation of the grating parallel to its surface and perpendicular to the direction

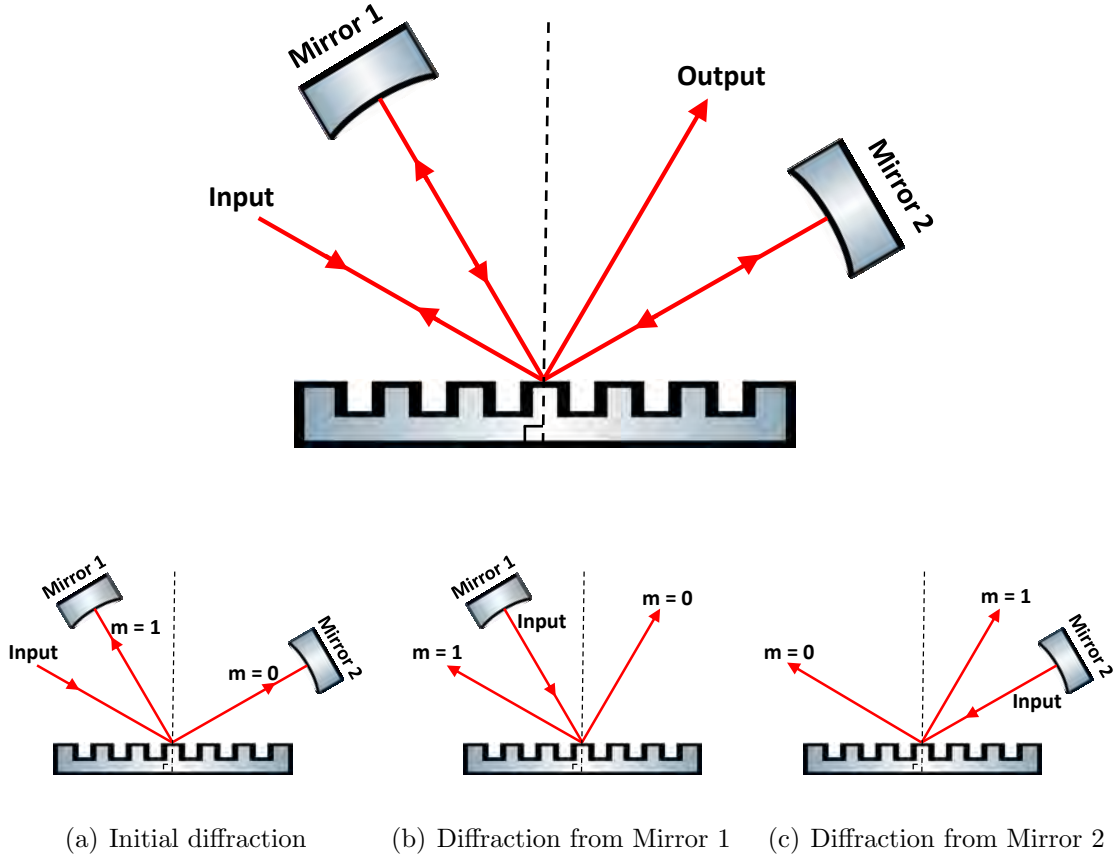


Figure 1.9.: *Top*: An all-reflective interferometer is created using a diffraction grating in a non-Littrow configuration, resulting in 4 ports. *Bottom*: The beam path is considered in three separate stages: (a) initial input beam diffracted towards both mirrors, (b) reflection from mirror 1 diffracted towards the source and the output, (c) reflection from mirror 2 diffracted towards the source and the output.

of the grooves causes a phase shift in the reflected light [76]. We will consider the phase noise effects due to grating translation.

### Change in optical path length

The broken symmetry of light deflection in diffraction gratings leads to strong coupling between alignment noise and output phase noise [77], and this effect is illus-



trated in Figure 1.10. From a simple geometrical consideration, a slight displacement of either the grating,  $\Delta x'$ , or the beam,  $h$ , relative to each other causes an optical path length shift of  $\Delta P = \delta_1 + \delta_2$  (where  $\delta_2$  is negative). Note that displacements are for distances less than the grating period.

For the moment, the blue and red rays can be considered as part of the same plane wave, and so at every reference plane (normal to their propagation direction) both rays should have the same phase. Yet, Figure 1.10 shows that there is a difference in the total optical path length of  $\Delta P$  (and therefore a difference in the phase). This implies that the diffraction at the grating advances or retards the phase of those rays which have a spatial distance of  $\Delta x'$  away from some chosen reference ray, ensuring that the phase over the total path length remains the same (as the reference ray). As far as the grating is concerned, the only displacement that occurs is by  $\Delta x'$ , as projected on the grating surface. Therefore a translation  $h$  of the incident beam can be considered as being equivalent to a grating displacement of  $\Delta x'$ . A further discussion of this geometrical consideration can be found in [77].

From Figure 1.10 we can deduce the following identities for the change in length:

$$\delta_1 = \Delta x' \sin \alpha \quad \text{and} \quad \delta_2 = \Delta x' \sin \beta, \quad (1.15)$$

which can be rewritten in terms of the total shift in length as

$$\delta_1 + \delta_2 = \Delta x' (\sin \alpha + \sin \beta). \quad (1.16)$$

This shift is shown to be related to the displacement  $\Delta x'$  via the grating equation

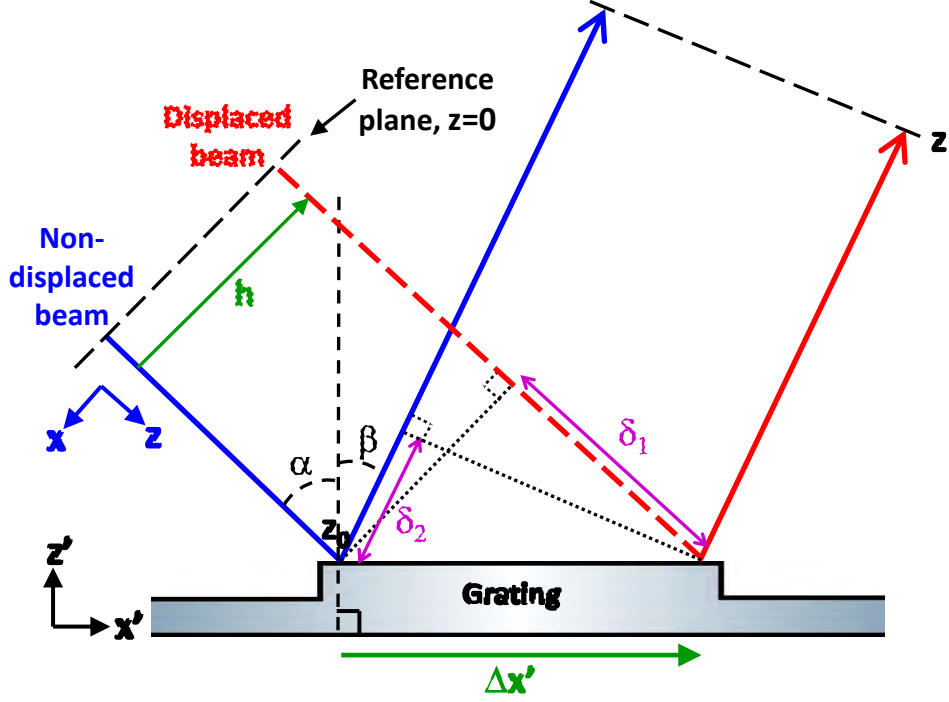


Figure 1.10.: Diffraction of light into the  $m$ -th diffraction order when the grating is displaced by amount  $\Delta x'$  relative to the beam. A grating displacement  $\Delta x'$  (corresponding to a parallel beam shift  $h$ ) leads to an output optical path length change of  $\Delta P$  according to Equation 1.17. For clarity only one diffraction order  $m$  is considered.

by substituting Equation (1.14) into Equation (1.16) to give

$$\Delta P = \delta_1 + \delta_2 = -\Delta x' \frac{m\lambda}{d}. \quad (1.17)$$

The negative sign arises from the fact that translating the grating to the left (or the beam to the right) induces a positive phase change via the extra geometric path length,  $\delta_1 + \delta_2$ . A ‘negative’ phase change is therefore required to counteract the positive phase change, thereby ensuring that the phase of both non-displaced and displaced beams in Figure 1.10 are the same at the end reference plane,  $z$ .

Keeping in mind that the change in phase,  $\Delta\theta$ , is described as

$$\begin{aligned}\Delta\theta &= k \Delta z \\ \Delta\theta &= k(\delta_1 + \delta_2) \\ \delta_1 + \delta_2 &= \frac{\Delta\theta}{k},\end{aligned}\tag{1.18}$$

then by substituting into Equation (1.17) we find

$$\begin{aligned}\frac{\Delta\theta}{k} &= -\Delta x' \frac{m\lambda}{d} \\ \Delta\theta &= -\Delta x' \frac{km\lambda}{d}.\end{aligned}\tag{1.19}$$

Using the relation  $k = (2\pi)/\lambda$ , we obtain the following expression to describe phase noise (change in phase due to grating displacement):

$$\boxed{\Delta\theta = -\Delta x' \frac{2\pi m}{d}}.\tag{1.20}$$

We refer to Equation (1.20) more specifically as the intrinsic phase factor. Note that beam displacement,  $h$ , is proportionally equivalent to a grating translation as:

$$h = -\Delta x' \cos \alpha.\tag{1.21}$$

Equation (1.20) implies a substantial phase change of up to  $2\pi$  between a non-displaced and displaced beam for displacements in the order of the grating period (i.e  $\Delta x' = d$ ). This effect is observed in Figure 1.11, which shows a plot of Equation (1.20) against varying grating displacements,  $\Delta x'$  (for diffraction order  $m = 1$ ). The resulting change in phase,  $\Delta\theta$ , varies over  $2\pi$  radians (between  $\pm\pi$ ) for displace-

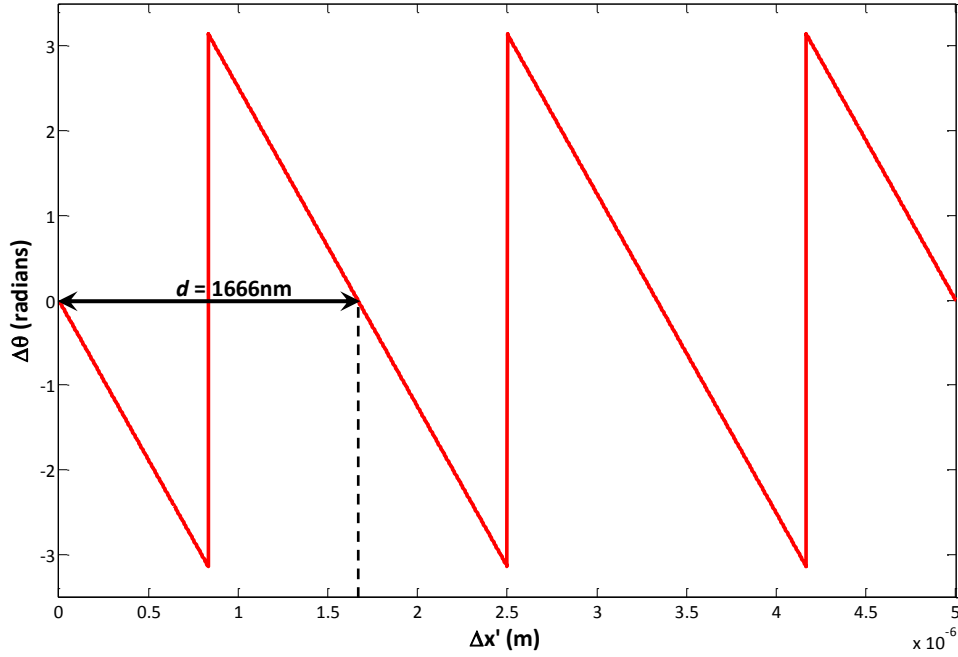


Figure 1.11.: Varying grating displacement,  $\Delta x'$ , causes the resulting change in phase,  $\Delta\theta$ , to vary over  $2\pi$  radians (assuming  $d=1666.7$  nm and  $m = 1$ ).

ments less than  $d$ , and the length of each phase cycle coincides with the grating spacing,  $d = 1666.7$  nm, as expected from Equation (1.20). With a total grating displacement of  $5\mu\text{m}$  along the  $x$ -axis in Figure 1.11, three complete phase cycles are clearly visible.

It should be noted that in addition to lateral displacement, longitudinal displacement of the grating (or mirror) also causes phase noise of a similar order [77]. However, longitudinal motion can be controlled to a high degree of accuracy through the use of sophisticated locking techniques involving various feedback control loops [78]. Unfortunately, the reduced symmetry in a diffraction grating compared to a mirror means that lateral motion is much more complicated to control [79], thereby limiting all-reflective geometries.

### 1.5.4. First attempts to mitigate phase noise

It was realised that grating coupled cavities introduce a new noise source simply due to increased sensitivity to general beam alignment. The possibility of reducing the phase noise from lateral grating displacements in grating coupled cavities was investigated by Hallam [80, 81], whereby grating coupled cavities with 2-port and 3-port configurations were compared to traditional two-mirror cavities.

Figure 1.12(a) shows the various light fields within a 2-port coupled grating cavity in a 1st order Littrow configuration. The incident beam,  $b_0$ , is diffracted by the grating ( $a_1$ ). This light propagates a distance  $L$  ( $a'_1$ ) before reaching the mirror (ETM), where it is either reflected ( $a_2$ ) or transmitted ( $a_4$ ). The reflected part travels the distance  $L$  back towards the grating ( $a'_2$ ) where it eventually undergoes diffraction again ( $a_3$ ) and exits along the same path as the incident beam. The signal readout occurs at port  $a_4$  using the transmitted portion of the beam.

Figure 1.12(b) illustrates the path of the light fields in a 3-port coupled grating in a 2nd order Littrow configuration. The incident beam,  $i_0$ , is diffracted ( $a_1$ ) and propagated a distance  $L$  ( $a'_1$ ), as in the 2-port case. The transmitted light is denoted  $a_5$ , and the reflected part ( $a_2$ ) propagates back to the grating ( $a'_2$ ). This beam is eventually diffracted in one of two ways: it can either exit the cavity as the output beam  $a_3$ , or travel back along the same path as the incident beam as  $a_4$ . The transmitted light forms the signal readout at port  $a_5$ .

Hallam proposed using the  $a_3$  port for signal readout in the 3-port cavity instead of the  $a_5$  port, and subsequently performed noise measurements for signal readout at the following three ports:  $a_4$  (in a 2-port cavity),  $a_3$  and  $a_5$  (in a 3-port cavity). The measurements were recorded as suspension requirements in Figure 1.13, where smaller requirements correspond to increased phase noise contained in the signal

readout.

Hallam demonstrated that, when compared to a two-mirror cavity, the isolation requirements against end-mirror tilt for a 2-port cavity were 8 orders of magnitude worse, yet for a 3-port cavity the requirements were only 5 orders of magnitude worse. The suppression of lateral displacement phase noise by the cavity finesse allowed the 3-port cavity to perform better than the 2-port cavity. The reduced performance of the 2-port cavity is also indicated by the tighter restrictions of the  $a_4$  port signal readout (blue trace in Figure 1.13).

The suspension requirements are less constrained at higher frequencies above 110 Hz for signal readout at the  $a_5$  port (green trace in Figure 1.13). However the requirements in the low frequency regime (10 Hz - 110 Hz) were found to be more relaxed for signal readout at the  $a_3$  port (red trace), and this was due to a partial cancellation of phase noise in the forward-reflected output port,  $a_3$ , and a summation in the back-reflected port,  $a_4$ , of the 3-port cavity.

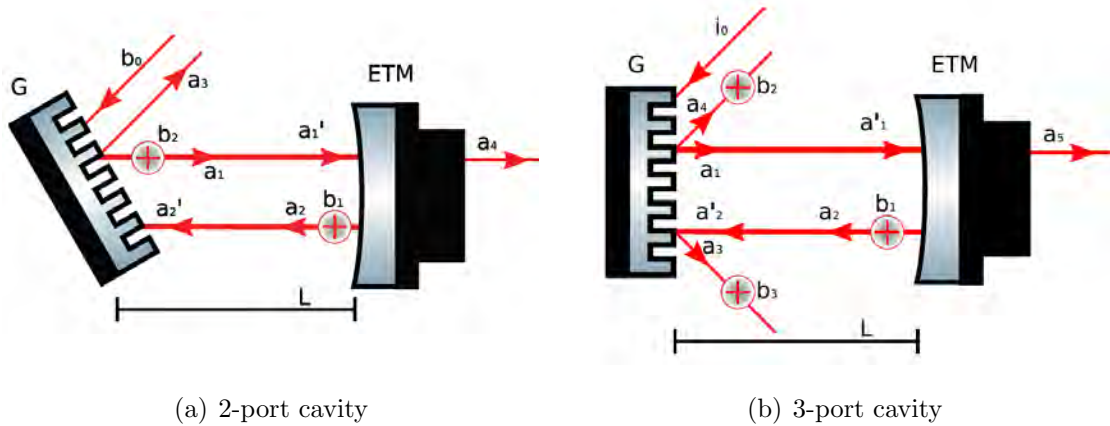


Figure 1.12.: Schematic for grating cavities depicting the various light fields within the cavity, where  $\oplus$  indicates sideband signals. (a) The signal readout in the 2-port cavity is located at the  $a_4$  port. (b) In the 3-port cavity, the signal readout is situated at the  $a_3$  port instead of the  $a_5$  port, thus improving suppression of lateral displacement phase noise. [80]

Partial cancellation was observed by oscillating the grating laterally in the 3-port cavity, causing the carrier light to produce ‘input’ sidebands with an amplitude proportional to the external input field. The input sidebands were slightly detuned from the cavity and so resonated with only some gain. Meanwhile, the carrier field amplitude was enhanced by the cavity gain and coupled out, generating output sidebands which were proportional to the carrier amplitude. The diffraction order for the input beam was  $m = +1$  and the output beam was  $m = -1$ , so the input and output sidebands had opposite signs and thereby cancelled each other out. However,

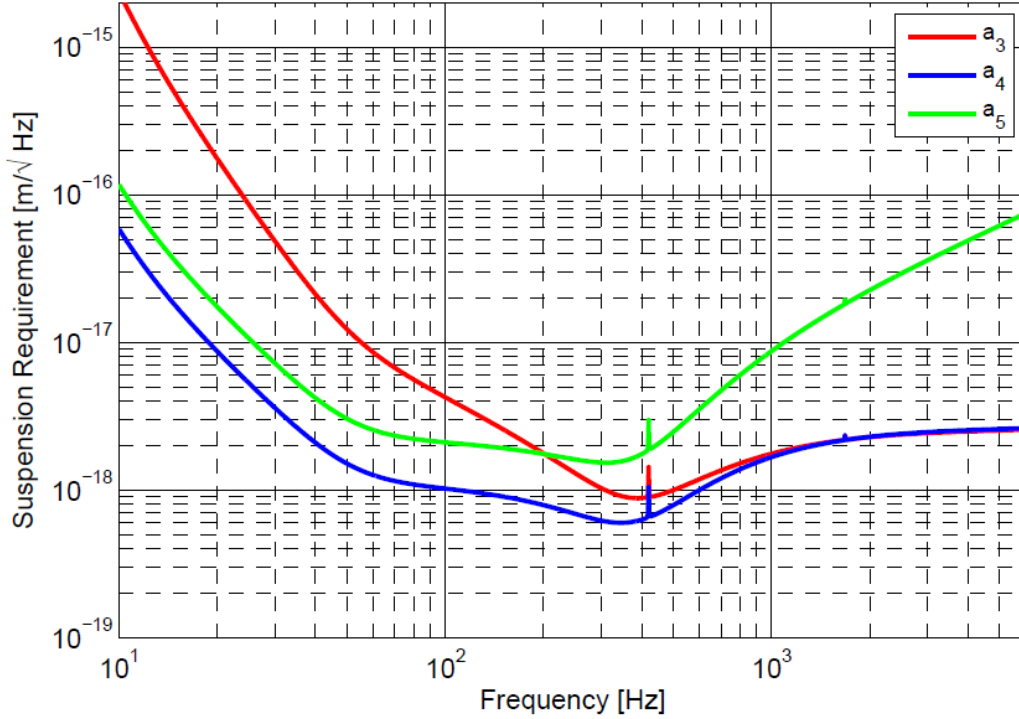


Figure 1.13.: Suspension requirement for the maximum tolerable lateral grating displacement necessary for achieving required sensitivity levels in the Advanced Virgo design [81]. Measurements were taken at three different ports:  $a_4$  (for a 2-port cavity),  $a_3$  and  $a_5$  (both in a 3-port cavity) (see Figure (1.12)), revealing that suspension requirements were alleviated by a factor of 20 at 10 Hz when port  $a_3$  was used for signal readout in comparison to port  $a_5$ .

since the gain of the input sidebands was less than that of the output sidebands, the cancellation was only partial.

As a result of using the  $a_3$  port for signal readout, the suspension requirements were alleviated (and thereby phase noise suppressed) by a factor of 20 at 10 Hz. A correlation was also observed between lower finesse cavities (i.e wider bandwidths) and increased phase noise suppression, and therefore the use of low finesse cavities was recommended.

### **1.5.5. An analytical framework for grating-related phase noise in simulations**

Partial cancellation of grating-related phase noise was demonstrated successfully in [80] with the use of improved optical setups and alternative signal readout ports. Although the results are encouraging and the prospect of using diffractive elements in future gravitational wave detectors looks promising, a lack of knowledge for practical implementations prevails, and therefore further investigation into diffractive elements is required.

Simulation tools potentially offer an accurate method of determining the impact of grating-related phase noise on detector sensitivity, and are a useful aid for experimental investigations. The basis of the most common simulation tools used for gravitational wave detection development are either *fast Fourier transforms* (FFT) or *modal*. FFT-based simulation tools have the capacity to simulate any beam shape and are therefore adept for detector development, for instance dealing with multiple modes and optical losses within cavities. Meanwhile, modal-based simulation tools rely on the technique of modal decomposition and are useful for the analysis of small beams possessing tiny defects; these tools are proficient for purposes such



as auto-alignment and error signals, where specific optical properties are concerned. One such example of a modal-based simulation tool is FINESSE [82].

Simulations of beam misalignment and diffractive optics require changes in their coordinate systems, yet modal simulation tools are paraxial, i.e., they are restricted to one coordinate system. In order to replicate beam (or grating) displacements, modal simulation tools employ a technique known as modal decomposition, achieved by adding higher-order modes to the fundamental zero-order mode. They are based on Gaussian models, where Hermite-Gauss modes are used to describe the spatial aspects of the beam (e.g. beam shape and position). However, as shown in this work, these modal simulations do not include the intrinsic phase factor from gratings, which plays an important role in the modelling of beam diffraction for all-reflective GW detectors.

There is an urgent need for a suitable analytical framework which incorporates the intrinsic phase factor into simulations using a realistic Gaussian model instead of geometric planewave considerations. This would then allow for a faster and more accurate computation of grating-related phase noise, and can be a useful tool to simulate grating effects for future layouts of high-precision interferometry.

## 1.6. Structure of this thesis

The aim of this thesis is to develop a Gaussian-based framework for grating diffraction and investigate grating-related phase effects due to beam misalignments for use in modal simulation tools, as well as determining the cause for the absence of the intrinsic phase factor from modal-based simulation tools. These elements are addressed under the following chapters.

In Chapter 2 we establish an analytical framework based on a Gaussian description and explore the effects of beam displacement through modal decomposition. We confirm that the Gaussian model does not contain the intrinsic phase factor to produce the same phase change as observed with geometric plane waves (Equation (1.20)). We next conduct a thorough analysis of the phase distribution of a Gaussian beam displaced by two different methods: a geometric translation of the beam and a modal decomposition. We then verify the accuracy of modal decomposition by comparing its phase distributions with those produced by actual beam translations, before and after grating diffraction.

The concept of modal decomposition to describe beam displacements is continued in Chapter 3 through experimental means. Using a Mach-Zehnder grating interferometer, we investigate the notion that a difference in phase change may occur between zero-order and first-order mode beams having undergone grating diffraction, and thereby determine whether the phase of a diffracted beam is dependent on the beam shape (or mode).

Chapter 4 introduces a rigorous time-domain simulation tool used to examine the diffraction of displaced Gaussian beams in further detail. Two scenarios are considered: a geometric beam (or grating) displacement and a modal decomposition. Ultimately, a direct comparison of the resulting phase profiles is made in order to determine the conditions required in order to obtain phase changes due to the intrinsic phase factor.

Chapter 5 reports on the conclusions drawn from the work presented in this thesis. The research and findings described here have also been published in [83] and [84].

Chapter 6 will branch off the main thesis topic where I cover the work that was carried out as part of the Suspensions Working Group for Advanced LIGO.

## Chapter 2.

# ANALYTICAL FRAMEWORK FOR DIFFRACTED GAUSSIAN BEAMS

A Gaussian model is required to address phase noise accurately, instead of a planewave approximation. In this chapter, we aim to develop a Gaussian-based framework for describing beam misalignments, before and after grating diffraction (through astigmatism). We determine whether beam displacement within the Gaussian framework displays any sign of the phase noise seen in an otherwise geometric planewave consideration (i.e. a change in phase over  $2\pi$  radians). Section 2.1 provides the fundamentals of Gaussian optics, with complete beam profile descriptions for zero-order and first-order modes. In Section 2.2, we apply the effects of beam displacement by means of a first-order modal decomposition, yielding new beam descriptions as part of the analytical modal model. Section 2.3 formulates the phase terms contained within the description of non-translated, geometrically translated and modally decomposed Gaussian beams, and presents a comparison of the electric fields. The concept of grating diffraction is then discussed in Section 2.4 in the form of astigmatism.

## 2.1. Gaussian optics

In this section, we present an overview of Gaussian optics, including the parameters which define the beam profiles for propagating Gaussian beams, both for zero-order and first-order modes, and the notation used.

### 2.1.1. Gaussian beam profile

Gaussian beams are described by Hermite-Gauss modes ( $\text{HG}_{nm}$ ), and are one of the solutions of the paraxial wave equation [85]. The electric field of a Gaussian beam propagating in the  $z$ -direction can be described in terms of Hermite-Gauss modes in the following general form:

$$E(x, y, z) = \sum_{nm} a_{nm} u_{nm}(x, y, z) e^{-ikz}, \quad (2.1)$$

where  $a_{nm}$  are complex amplitude factors, and the indices  $n$  and  $m$  represent the number of nodes along the  $x$ -axis and  $y$ -axis respectively, thereby determining the mode order of the beam. The function  $u_{nm}(x, y, z)$  describes the transverse spatial distribution of the beam as it varies slowly with  $z$  and can be expressed along the  $x$  and  $y$ -directions as

$$u_{nm}(x, y, z) = u_n(x, z) u_m(y, z),$$

A complete definition for  $u_{nm}(x, y, z)$  is as follows:

$$\begin{aligned} u_{nm}(x, y, z) &= (2^{n+m-1} n! m! \pi)^{\frac{1}{2}} \frac{1}{\omega(z)} \exp(i(n+m+1)\Psi(z)) H_n\left(\frac{\sqrt{2}x}{\omega(z)}\right) \\ &\times H_m\left(\frac{\sqrt{2}y}{\omega(z)}\right) \exp\left(-i\frac{k(x^2+y^2)}{2R_C(z)} - \frac{x^2+y^2}{\omega^2(z)}\right), \end{aligned} \quad (2.2)$$

where  $H_n$  and  $H_m$  are Hermite polynomials and  $k$  is the wave number, specified as  $k = 2\pi/\lambda$ .  $\omega(z)$  is the radius of the beam spot,  $R_C(z)$  is the radius of curvature of the beam wavefronts, and  $\Psi(z)$  is the Gouy phase, all of which have the following definitions:

$$\begin{aligned}\omega(z) &= \omega_0 \sqrt{1 + \left(\frac{z}{z_R}\right)^2}, & z_R &= \frac{\pi\omega_0^2}{\lambda}, \\ \Psi(z) &= \arctan\left(\frac{z - z_0}{z_R}\right), & R_C(z) &= z + \frac{z_R^2}{z},\end{aligned}$$

where  $\omega_0$  is the radius of the beam waist,  $z_0$  is the position of the beam waist and  $z_R$  is the Rayleigh range. Figure 2.1 depicts a typical Gaussian beam profile as the beam propagates along the  $z$ -axis.  $b$  is known as the confocal length and is twice the Rayleigh range, and  $\Theta$  is the divergence angle of the beam in the far-field, both of which are given by

$$b = 2z_R = \frac{2\pi\omega_0^2}{\lambda} \quad \text{and} \quad \Theta \simeq \frac{2\lambda}{\pi\omega_0}.$$

In general, an offset beam is displaced in both the  $x$  and  $y$  directions. For simplicity, however, we will investigate just one degree of freedom i.e. displacement in the  $x$ -direction only. The normalised Hermite-Gauss function (of a non-displaced beam),  $u_n(x, z)$  in  $x$  then becomes:

$$u_n(x, z) = \left(\frac{2}{\pi}\right)^{\frac{1}{4}} \left(\frac{\exp(i(2n+1)\Psi(z))}{2^n n! \omega(z)}\right)^{\frac{1}{2}} H_n\left(\frac{\sqrt{2}x}{\omega(z)}\right) \exp\left(-i\frac{kx^2}{2R_C(z)} - \frac{x^2}{\omega^2(z)}\right). \quad (2.3)$$

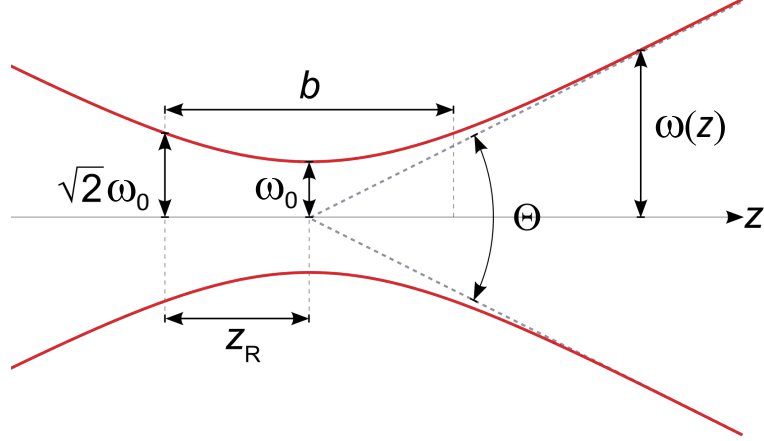


Figure 2.1.: Profile of a Gaussian beam [86] propagating along the  $z$ -axis. Key parameters include the beam waist radius,  $\omega_0$ , beam spot radius,  $\omega(z)$ , divergence angle,  $\Theta$ , Rayleigh range,  $z_R$ , and the confocal length,  $b$ .

### 2.1.2. Fundamental and higher order modes

#### Zero-order modes, $\text{TEM}_{00}$

Since  $n = 0$  for a zero-order mode beam, then the Hermite polynomial becomes  $H_0 = 1$ , and the beam is defined as:

$$u_0(x, z) = \left(\frac{2}{\pi}\right)^{\frac{1}{4}} \left(\frac{\exp(i\Psi(z))}{\omega(z)}\right)^{\frac{1}{2}} \exp\left(-i\frac{kx^2}{2R_C(z)} - \frac{x^2}{\omega^2(z)}\right). \quad (2.4)$$

This equation can be simplified if we initially consider the beam at the waist position to compute key parameters without the loss of generality, and then propagate away from the waist when required. Firstly, the beam size,  $\omega(z)$ , simply becomes the beam waist size,  $\omega_0$ . Secondly, the radius of curvature goes to infinity at the waist, and so the  $R_C$  term in Equation (2.4) can be ignored. Thirdly,  $z$  becomes  $z_0$ , allowing for a zero Gouy phase,  $\Psi(z_0) = 0$ . Equation (2.4) now has the following form at the

waist position:

$$u_0(x, z_0) = \left(\frac{2}{\pi}\right)^{\frac{1}{4}} \frac{1}{\sqrt{\omega_0}} \exp\left(-\frac{x^2}{\omega_0^2}\right). \quad (2.5)$$

### First-order modes, TEM<sub>10</sub>

In the case of a first-order mode beam with  $n = 1$ , it follows that  $H_1 = 2\left(\frac{\sqrt{2}x}{\omega(z)}\right)$ , and is expressed as:

$$u_1(x, z) = \left(\frac{2}{\pi}\right)^{\frac{1}{4}} \left(\frac{\exp(i3\Psi(z))}{2\omega(z)}\right)^{\frac{1}{2}} \left(\frac{2\sqrt{2}x}{\omega(z)}\right) \exp\left(-i\frac{kx^2}{2R_C(z)} - \frac{x^2}{\omega^2(z)}\right). \quad (2.6)$$

At the waist this becomes

$$u_1(x, z_0) = \left(\frac{2}{\pi}\right)^{\frac{1}{4}} \frac{1}{\sqrt{2\omega_0}} \left(\frac{2\sqrt{2}x}{\omega_0}\right) \exp\left(-\frac{x^2}{\omega_0^2}\right). \quad (2.7)$$

Equation (2.7) can be rearranged to obtain:

$$\begin{aligned} u_1(x, z_0) &= \left(\frac{2}{\pi}\right)^{\frac{1}{4}} \frac{1}{\sqrt{\omega_0}} \exp\left(-\frac{x^2}{\omega_0^2}\right) \frac{1}{\sqrt{2}} \left(\frac{2\sqrt{2}x}{\omega_0}\right) \\ &= \underbrace{\left(\frac{2}{\pi}\right)^{\frac{1}{4}} \frac{1}{\sqrt{\omega_0}} \exp\left(-\frac{x^2}{\omega_0^2}\right)}_{=u_0(x, z_0)} \frac{2x}{\omega_0}. \end{aligned} \quad (2.8)$$

The first three factors in Equation (2.8) correspond to the zero-order mode, allowing us to simplify the expression and obtain a relation between a zero-order mode and a first-order mode *at the waist*:

$$\boxed{u_1(x, z_0) = \frac{2x}{\omega_0} u_0(x, z_0).} \quad (2.9)$$

### Away from the beam waist

We now consider the beam away from the waist, for any position  $z$ . A similar relation to the one given in Equation (2.9) can be computed using the full expressions stated in Equations (2.4) and (2.6) for a zero-order and first-order modes. Equation (2.6) can be rewritten as

$$u_1(x, z) = \underbrace{\left(\frac{2}{\pi}\right)^{\frac{1}{4}} \left(\frac{\exp(i\Psi(z))}{\omega(z)}\right)^{\frac{1}{2}} \exp\left(-i\frac{kx^2}{2R_C(z)} - \frac{x^2}{\omega^2(z)}\right) \left(\frac{\exp(i\Psi(z))}{\sqrt{2}}\right)}_{=u_0(x, z)} \left(\frac{2\sqrt{2}x}{\omega(z)}\right). \quad (2.10)$$

Once again, the first three factors correspond to the zero-order mode, producing the following relation between a zero-order mode and a first-order mode *away from the waist position*:

$$\boxed{u_1(x, z) = \exp(i\Psi(z)) \frac{2x}{\omega(z)} u_0(x, z).} \quad (2.11)$$

## 2.2. Beam displacement

If a zero-order beam is displaced by an amount  $h$  along the  $x$ -axis to a new set of coordinates,  $(x', z')$ , as shown in Figure 2.2, then at any position  $z$ , the translated beam is expressed as

$$u_0^t(x', z') = \left(\frac{2}{\pi}\right)^{\frac{1}{4}} \left(\frac{\exp(i\Psi(z))}{\omega(z)}\right)^{\frac{1}{2}} \exp\left(-i\frac{kx^2}{2R_C(z)} - \frac{x^2}{\omega^2(z)}\right). \quad (2.12)$$



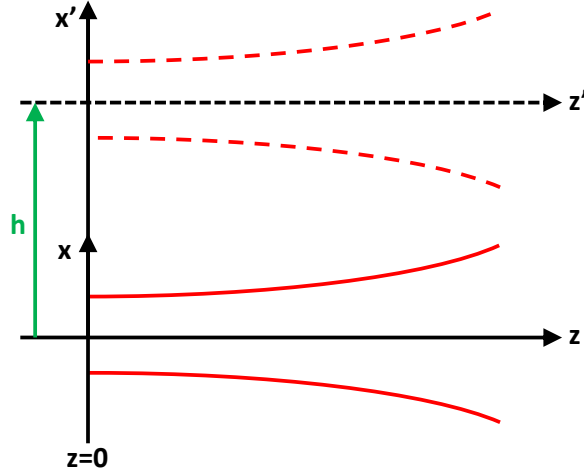


Figure 2.2.: A Gaussian beam of zero-order mode (solid) with coordinates  $x, z$  is displaced by an amount  $h$ . The displaced beam (dashed) is still described as a zero-order mode beam, but has a new coordinate system,  $x', z'$ .

However, the translated beam can still be described in the original coordinate system  $(x, z)$  using the relation  $x' = x - h$ :

$$u_0^t(x, z) = \left(\frac{2}{\pi}\right)^{\frac{1}{4}} \left(\frac{\exp(i\Psi(z))}{\omega(z)}\right)^{\frac{1}{2}} \exp\left(-i\frac{k(x-h)^2}{2R_C(z)} - \frac{(x-h)^2}{\omega^2(z)}\right). \quad (2.13)$$

Expanding Equation (2.13) gives:

$$\begin{aligned} u_0^t(x, z) &= \left(\frac{2}{\pi}\right)^{\frac{1}{4}} \left(\frac{\exp(i\Psi(z))}{\omega(z)}\right)^{\frac{1}{2}} \exp\left(-i\frac{k(x^2 + h^2 - 2xh)}{2R_C(z)} - \frac{(x^2 + h^2 - 2xh)}{\omega^2(z)}\right) \\ &= \left(\frac{2}{\pi}\right)^{\frac{1}{4}} \left(\frac{\exp(i\Psi(z))}{\omega(z)}\right)^{\frac{1}{2}} \exp\left(-i\frac{kx^2}{2R_C(z)} - \frac{x^2}{\omega^2(z)}\right) \exp\left(-i\frac{k(h^2 - 2xh)}{2R_C(z)}\right) \\ &\quad \times \exp\left(-\frac{(h^2 - 2xh)}{\omega^2(z)}\right). \end{aligned} \quad (2.14)$$

The beam described in Equation (2.14) can be *decomposed* using a modal expansion technique as discussed in the next section.

### 2.2.1. Modal decomposition

Misalignments can be decomposed into higher order modes. In other words, a translated beam can be described as a sum of the fundamental mode and the first order mode:

$$E(x, y, z) = a_{00}u_{00}e^{-ikz} + a_{01}u_{01}e^{-ikz}. \quad (2.15)$$

Here,  $a_{00}$  and  $a_{01}$  are amplitude factors which determine how much of the zero order and first order modes contribute to the resulting translated beam. We will also see that these amplitude factors are proportional to the amount of displacement,  $h$ . Referring back to Equation (2.14), we have:

$$\begin{aligned} u_0^t(x, z) &= \underbrace{\left(\frac{2}{\pi}\right)^{\frac{1}{4}} \left(\frac{\exp(i\Psi(z))}{\omega(z)}\right)^{\frac{1}{2}} \exp\left(-i\frac{kx^2}{2R_C(z)} - \frac{x^2}{\omega^2(z)}\right)}_{=u_0(x, z)} \exp\left(-i\frac{k(h^2 - 2xh)}{2R_C(z)}\right) \\ &\times \exp\left(-\frac{(h^2 - 2xh)}{\omega^2(z)}\right). \end{aligned} \quad (2.16)$$

The fundamental mode is in fact described by the first three factors in Equation (2.16), so we can rewrite it as

$$u_0^t(x, z) = u_0(x, z) \exp\left(-i\frac{k(h^2 - 2xh)}{2R_C(z)}\right) \exp\left(-\frac{(h^2 - 2xh)}{\omega^2(z)}\right). \quad (2.17)$$

Due to the fact that the displacement  $h$  is usually very small compared to the beam size<sup>1</sup>, i.e.  $h/\omega \ll 1$ , we can make two approximations. First, we can make the

---

<sup>1</sup>Based on the example given in Section 2.5,  $h = 0.05$  mm and  $\omega = \omega_0 = 10$  mm, and so  $h/\omega = 0.005$ .

assumption that

$$\exp\left(-\frac{h^2}{\omega^2}\right) \approx 1, \quad (2.18)$$

so that Equation (2.17) becomes

$$u_0^t(x, z) = u_0(x, z) \exp\left(-i\frac{k(h^2 - 2xh)}{2R_C(z)}\right) \exp\left(\frac{2xh}{\omega^2(z)}\right). \quad (2.19)$$

The second approximation is the application of a first-order Taylor expansion to the exponential term in Equation (2.19), as follows

$$\exp\left(\frac{2xh}{\omega^2}\right) \approx 1 + \frac{2xh}{\omega^2}, \quad (2.20)$$

and substituting into Equation (2.19) produces the result

$$\begin{aligned} u_0^t(x, z) &= u_0(x, z) \exp\left(-i\frac{k(h^2 - 2xh)}{2R_C(z)}\right) \left(1 + \frac{2xh}{\omega^2}\right) \\ &= \exp\left(-i\frac{k(h^2 - 2xh)}{2R_C(z)}\right) \left[ u_0(x, z) + \underbrace{\frac{h}{\omega} \frac{2x}{\omega} u_0(x, z)}_{=\exp(-i\Psi(z)) u_1(x, z)} \right] \end{aligned} \quad (2.21)$$

Part of the second term in Equation (2.21) can be replaced with the definition of a first-order mode (Equation (2.11)), and we obtain the following description of a translated beam as a sum of zero-order and first-order modes in the form of a decomposed beam:

$$\boxed{u_0^d(x, z) = \exp\left(-i\frac{k(h^2 - 2xh)}{2R_C(z)}\right) \left[ u_0(x, z) + \frac{h}{\omega} e^{-i\Psi(z)} u_1(x, z) \right]}, \quad (2.22)$$

where the superscript  $d$  denotes decomposition. From this it is clear that the translated beam is composed of zero-order and first-order mode terms; we can therefore

deduce that a translated zero-order mode beam can be described by a decomposition into higher-order modes.

It is worth noting that this procedure is applicable for arbitrary displacements, and that the Hermite-Gauss modes are orthonormal and a complete set. Since we consider very small beam displacements, it is possible to compute displacements using only a few number of modes.

Notice that if the beam waist position is considered, where  $R_C = \infty$ ,  $\Psi = 0$  and  $\omega = \omega_0$ , then Equation (2.22) becomes:

$$u_0^d(x, z_0) = u_0(x, z_0) + \frac{h}{\omega_0} u_1(x, z_0) \quad (2.23)$$

## 2.3. Beam comparison

Section 2.2 established that a displaced beam can be described by modal decomposition, yet we need to verify if the same applies to the phase of the beam. The aim of this section is to examine the phase terms of a non-displaced and displaced Gaussian beam as they both travel from one reference plane, undergo grating diffraction, and reach a second reference plane. The displaced beam is then considered as being decomposed into zero-order and first-order modes, after which the phase terms for all three cases can be analysed.

### 2.3.1. Identifying the phase components

In order to observe how accurately a decomposed beam describes a translated beam, a further understanding of the phase terms is required when propagated away from

the waist, i.e.  $z \neq z_0$ . The phase terms are given by the imaginary exponential terms; referring to Equations (2.1) and (2.3), we find that non-translated and translated zero-order beams each contain three such terms. In the following, the subscripts  $f$ ,  $t$  and  $d$  correspond to the fundamental non-translated, translated and decomposed beams respectively.

Using the general form,  $\exp(-i\theta)$ , the phase of a beam,  $\theta$ , at any given point in the  $x$ - $z$  plane is described as:

$$\exp(-i\theta_f) = \exp(-ikz) \exp\left(i\frac{1}{2}\Psi\right) \exp\left(-i\frac{kx^2}{2R_C}\right). \quad (2.24)$$

By substituting  $x$  for  $x - h$ , the same terms hold for translated zero-order beams:

$$\exp(-i\theta_t) = \exp(-ikz) \exp\left(i\frac{1}{2}\Psi\right) \exp\left(-i\frac{k(x-h)^2}{2R_C}\right). \quad (2.25)$$

However, in the case of a decomposed beam it is not so straight-forward, since it is described by a sum of zero-order and first-order modes. In order to describe  $\exp(-i\theta_d)$ , a clear description for  $\theta_d$  is required and computed in the next step.

### Determining the phase terms of a decomposed beam

The electric field of a propagated decomposed beam according to Equation (2.22) is given by:

$$\begin{aligned} E_0^d(x, z) &= \exp\left(-i\frac{k(h^2 - 2xh)}{2R_C}\right) \left[ \left(\frac{2}{\pi}\right)^{\frac{1}{4}} \frac{1}{\sqrt{\omega}} \exp\left(-i\frac{kx^2}{2R_C} - \frac{x^2}{\omega^2}\right) \exp\left(i\frac{1}{2}\Psi\right) \right. \\ &\quad + \frac{h}{\omega} \exp(-i\Psi) \left(\frac{2}{\pi}\right)^{\frac{1}{4}} \frac{1}{\sqrt{2\omega}} \exp\left(-i\frac{kx^2}{2R_C} - \frac{x^2}{\omega^2}\right) \exp\left(i\frac{3}{2}\Psi\right) \left(\frac{2\sqrt{2}x}{\omega}\right) \Big] \\ &\quad \times \exp(-ikz), \end{aligned} \quad (2.26)$$

which can be simplified to

$$E_0^d(x, z) = \exp\left(-i\frac{k(h^2 - 2xh)}{2R_C}\right) \left( \left(\frac{2}{\pi}\right)^{\frac{1}{4}} \frac{1}{\sqrt{\omega}} \exp\left(-i\frac{kx^2}{2R_C} - \frac{x^2}{\omega^2}\right) \exp\left(i\frac{1}{2}\Psi\right) \times \left[\frac{2xh}{\omega^2} + 1\right] \right) \exp(-ikz). \quad (2.27)$$

The last term in the square brackets is purely real and therefore does not contribute to the phase. Equation (2.27) becomes

$$E_0^d(x, z) = \left(\frac{2}{\pi}\right)^{\frac{1}{4}} \frac{1}{\sqrt{\omega}} \exp(-ikz) \exp\left(i\frac{1}{2}\Psi\right) \exp\left(-\frac{x^2}{\omega^2}\right) \times \exp\left(-i\frac{kx^2}{2R_C}\right) \exp\left(-i\frac{k(h^2 - 2xh)}{2R_C}\right). \quad (2.28)$$

The last two exponential factors can be factorised to leave the following:

$$E_0^d(x, z) = \left(\frac{2}{\pi}\right)^{\frac{1}{4}} \frac{1}{\sqrt{\omega}} \exp(-ikz) \exp\left(i\frac{1}{2}\Psi\right) \exp\left(-\frac{x^2}{\omega^2}\right) \exp\left(-i\frac{k(x-h)^2}{2R_C}\right). \quad (2.29)$$

From Equation (2.29), the factors which contribute to the phase of a decomposed beam are identified as

$$\exp(-i\theta_d) = \exp(-ikz) \exp\left(i\frac{1}{2}\Psi\right) \exp\left(-i\frac{k(x-h)^2}{2R_C}\right). \quad (2.30)$$

The phase terms in Equation (2.30) are exactly same as those for a translated beam in Equation (2.25).

### Resulting phase terms

The phase of a beam,  $\theta$ , can be expressed as

$$\theta_{f,t,d} = kz - \frac{1}{2}\Psi + \phi_{f,t,d}. \quad (2.31)$$

The common factor of  $kz - \frac{1}{2}\Psi$  can be omitted to leave  $\phi_{f,t,d}$ , defined for each beam as follows:

$$\textbf{Fundamental beam:} \quad \phi_f = \frac{kx^2}{2R_C}, \quad (2.32)$$

$$\textbf{Translated beam:} \quad \phi_t = \frac{k(x-h)^2}{2R_C}, \quad (2.33)$$

$$\textbf{Decomposed beam:} \quad \phi_d = \frac{k(x-h)^2}{2R_C}. \quad (2.34)$$

These phase terms can now be explored for diffracted beams and displacements smaller than a grating period.

## 2.4. Grating diffraction

Before grating diffraction, the spot size of the beam is considered to be perfectly circular, i.e., the beam size along the  $x$  and  $y$  directions are the same at any given propagation distance  $z$ . The effect of a diffraction grating on a Gaussian beam is considered here in the form of *astigmatism*.

For clarification, consider a model where the propagating beam encounters a diffrac-

tion grating whose surface is parallel to the  $x$ - $z$  plane. For simplicity, the beam waist,  $\omega_0$ , is assumed to be located at the grating, i.e. where  $z = z_0$ . The angles of incidence,  $\alpha$ , and reflection,  $\beta$ , with respect to the grating normal are different, i.e.  $\alpha \neq \beta$ , as depicted in Figure 1.10. This gives rise to an additional optical path length of  $\delta_1$  to the offset incoming, and a missing optical path length of  $\delta_2$  in the offset diffracted beam. Consequently, only the beam parameters along the  $x$ -axis change, whilst those along the  $y$ -axis remain the same, and an elliptical beam spot is produced. A beam diffracted by a grating is astigmatic, with the exception of  $m = 0$  diffraction orders.

However, applying an astigmatism only changes the size of the beam along one axis and does not constitute as a true interaction with a diffraction grating.

### 2.4.1. Beam displacements within a grating period

With the Gaussian model lacking a true grating description, the effects can be demonstrated simply by examining the effects of beam displacement for increasing values of  $h$  within a grating period of  $d = 1666$  nm by computing the phase given by Equation 2.34 (and equivalently for Equation 2.33). The phase is measured at the central optical axis (where  $x = 0$ ) of the modally decomposed beam (or translated beam), using the waist size,  $\omega_0 = 10$  mm, and the resulting phase profile can be seen in Figure 2.3 as the red trace. Regardless of the beam size or ellipticity (caused by a non-symmetric reflection off a diffraction grating), the phase is zero at all times at the beam's central optical axis. The trace displays no periodic phase change over a distance equivalent to the grating period (in contrast to the  $2\pi$  phase change observed in Figure 1.11 due to the intrinsic phase factor), and this is simply because there is no grating for the beam to interact with.



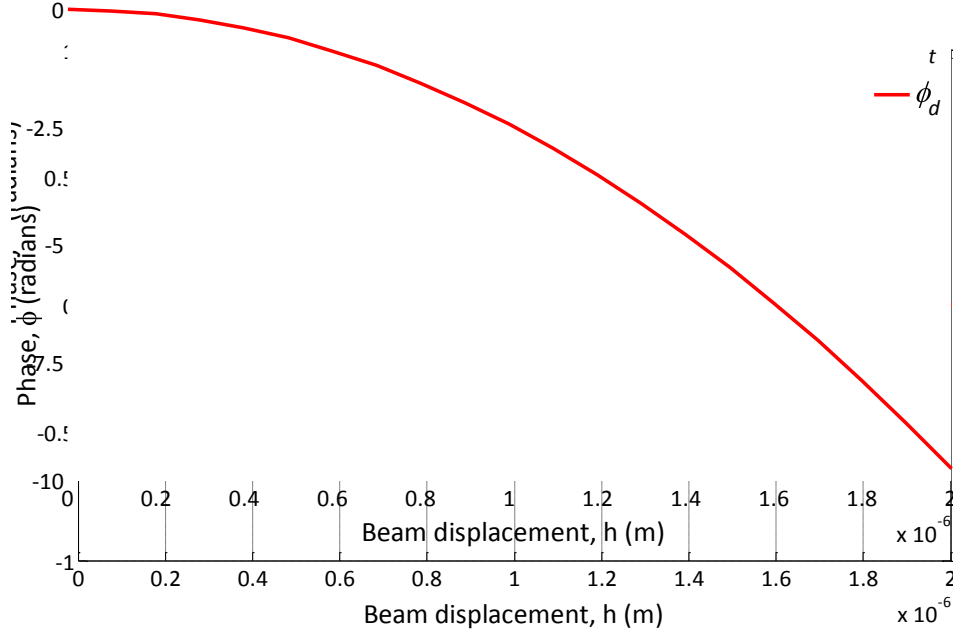


Figure 2.3.: Phase measured at the central optical axis for a translated/modally decomposed beam. Displacement occurs over a grating period,  $d$ , and the parameters are defined as:  $h = 0.05$  mm,  $z = 0.5$  m,  $\lambda = 10^{-6}$  m and  $\omega_0 = 10$  mm. The trace does not exhibit a periodic phase noise of  $2\pi$  radians.

We have established that the phase terms which describe a modally decomposed beam are the same as those defined by a translated beam, and thus there is no need for a direct comparison of phase between a translated beam and a modally decomposed beam. We can, however, compare the differences in the electric field of the two beams, as demonstrated in the next section.

## 2.5. Comparison of electric field amplitudes

The electric field of a translated zero-order is given by:

$$\begin{aligned}
 E_0^t(x, z) = & \left(\frac{2}{\pi}\right)^{\frac{1}{4}} \frac{1}{\sqrt{\omega}} \exp\left(-i \frac{kx^2}{2R_C(z)} - \frac{x^2}{\omega^2(z)}\right) \exp\left(-i \frac{k(h^2 - 2xh)}{2R_C(z)}\right) \\
 & \times \exp\left(i \frac{1}{2}\Psi\right) \underbrace{\exp\left(-\frac{(h^2 - 2xh)}{\omega^2(z)}\right)}_{F_t} \exp(-ikz), \quad (2.35)
 \end{aligned}$$

and the electric field for a modally decomposed beam (according to Equation (2.27)) is described as:

$$\begin{aligned}
 E_0^d(x, z) = & \exp\left(-i \frac{k(h^2 - 2xh)}{2R_C(z)}\right) \left(\left(\frac{2}{\pi}\right)^{\frac{1}{4}} \frac{1}{\sqrt{\omega}} \exp\left(-i \frac{kx^2}{2R_C(z)} - \frac{x^2}{\omega^2(z)}\right)\right) \\
 & \times \exp\left(i \frac{1}{2}\Psi\right) \underbrace{\left[\frac{2xh}{\omega^2(z)} + 1\right]}_{F_d} \exp(-ikz). \quad (2.36)
 \end{aligned}$$

Notice that the only difference between the two expressions is the complete factor indicated as  $F_t$  in Equation (2.35), which was approximated in Section 2.2.1 and resulted in the approximated factor,  $F_d$ , in Equation (2.36). Although the approximation holds for small displacements, we can observe the effects of this approximation for much larger beam displacements. We are only concerned with the factors  $F_t$  and  $F_d$  for comparison, since all of the other terms in Equations (2.35) and (2.36) are identical.

From the expression for a translated beam, we let

$$F_t = \exp\left(-\frac{(h^2 - 2xh)}{\omega^2(z)}\right), \quad (2.37)$$

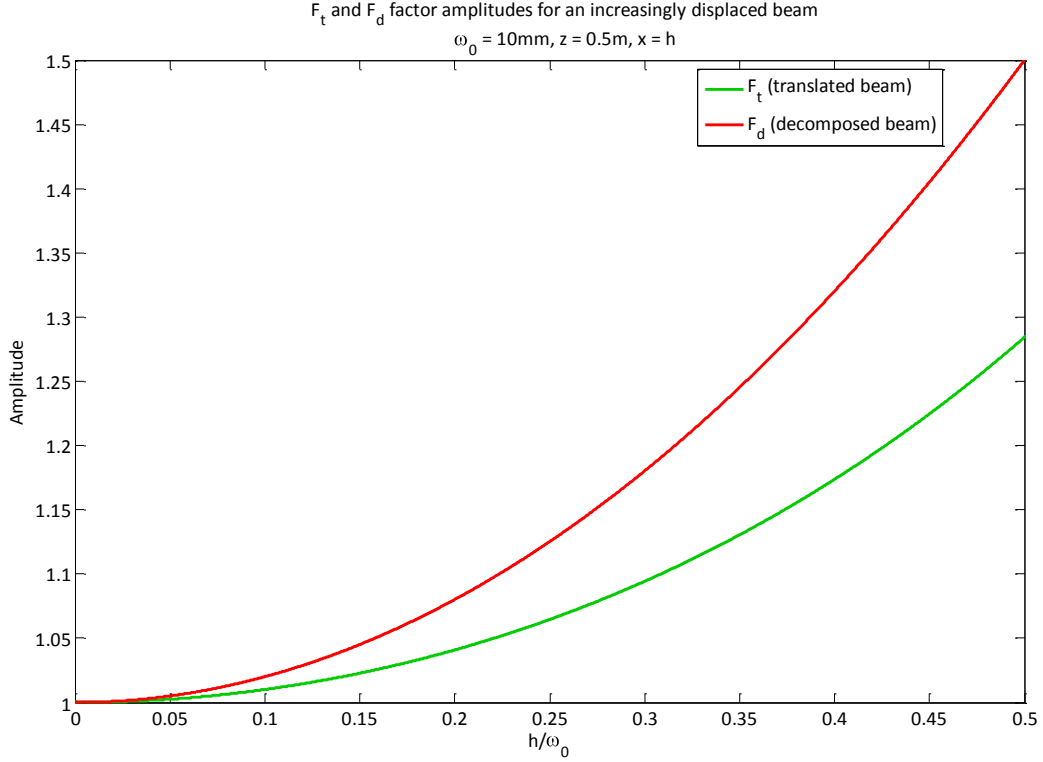


Figure 2.4.: Amplitude of the  $F_t$  factor (green) and the  $F_d$  factor (red) for continuously increasing beam displacement,  $h$ . The factors are computed at the central optical axis of the beam, using the parameters  $\lambda = 10^{-6}$  m,  $\omega_0 = 10$  mm and  $z = 0.5$  m.

and for a modally decomposed beam we have

$$F_d = \frac{2xh}{\omega^2(z)} + 1. \quad (2.38)$$

These factors were computed in Matlab for a typical Gaussian beam with the following values:  $\lambda = 1 \times 10^{-6}$  m,  $\omega_0 = 10$  mm and  $z = 0.5$  m<sup>2</sup>, as seen in Figure 2.4. The green and red lines represent  $F_t$  and  $F_d$ , respectively, as measured at the central optical axis of the beam. The  $x$ -axis shows a displacement from zero up to half of the beam radius, and the approximated factor of  $F_d$  clearly deviates further away

<sup>2</sup>The value of  $z = 0.5$  m was chosen to match typical beam propagation distances observed during table-top experiments.

from the  $F_t$  factor at such large beam displacements.

If we now consider a typical displacement where  $h = 0.05$  mm, then  $h/\omega_0 = 0.005$ , and we see from Figure 2.4 that the approximation for the decomposed beam is highly comparable to the factor for the translated beam in this region.

This can be understood more clearly by considering the difference between  $F_d$  and  $F_t$  relative to  $F_t$ , which is illustrated by the purple trace in Figure 2.5 (using the same beam parameters). Again, for larger  $h$ , the relative difference increases, showing that the  $F_d$  approximation deviates further away from  $F_t$ . Yet for a displacement of  $h = 0.05$  mm, the relative difference was equal to  $2.5 \times 10^{-5}$ , which is an extremely small number, implying that the difference in the electric field between a translated beam and a decomposed beam is almost negligible for very small beam displacements.

## 2.6. Analytical results

The phase terms between a translated beam and a modally decomposed beam are the same, regardless of the beam's ellipticity (due to grating diffraction). We find that the electric field amplitude of a modally decomposed beam is highly comparable to that for a translated beam at for very small displacements - in realistic terms, the degree to which a beam experiences misalignment is minute, typically less than 0.5% of the beam size. The exceptionally small difference between the two expressions suggests that the resulting electric field from modal decomposition is very close to that of a translated beam, and that the technique of decomposing a beam into higher order modes is a very good approximation for describing small beam displacements.

As discussed in Section 1.5.3, a beam diffracted by a grating must introduce a substantial phase change of  $2\pi$  radians when displaced over a grating period,  $d$ , under

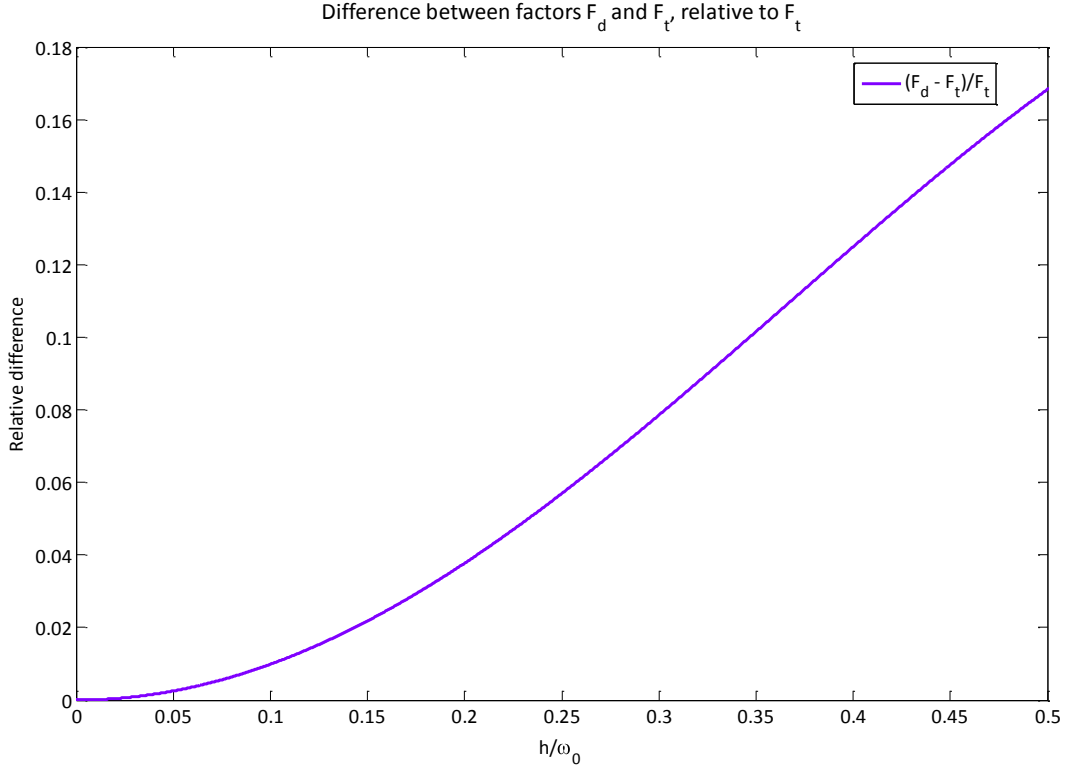


Figure 2.5.: Difference between  $F_d$  and  $F_t$  relative to  $F_t$ , with increasing beam displacement,  $h$ . The parameters are:  $\lambda = 10^{-6}$  m,  $\omega_0 = 10$  mm and  $z = 0.5$  m.

a geometrical planewave consideration. Yet within the Gaussian model, the absence of a proper description for a diffraction grating means that when a beam is displaced either through a geometrical translation or a modal decomposition, the phase (as described by Equation (2.33) or (2.34)) at the central optical axis always remains constant (see Figure 2.3). The  $2\pi$  phase change is absent within the Gaussian-based framework, contrary to the phase change predicted by Equation (1.20). It stands to reason that the intrinsic phase factor is missing because the diffraction grating element itself has not been fully described, and thus there is no proper interaction between the beam and the grating to generate the appropriate phase changes.

However, we have identified that the phase terms in a translated beam and a modally decomposed beam are the same, and this applies regardless of the beam ellipticity;

the similarity between a translated and decomposed beam is not dependent solely on the beam size but on the amount of displacement relative to the beam size.

In order to further understand the role of the intrinsic phase factor within the Gaussian model presented, and for the purpose of verifying the technique of modal decomposition, we must first ascertain that the phase in the individual zero-order and first-order modes of a diffracted beam are, in fact, the same. In the next chapter, we determine whether the phase is influenced by the beam shape using an experimental setup.

## **Chapter 3.**

# **EXPERIMENTAL DEMONSTRATION OF PHASE-MODE INDEPENDENCY**

In Chapter 2, a theoretical analysis of a Gaussian beam was performed, and the effect of beam displacement on the phase of the beam was examined. The beam was displaced using two methods - through a geometric translation and a modal decomposition. Although both methods demonstrated identical descriptions for the phase, it was found that the Gaussian framework does not contain the phase change associated with the intrinsic phase factor.

In this chapter we use experimental means to determine if the phase of zero-order and a first-order diffracted beams are the same, and therefore establish whether or not the phase of a diffracted beam is dependent on the beam shape (or mode). This is achieved by observing an interference pattern created by two zero-order mode beams, one of which is imprinted by a diffraction grating, and comparing it to the

interference pattern using two first-order mode beams, also one of which is imprinted by grating diffraction. Any difference in the phase of the two mode orders would be indicated by a shift in phase between the two interference patterns, or fringes.

Section 3.1 introduces the properties of the specific diffraction grating used as part of the experimental setup. In Section 3.2 we present the details of the table-top experiment: a Mach-Zehnder interferometer with a reflective diffraction grating contained within one of the interferometer arms. The concept of the frequency stabilisation technique is provided in Section 3.3, required to lock the modecleaner and the main interferometer. We describe a method of dual-mode locking in Section 3.4, enabling a stable lock whilst continuously switching between zero-order and first-order modes.

### 3.1. Blazed gratings

Usually for a diffraction grating with non-defined efficiencies, such as the one shown in Figure 1.7, most of the energy from the incident beam is contained in the zeroth diffraction order, while the power in the higher diffraction orders weaken progressively. Since the aim of this work is to investigate the effects on a diffracted beam, we require a grating specifically designed for a high efficiency in the first diffraction order, unlike the 3-port gratings described mainly in Section 1.5.2. This is achieved with a *blazed* diffraction grating, which are available commercially.

A blazed grating lends its name to the shape of the grooves which have an asymmetric ‘sawtooth’ profile, as illustrated in Figure 3.1. This particular groove design consequently shifts the diffraction envelope such that the diffraction peak (of maximum power) coincides with a higher diffraction order. The grating efficiency can therefore be optimised in the first diffraction order for a specific wavelength.



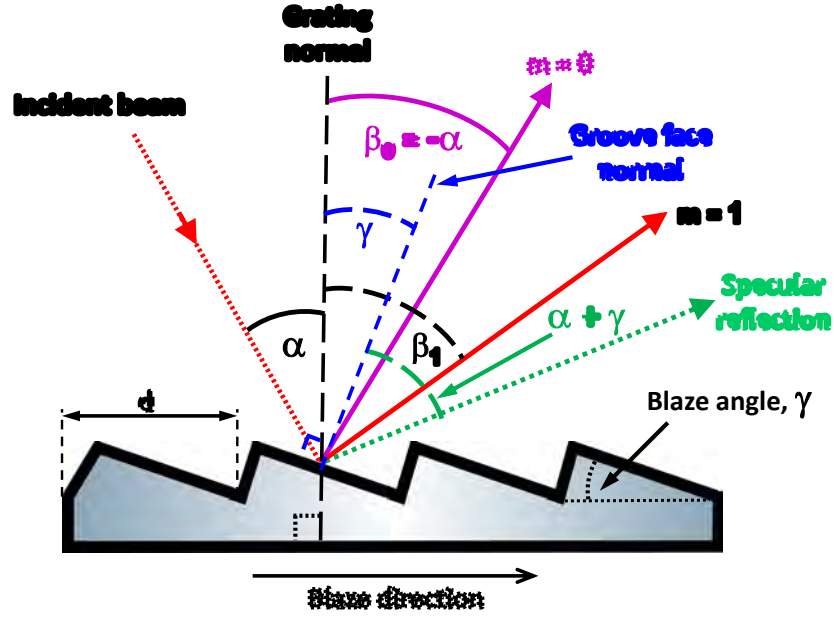


Figure 3.1.: Blazed gratings are optimised in the first diffraction order, with maximum efficiency for a given wavelength determined by the blaze angle,  $\gamma$ , but are still governed by the grating equation.

Despite the nature of the blazed grooves, the standard grating equation (Equation (1.14)) applies as normal; the various diffraction orders are located accordingly with respect to the grating normal, including the zeroth diffraction order whose beam properties are identical to the incident beam.

However, the groove geometry stipulates that the groove surface normal is different to the grating normal, thereby separating the specular reflection (and hence the diffraction peak) from the zeroth diffraction order. By selecting the correct blaze angle,  $\gamma$ , the first diffraction order will lie close to the specularly reflected beam, falling within the diffraction peak to obtain increased power.

## 3.2. A Mach-Zehnder setup to observe phase effects

Through experimental means, we want to distinguish the phases between diffracted beams of zero-order and first-order modes. This is achieved by interfering two beams (of the same mode), where one of the beams is imprinted by diffraction from a grating. Several interferometer configurations were considered, such as the Michelson and Sagnac interferometers, but for the purpose of studying the relative phase between two interference patterns for different modes, the Mach-Zehnder (MZ) interferometer is ideal. It has the advantage of being quick and fairly simple to set up, and allows for flexibility in the geometrical layout, as seen in Figure 3.2. Before entering the main MZ interferometer, the input beam is purified via a triangular mode cleaner (MC) to yield a single and pure beam mode. The input and output beamsplitters (BS) are partially reflective mirrors designed for 50% transmission and reflection. At the input BS, the beam is split into two arms of equal length - one arm includes a piezoelectric transducer (PZT) and the other arm contains the diffraction grating, denoted as the ‘PZT’ path and the ‘grating’ path, respectively. Both beams recombine at the output BS resulting in two superimposed output beams. One output beam is incident on the ‘east’ photodetector (PD) and the second output beam is incident on the ‘south’ PD, and both beams are  $180^\circ$  out of phase with respect to each other.

### 3.2.1. Mode cleaner

The input laser beam in our lab is well collimated with a waist size of  $1183\ \mu\text{m}$ . However, in order for the MC to operate successfully, the beam entering the MC must have specific beam parameters. For our particular MC, the beam was required to have a waist size of  $371\ \mu\text{m}$  (and hence a Rayleigh range of  $0.41\ \text{m}$ ), with the

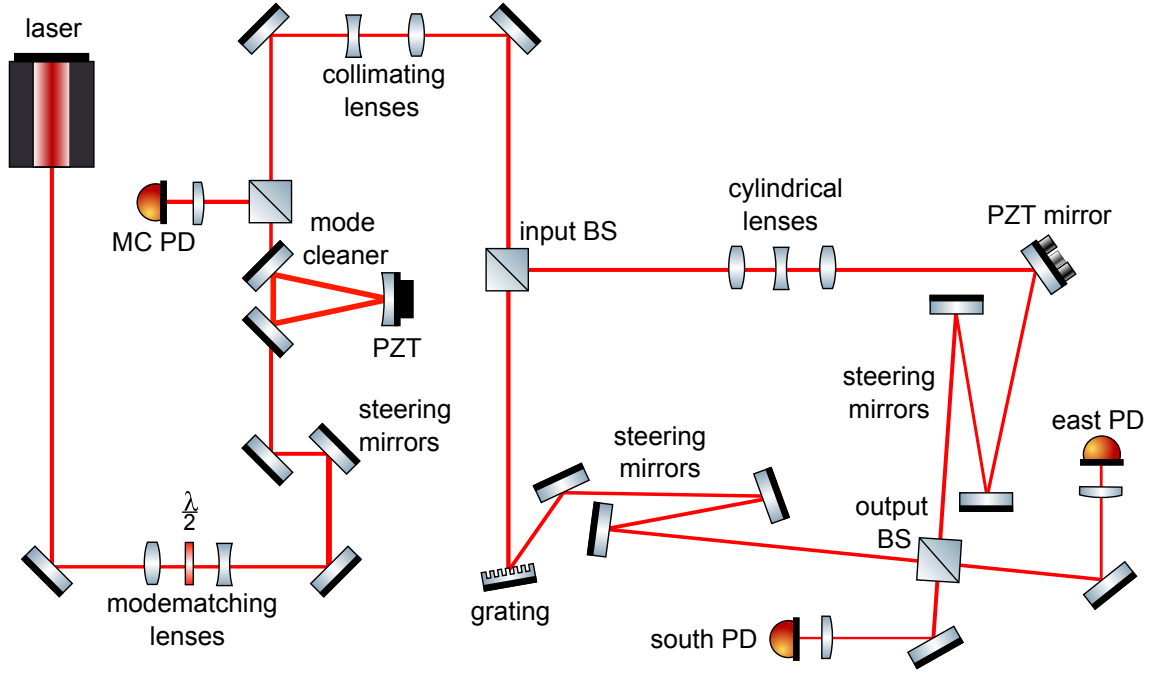


Figure 3.2.: Layout of a table-top grating Mach-Zehnder interferometer. The mode cleaner (MC) is locked using a piezoelectric transducer (PZT) and a photodetector (PD), allowing a single mode beam to pass through. The beam is split into two arms by an input beamsplitter (BS), where one arm contains a diffraction grating and the other arm includes a PZT mirror, and the beams recombine at an output BS and are detected by the east and south PDs. The PZT mirror causes fluctuations in the length of the arm to create interference signals.

waist located centrally between the input and output mirrors of the MC. A JamMt simulation tool [87] was used to compute the best combination of lenses for mode-matching the laser beam into the MC. Mode-matching was achieved using a convex lens with  $f = 100$  mm and a concave lens with  $f = -50$  mm (see Figure A.1 in Appendix A for details).

The alignment of the beam upon entering the MC is crucial - the beam must be incident on the input mirror of the MC at a very precise point and angle. This is to ensure that the beam is reflected at the correct angles within the MC and

completes a round-trip before exiting the MC. A combination of steering mirrors guides the beam into the MC and can be adjusted to alter the beam alignment, thereby amplifying the resonance of the desired mode. The MC is tuned using a PZT - when a voltage is applied to the PZT, the shape of the material deforms proportionally, thereby adjusting the position of the PZT mirror. Although these movements are extremely tiny, it is enough to alter the round-trip distance of the circulating light inside the MC, allowing one specific mode to exit and suppressing all other modes. The distance for one round-trip within the triangular MC is 0.42m, with a free spectral range (FSR) of 714 MHz and a finesse of  $\mathcal{F} = 307 \pm 20$  [88] (see Figure 3.4(a)).

The exiting beam from the MC encounters a beamsplitter, where the reflected beam is sensed by a PD and the signal is used as part of a feedback loop to lock the MC to a particular beam mode (as discussed in Section 3.3). The transmitted beam from the beamsplitter continues to the main interferometer setup, travelling through another pair of collimating lenses. The lenses have the same focal lengths as the mode-matching lenses but in reverse order, ensuring a collimated beam once more with a waist size of  $1036 \mu\text{m}$  (see Appendix A.2 for the measured beam profile). The input BS then separates the beam into two arms: the grating path and the PZT path.

### 3.2.2. Mach-Zehnder, grating path

The beam transmitted through the input BS forms one arm of the Mach-Zehnder interferometer, referred to as the grating path. The grating used in this setup is orientated to lie in the  $x$ - $y$  plane, with the grooves aligned parallel to the  $y$ -axis, and  $\alpha = 10^\circ$  for the incident beam with respect to the grating normal. The grating is located on a dual-axis translation stage to enable motion in two degrees of freedom:

along the  $x$ -axis for lateral translation, and along the  $z$ -axis. The high-resolution manual actuators allow for grating displacements smaller than the groove spacing, with incremental steps as small as 500 nm. Note that the purpose of the translation stage was for grating and beam alignment during the experimental setup, and not to investigate grating displacements.

The groove spacing of the grating was chosen to be the same order as the wavelength of the laser. A square, ruled grating with 600 grooves/mm was chosen, giving a groove spacing of  $d = 1666.7$  nm. The grating is ‘blazed’ to produce a sawtooth profile, illustrated in Figure 3.3. The blaze angle determines the wavelength at which the grating exhibits high diffraction efficiency. In this case, a blaze angle of  $\gamma = 17.45^\circ$  produces an approximate efficiency of 70% for a 1064 nm wavelength.

The grating was aligned to the incident beam such that for the diffracted beams, maximum power occurred in the first diffraction order ( $m = +1$ ). This was found to occur when the incident beam was set at an angle of  $\alpha = 10^\circ$  to the grating normal. Using the grating equation, the beam was found to have a first order diffraction angle of  $\beta_1 = 27.69^\circ$ . Angle conventions imply that both  $\alpha$  and  $\beta$  are positive, since they are on the same side of the grating normal.

A beam reflected off a grating experiences a change in beam parameters along the  $x$ -axis<sup>1</sup> (i.e. parallel to the surface of the optics table). More importantly, these new parameters include a new waist size and waist position (if the beam were to be traced backwards). A Matlab script was used to take the original parameter inputs, namely the waist size and propagation distances (details can be found in Appendix A.3). The beam was propagated and reflected off the grating using the angles specified in Figure 3.3, and the new beam parameters along the  $x$ -axis were computed. The waist size and Rayleigh range before and after diffraction are as

---

<sup>1</sup>Note that the beam profile in the  $y$ -direction remains unchanged.

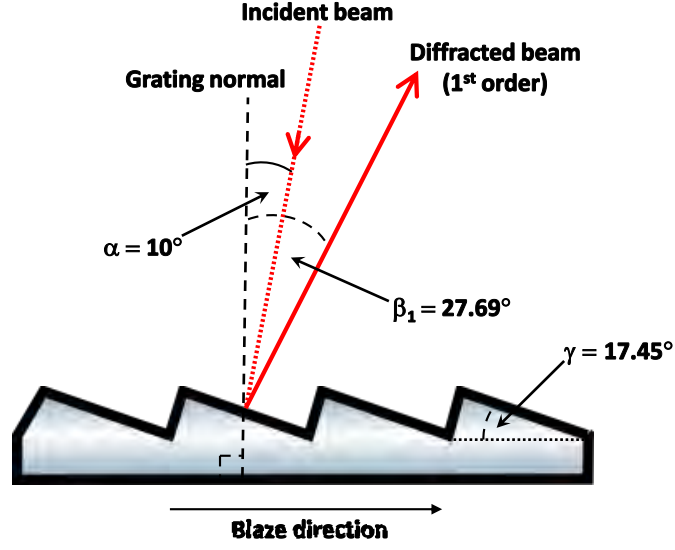


Figure 3.3.: Orientation of the blazed grating. When incoming beam is incident at an angle of  $\alpha = 10^\circ$ , first order diffraction occurs at  $\beta_1 = 27.69^\circ$  to the grating normal.

follow:

	Before diffraction		After diffraction
$\omega_0$	$1036 \mu\text{m}$	$\rightarrow$	$950 \mu\text{m}$
$z_R$	$2.29 \text{ m}$	$\rightarrow$	$1.92 \text{ m}$

Note that the effect of diffraction has caused the previously circular beam cross-section to *decrease* along the  $x$ -direction, resulting in an astigmatic beam.

A turning mirror is situated after the grating, guiding the beam to a pair of steering mirrors. These are set slightly further apart than those for the MC so as to provide greater sensitivity during mirror adjustment for beam alignment at the output BS.

### 3.2.3. Mach-Zehnder, piezoelectric transducer path

The beam reflected from the input BS forms the second arm of the Mach-Zehnder interferometer, designated as the PZT path. Since the beam in the PZT path is unaffected by any diffraction effects, the beam retains a circular beam shape, while the beam in the grating path has an elliptical beam shape due to grating diffraction. It is important that when both beam paths recombine at the output BS, their beam shapes are as similar as possible so as to obtain a high contrast in interference and therefore a strong signal detection by the output PDs. Therefore one of two things must be done: either an astigmatism is applied to the beam in the PZT path to match the astigmatic beam in the grating path, or the elliptical beam shape in the grating path is converted back to a circular beam shape. Both methods can be achieved using a ‘telescope’ of three cylindrical lenses,<sup>2</sup> which change the beam parameters along one axis only.

Due to space constraints of the optical layout, the method of converting the beam shape from circular into elliptical in the PZT path was chosen, and this required a change in the beam parameters along the  $x$ -direction only. The mode-matching simulation tool computed the best combination of cylindrical lenses (see Figure A.2 in Appendix A for specific lens properties and positions).

Once the cylindrical lenses were positioned in the PZT path, as seen in Figure 3.2, a laser beam profiler was used to observe the spatial intensity profile of the beam. The beam profiler captured a 2-D image of the beam to be captured, displaying the intensity patterns and dimensions of the beam spot in the  $x-y$  plane on a laptop. To ensure that the converted astigmatic beam matched the beam profile of the grating path, the beam profiler was placed in various positions along the optical beam path  $z$  of both the grating arm and the PZT arm, and measurements of the beam shape

---

<sup>2</sup>Two lenses are usually sufficient, but if space is limited then a third is necessary.

were recorded and compared. The cylindrical lenses were adjusted back and forth along the  $z$ -axis by fractional amounts until the beam diameter along the  $x$ -axis in the PZT path matched as closely as possible the beam diameter in the grating path along different positions of  $z$ .

Once the beam profiles of the two paths were well matched, a final measurement was carried out to compare the ellipticity in each path. The beam profiler was placed 0.7 m away from the input BS along the grating path, which was located just in front of the first steering mirror. After averaging over a 10-second period, the diameter along the  $x$ -axis ( $2\omega_x^{gr}$ ) of the diffracted beam was recorded as  $(2058 \pm 15) \mu\text{m}$ , and the diameter along the  $y$ -axis ( $2\omega_y^{gr}$ ) was  $(2195 \pm 15) \mu\text{m}$ , resulting in an ellipticity of  $\varepsilon_{gr} = 0.937$ . The profiler was then placed 0.7 m away from the input BS along the PZT path, just in front of the PZT mirror itself. In the  $x$ -direction, the diameter was found to be  $2\omega_x^{PZT} = (2053 \pm 15) \mu\text{m}$ , with a diameter along the  $y$ -direction as  $2\omega_y^{PZT} = (2205 \pm 15) \mu\text{m}$ , giving  $\varepsilon_{PZT} = 0.931$ . The beam shape of both beam paths was therefore confirmed to be very similar.

After passing through the cylindrical lenses, the beam is reflected off a PZT mirror, followed by a pair of steering mirrors directing the beam to the output BS. Ramping the PZT mirror caused tiny fluctuations in the length of the PZT path, thereby creating an interference pattern when the two beam paths recombined at the output BS.

### 3.3. Cavity resonance stabilisation techniques

Frequency fluctuations occur naturally in a laser, and so some form of frequency stabilisation is required in order to ‘lock’ a system to a specific resonance frequency, and this is achieved using a feedback control loop. In the case of locking an MC



with respect to the laser, the laser intensity is measured by the PD at the MC's output, and the signal is fed back to the MC's PZT mirror, which then adjusts itself accordingly to hold the cavity on resonance. The basic concepts of this form of feedback control are introduced in the following sections. In the following example we use a simple linear cavity, otherwise known as a Fabry-Perot cavity, instead of a triangular mode cleaner for simplicity.

### 3.3.1. Analogue cavity resonance stabilisation

A linear cavity, such as the one shown in Figure 3.5, is said to be on resonance if the laser frequency,  $\nu_r$ , is an integer multiple of the free spectral range (FSR):  $\nu_r = N\Delta\nu_{fsr}$ . The FSR is defined as  $\Delta\nu_{fsr} = c/2L$ , where  $L$  is the length of the cavity. In other words, resonance occurs when an integer number of wavelengths of the laser light is equal to twice the length of the cavity<sup>3</sup>. A plot of the light transmission against frequency reveals evenly spaced resonance peaks, as shown in Figure 3.4(a). The finesse,  $\mathcal{F}$ , is the 'quality factor' of the peak, where the solid and dashed transmission lines represent cavities with a high and low finesse, respectively. The finesse is described as the ratio between the FSR and the linewidth of the peak (also known as the full-width half-maximum, FWHM). For a further understanding of modulation, see Appendix B.

#### The feedback loop

Locking a system through feedback control is the process of taking measurements of the beam's intensity derivative and feeding it back either to the laser or the MC PZT in order to hold the cavity on resonance. For our setup, the PD is said to be

---

<sup>3</sup>Or one round-trip distance for a triangular MC.

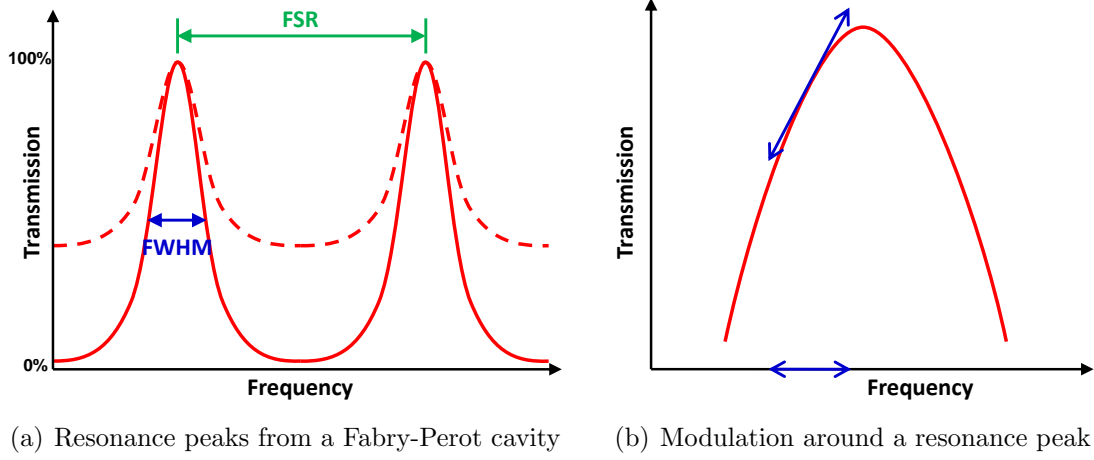


Figure 3.4.: (a) Resonance peaks formed by light transmission through a Fabry-Perot cavity as a function of frequency. When transmitted light is maximum, reflected light from the cavity is minimum and vice versa, and these occur at very specific frequencies. The solid red line corresponds to a high-finesse cavity, and the dashed red line represents a relatively low-finesse cavity. (b) Below resonance, modulating the frequency a small amount causes the transmitted light to vary in amplitude over a larger range. Above resonance, the transmitted light will vary  $180^\circ$  out of phase. By modulating and observing the behaviour of the transmitted light, it is possible to distinguish which side of resonance the system has drifted to.

measuring the signal in *transmission*, since the laser beam is transmitted through the MC, and the transmitted light is held at maximum resonance.

An alternative but very similar method is to locate the PD at the input mirror of the cavity to detect the *reflected* beam, as demonstrated in Figure 3.5 - this technique is known as the Pound-Drever-Hall (PDH) scheme [89]. Using the PDH method, the reflected signal is held at minimum intensity, meaning that the light transmitted through the cavity is automatically held at maximum resonance.

The reason why transmission was chosen for our setup is due to space constrictions of the optical layout. The following example given in Figure 3.5 uses the PDH

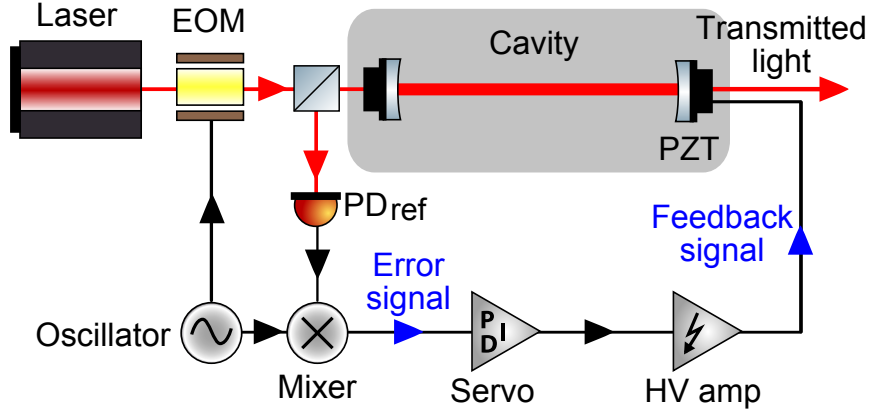


Figure 3.5.: Demonstration of a feedback control loop to lock a simple Fabry-Perot cavity on resonance using the Pound-Drever-Hall technique. An oscillator modulates the laser frequency through an electro-optic modulator (EOM). The reflected signal from the cavity is detected by a photodetector (PD<sub>ref</sub>) and sent to a mixer, which is then multiplied with the oscillator signal. The output is the error signal, which enters the servo amplifier. The resulting feedback signal is amplified by the high-voltage (HV) amplifier and finally fed back to the piezoelectric transducer (PZT), holding the cavity at resonance and therefore in a stable lock.

technique to explain the practicalities of feedback control - additional information can be found in [1].

A brief description of the feedback control loop shown in Figure 3.5 begins with an oscillator which modulates the phase<sup>4</sup> of the laser via an electro-optic modulator (EOM). The reflected signal from the cavity is detected by the photodetector in reflection (PD<sub>ref</sub>) and enters a mixer as one of its inputs. The mixer receives a second input signal from the oscillator and multiplies the two input signals. Contained within the mixer is a low-pass filter which extracts the appropriate signal from the

<sup>4</sup>Phase and frequency modulation both have the same results, but phase modulation is easier to carry out in practice and the mathematical analysis is more simple.

product of the inputs. The output from the mixer is called the *error signal*,  $\varepsilon$ , and proceeds to the servo amplifier (see Appendix C for the servo circuit schematics). The servo acts to drive the error signal to zero in the form of a *feedback signal*, which goes on to be amplified through the high-voltage amplifier (HV amp), and the resulting feedback signal is fed back to the PZT situated on the output mirror of the cavity. The feedback loop is now complete and the system is said to be locked on resonance. Appendix B provides a description of the fields for the carrier and sideband frequencies (Section B.2), followed by a derivation for the power in the reflected beam (Section B.3) and details on obtaining the error signal (Section B.4).

### 3.3.2. Mode-cleaner control loop

Referring back to our setup, a feedback control system similar to the PDH example in Figure 3.5 was employed for the MC using high frequency modulation, illustrated in Figure 3.6. The transmitted light from the output of the MC is picked off by a BS and detected by the  $\text{PD}_{\text{trans}}$ , providing an AC signal for the mixer. The oscillator modulates at 15 MHz, and the mixer is also optimised to operate at 15 MHz. The error signal passes through the servo, and the resulting feedback signal is fed back into the PZT of the MC, thus completing the feedback loop. The feedback signal triggers a deformation of the PZT, adjusting the position of the PZT's mirror surface so as to maintain the correct round-trip distance inside the MC. This allows a particular mode to resonate, thereby locking the MC on resonance with respect to the laser.

A CCD camera was inserted in the beam path just before the input BS of the interferometer so that the image of the shape of the beam spot emerging from the MC could be observed directly on a monitor. A cavity scan was performed using the ramping function on the servo which applies a triangular wave signal to

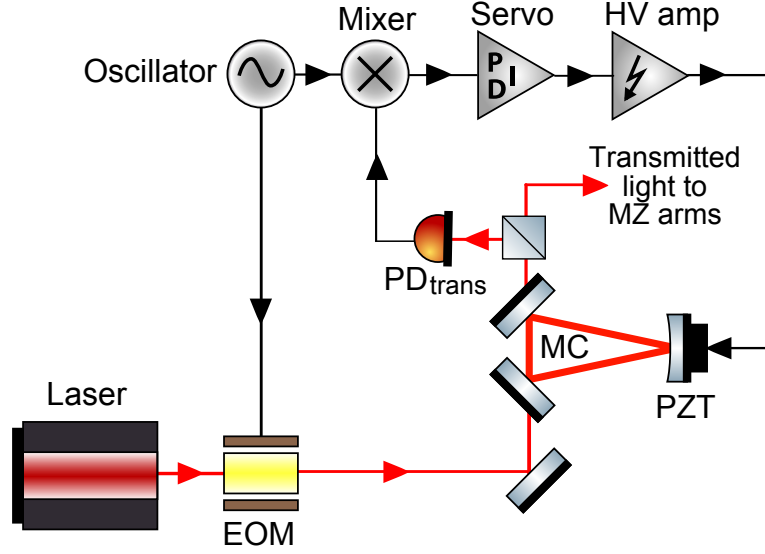


Figure 3.6.: Feedback control system used for locking the triangular mode cleaner (MC) on resonance with respect to the laser. The transmitted signal from the MC is detected by the photodetector ( $PD_{trans}$ ) and fed into a mixer together with a modulation signal from the oscillator. The mixer outputs an error signal, which enters a servo and is amplified by the high-voltage amplifier (HV amp). The resulting feedback signal is fed back to the piezoelectric transducer (PZT), whose position continually adjusts so that the required mode resonates and exits the MC.

the MC's PZT (green trace in Figure 3.7), causing the PZT to move back and forth and sweep through the various resonance modes. During the cavity scan, the monitor reveals a whole range of beam shapes with varying Hermite-Gauss (and some Laguerre-Gauss) modes. Through careful alignment of the beam entering the MC, the resonance peaks corresponding to zero-order modes were amplified while higher-order modes were suppressed, as depicted by the red trace in Figure 3.7. The blue trace in Figure 3.7 represents the error signal, with steep zero-crossings coinciding with the highest resonance peaks. Note that the shape of the error signal is typical for high-frequency modulation, as seen in Figure B.2(a).

Without the ramp function, the position of the PZT can be manually adjusted using

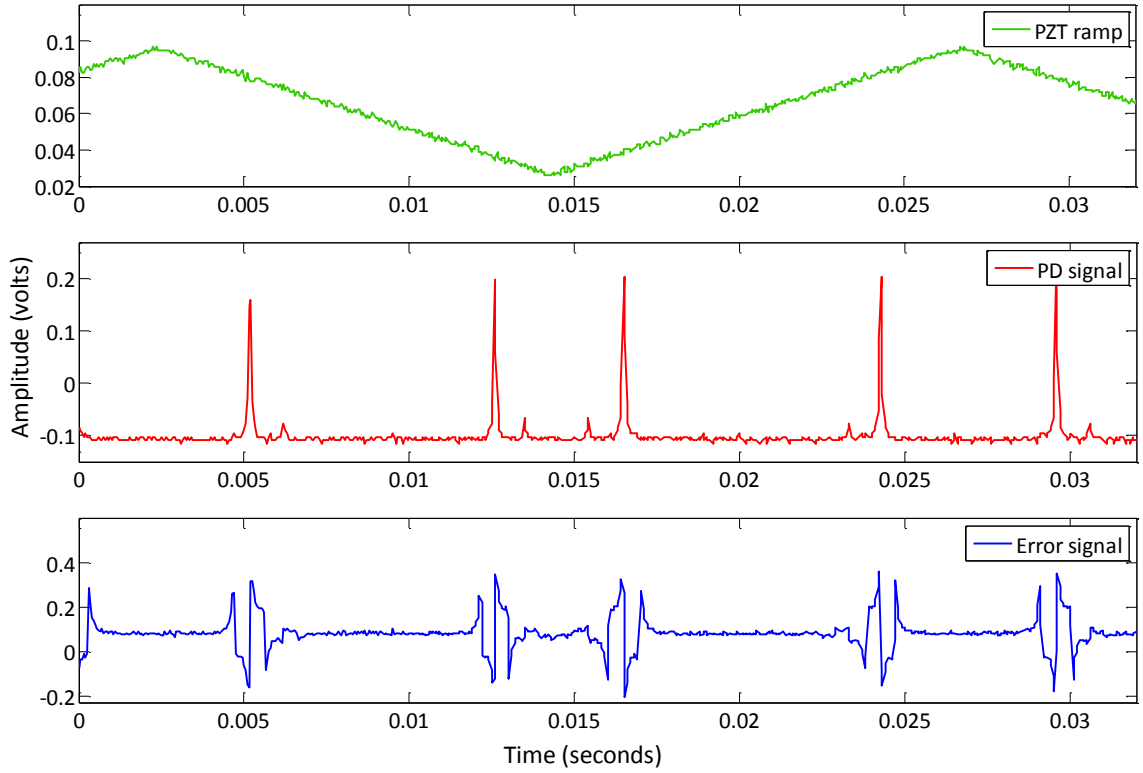


Figure 3.7.: A cavity scan by ramping the piezoelectric transducer back and forth (green) causes zero-order modes to resonate within the mode cleaner (MC) cavity, producing resonance peaks (red). High-frequency modulation creates an error signal (blue) at each resonance peak, and is used to lock the MC on resonance.

an offset dial on the servo to locate the required mode, such as the zero-order mode, by observing the CCD image. When the PZT is in the correct position for zero-order mode resonance, the image of a zero-order mode appears on the monitor as a bright circular beam spot. Simultaneously, the output signal from the MC's PD displays a sudden increase in power on an oscilloscope. At this precise point, the feedback control is engaged by switching on the integrator switches on the servo, holding the PZT in position. At this point the MC is said to be locked, and this is clear from the presence of a consistent beam spot image from the monitor without drifting into other modes.

### 3.3.3. Mach-Zehnder control loop

The arms of the MZ setup can also be locked to either the bright or dark fringe operation point by using one of the output PDs and the PZT mirror contained in one of the arms. The feedback control system can be seen in Figure 3.8, and works on the same principle as that described in Section 3.3.2 for the MC, with a couple of differences.

Firstly, the phase modulation is not applied through an EOM but to the PZT via the HV amplifier (as is the feedback signal). Secondly, a low-frequency modulation was used (as opposed to the high-frequency modulation of 15 MHz used in the MC, which would have required an extra EOM). The PZT had a resonance frequency of approximately 2 kHz, and so the modulation frequency was set between 1 - 2 kHz.

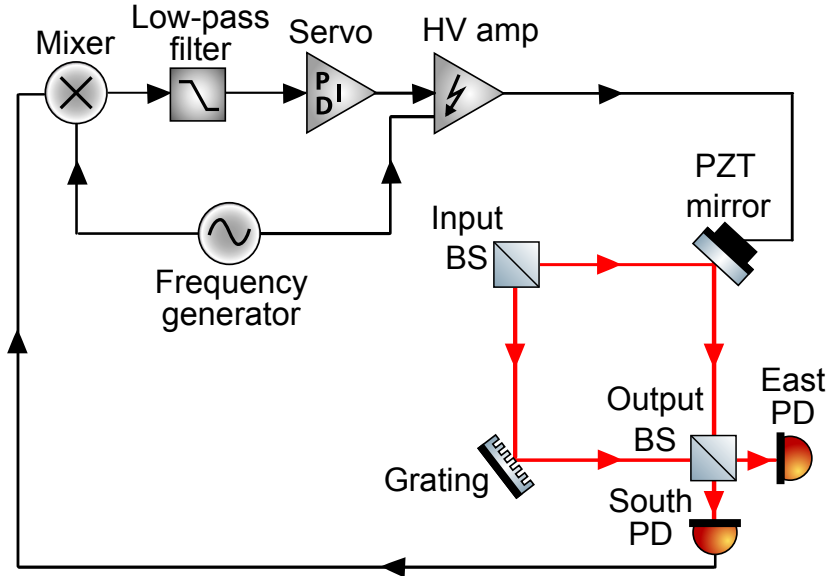


Figure 3.8.: Feedback control system used for locking the interferometer arms to the dark fringe at the south photodetector (PD). The oscillator is replaced by a frequency generator, and the inclusion of a low-pass filter enables low-frequency modulation of the piezoelectric transducer (PZT).

Low-frequency modulation is achieved by using a frequency generator instead of an oscillator to inject a modulation signal to a mixer (designed specifically for low-frequency modulation) and the PZT via the HV amp, as seen in Figure 3.8. Low-frequency modulation required a low-pass filter, which was placed between the mixer and servo (indicated in Figure 3.8), and setting the filter’s cut-off frequency to 300 Hz ensured that all high frequencies were removed.

Figure 3.9 illustrates the effects of interference between the two arms of the MZ. When the PZT is ramped back and forth continuously (green trace), the optical path length of the PZT arm increases and decreases, causing continuous constructive and destructive interference at the output BS. This gives rise to interference fringes, which is detected by the east PD as increasing and decreasing light power (pink trace). Note that due to the symmetry of the interference fringes, the signal detected by the south PD is the same as the pink trace but reversed in amplitude. The best interference contrast, or *fringe visibility*, achieved for this setup was in the region of 85-95%, and was considered to be very reasonable.

The error signal is indicated by the blue trace, and the steep zero-crossings are seen to occur when the beam intensity at the east PD is maximum (bright fringe), coinciding with the minimum intensity (dark fringe) at the south PD. The shape of the resulting error signal is typical for low-frequency modulation, as was seen in Figure B.2(b). The south port PD provided the AC signal for the mixer and the feedback signal was fed into the PZT, allowing the MZ arms to lock to the ‘dark’ port of the south PD (and hence holding the beam intensity on the bright fringe at the east PD).



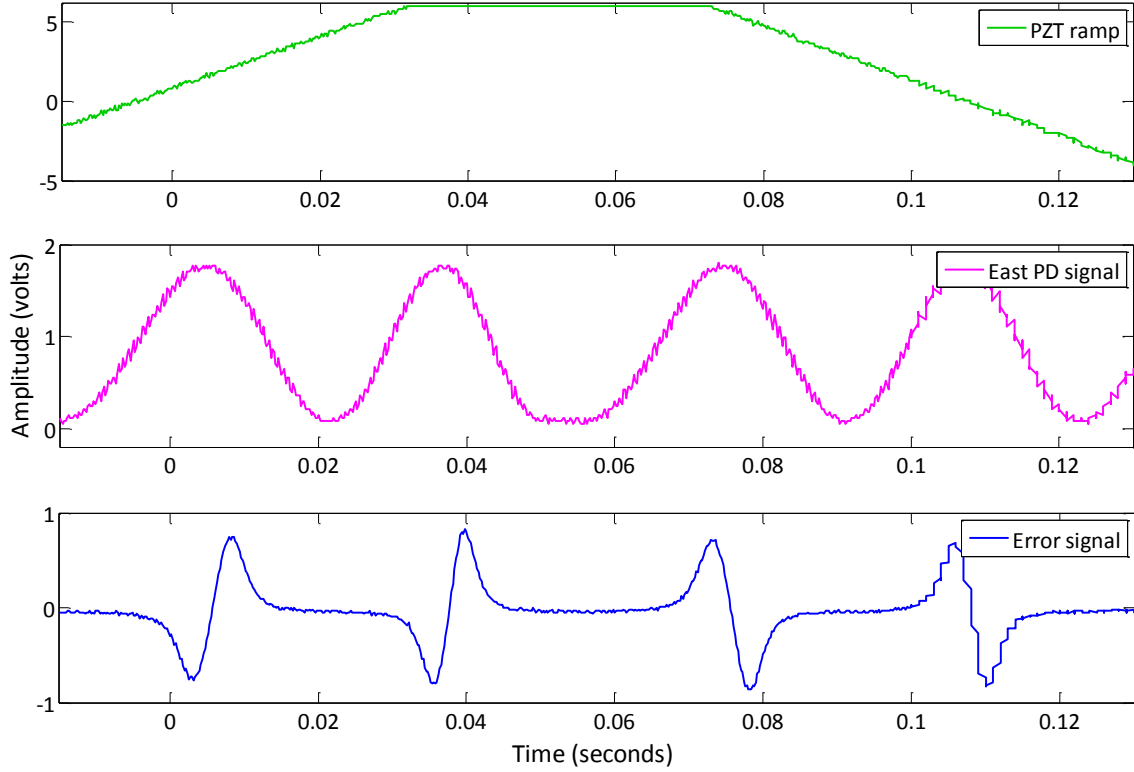


Figure 3.9.: Error signal for the Mach-Zehnder arms. Ramping the piezoelectric transducer back and forth (green) causes interference in the superimposed output beams to create bright and dark fringes at the east photodetector (pink). Low-frequency modulation creates an error signal (blue), allowing the interferometer to lock to the beam's minimum or maximum intensity.

### 3.4. Dual-mode locking technique

We aim to compare the phase between zero-order and first-order modes imprinted with a grating diffraction using the grating MZ setup. However, the absolute phase cannot be measured and so we cannot simply observe the interference fringes of zero-order and first-order modes independently and compare the phase difference. A reference point is required against which relative phase changes can be measured with any significance, but we have no common reference point, since using each order of mode would imply running two separate experiments.

Instead, we execute a method of using the same beam and continuously alternate between the two modes, whilst ensuring that the MC was locked to the relevant mode at all times. We employed a technique involving ‘dual-mode locking’.

### 3.4.1. Method of dual-mode locking

The procedure of dual-mode locking relies on the precise tuning of the MC. The resonances corresponding to  $HG_{00}$  and  $HG_{01}$  modes are both maximised to the same level using the steering mirrors. The peak of the zero-order mode occurs when the MC’s PZT is at one specific position, and the peak of the first-order mode occurs when the PZT is at another position.

These two positions equate to an amplitude difference, implying that if the PZT was supplied with a square-wave signal consisting of only two voltage levels, the PZT can be displaced back and forth continuously between two very precise positions.

A square-wave signal from an external signal generator provided these two voltages, where the minimum portion of the square-wave coinciding with the peak of one resonant mode, while the maximum part of the square-wave coincided with the peak of the other resonant mode. The CCD monitor screen displayed images of the alternating zero-order and first-order mode beam shapes, as seen in Figure 3.10.

For this setup, the amplitude for the square-wave signal was found to be in the range of  $2.1 \pm 0.1$  volts. A frequency of 10 Hz was used initially to locate the resonant peaks, and was eventually reduced to the order of a few hertz to enable locking. Figure 3.11 shows a continuously locked signal for each mode emitted from the MC (red trace) during dual-mode operation using the square-wave signal (green trace). Three perturbations are evident in the red trace - these are due to stabilisation

effects from the electronics and are discussed in the next section. Despite these fluctuations, the MC remained successfully locked at each mode.

### 3.4.2. Dual-mode fringe pattern

Once a stable dual-mode beam has been established and locked using the MC, the beam proceeds through the main MZ interferometer. The switching between the zero-order and first-order modes can be observed clearly throughout the setup with a simple infra-red laser viewing card. When the PZT in the arm of the MZ is ramped, interference at the output BS generates fringes as before, and the continuity of the fringe pattern during mode-switching can be observed. The effect is illustrated in Figure 3.12, where a fringe pattern resulting from dual-mode locking can be seen (red).

Slight fluctuations are evident in the otherwise perfectly continuous fringe pattern, coincident with the imperfections seen in the PD signal from the MC (blue), which in turn occur each time the square-wave jumps to maximum and minimum. The fluc-

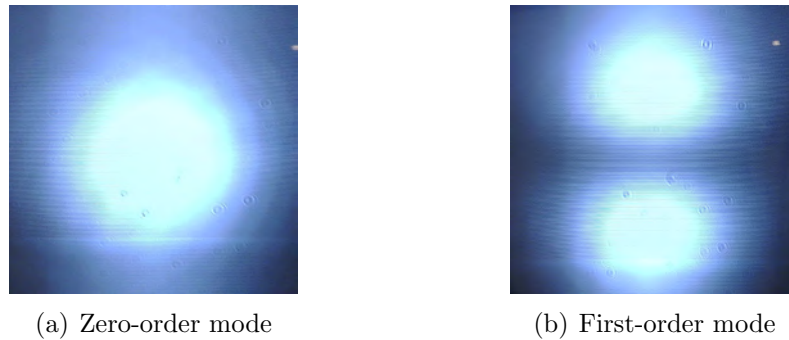


Figure 3.10.: When the piezoelectric transducer in the mode cleaner is displaced back and forth precisely at the correct amplitude, the resonating mode will alternate between zero-order and first-order modes, producing interchanging images of the beam shape.

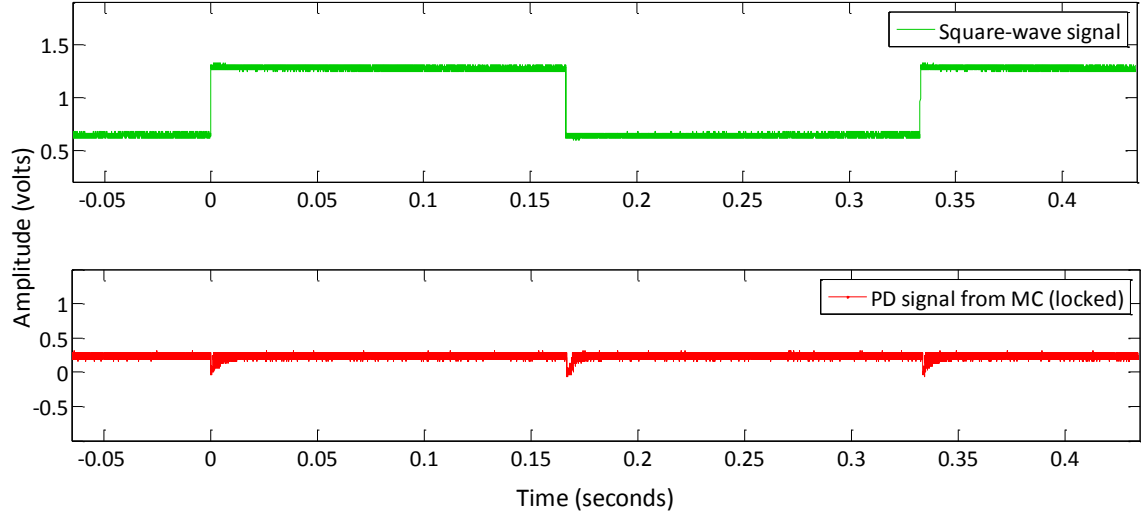


Figure 3.11.: Stable output signal from the modecleaner (MC) during locking in dual-mode. When the piezoelectric transducer in the MC shifts between zero-order and first-order modes (green), the output signal detected by the photodetector (PD) is locked to each mode alternately and remains stable (red).

tuations, signified by the vertical dashed lines, are caused by the electronic systems attempting to lock to a new mode each time. After a brief moment, the system stabilises into a locked system, and the fringe signal continues its waveform. For this reason, the square-wave signal is set to a frequency of 3Hz - a higher frequency forces the electronics to destabilise more frequently and results in very noisy fringe signals, yet if the frequency is too low, it is difficult to lock the modecleaner at both resonances<sup>5</sup>. The breaks in fringe symmetry are due to the PZT in the MZ changing direction during ramping (peaks and troughs of the triangular wave), indicated by the vertical dotted lines.

<sup>5</sup>The MC is difficult to lock using a low-frequency square-wave signal because the longer the time period at maximum or minimum level, the more round-trip distance inside the MC varies, causing the cavity to drift in and out of resonance.

### 3.5. Experimental results

If a difference in phase existed between zero-order and first-order modes, a definite phase shift would be observed in the fringe waveform each time the mode changed

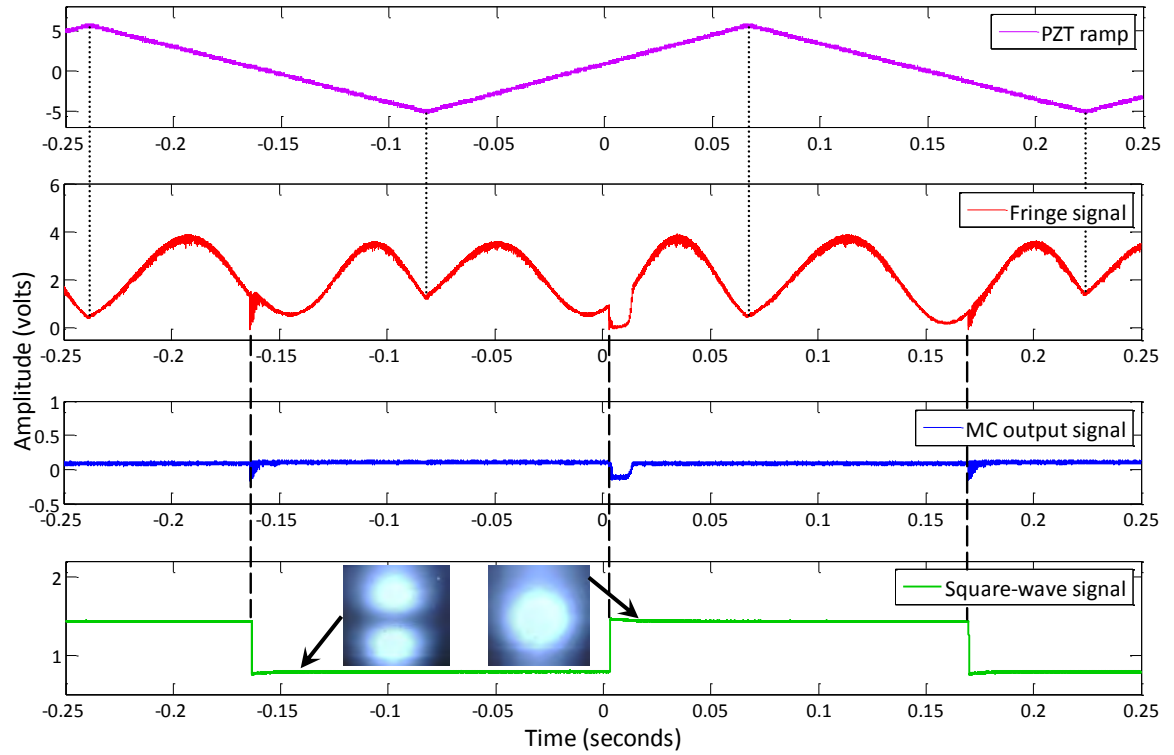


Figure 3.12.: Fringe pattern resulting from dual-mode locking. From top to bottom: piezoelectric transducer (PZT) ramp for the Mach-Zehnder arm (purple); interference fringe signal detected by the east photodetector (PD) (red); locked output signal in dual-mode from the modecleaner (MC) PD (blue); 3 Hz square-wave signal applied to the PZT in the MC (green). The maximum and minimum part of the square-wave locks to zero-order and first-order mode resonances, respectively. Note that the slight fluctuations present in both the fringe signal and the output of the MC are due to the stabilisation effects of the electronics when attempting to lock each time to a new mode.

(i.e. at the precise point when the square-wave signal jumped to maximum or minimum). However, the fringe signal (red trace) in Figure 3.12 reveals a continuous and unbroken waveform during mode-switching. Apart from the perturbations in the fringe signal which are due to the stabilisation effects from the electronics, there appears to be no obvious deviation from the general wave pattern. This result implies that, within the measurement accuracy, there is no difference in phase between zero-order and first-order modes after grating diffraction, and thereby confirming that the phase of a diffracted beam is, in fact, independent of the beam shape (or mode).

In the next chapter, we introduce a rigorous simulation tool and continue to verify mode independency in diffracted beams. In addition, a rather more thorough investigation is carried out, comparing the effects of a diffracted beam when displaced geometrically and through modal decomposition.

## Chapter 4.

# TIME-DOMAIN SIMULATION FOR GRATING DIFFRACTION

We have established that the analytical framework developed in Chapter 2 does not contain the intrinsic phase factor associated with grating-related phase changes over  $2\pi$  radians, which is otherwise present in a geometric planewave approach. We have verified that the method of modal decomposition is an accurate representation for small beam displacements. In Chapter 3 we demonstrated using a table-top experiment that the phase of a diffracted beam is independent of the beam mode. Such experimental setups are unfortunately limited to some extent in terms of precision, and a further improvement in accuracy is too costly and time-consuming. Instead, we look to alternative methods in order to study the phase behaviour of different modes after diffraction by a grating in greater detail. A flexible solution is the use of simulation tools - they allow the user to adapt any setup to suit their requirements, and various parameters can be manipulated quickly, easily and in a cost-effective manner.

We introduce an alternative notation to describe various orders of modes in terms of transverse electromagnetic, or  $\text{TEM}_{nm}$ , waves. The indices  $n$  and  $m$  refer to the node number, and so  $\text{TEM}_{00}$  and  $\text{TEM}_{10}$  correspond to zero-order modes and first-order modes respectively.

In this chapter, we aim to simulate a diffraction grating through which beams of different orders of mode are propagated, and attempt to study the phase changes created when the beam or grating is displaced. The motivation behind this is to understand why phase shifts of  $2\pi$  radians are absent in the Gaussian-based analytical model. The main objective is to observe and compare the phase changes in the 1st diffraction order in two different scenarios: (a) during a geometric beam (or grating) displacement using a  $\text{TEM}_{00}$  beam (see Section 4.3.1), and (b) during a modal decomposition, achieved by adding a  $\text{TEM}_{10}$  beam to a  $\text{TEM}_{00}$  beam and thereby replicating a beam displacement (see Section 4.4). The outcome will verify how accurately the modal decomposition approximation describes phase changes (in the 1st diffraction order) in comparison to the phase change from actual beam or grating displacements in a geometric sense.

Section 4.1 introduces the simulation tool, adapted to emulate a propagating Gaussian beam after grating diffraction. Since the simulation parameters can easily be adjusted, the phase of the diffracted beams can be measured under various conditions.

Section 4.2 provides the key parameters which define the simulation space. Considerations regarding the optical layout are also acknowledged, notably the positioning of the beam waists and reference planes for phase measurements.

In Section 4.3, we essentially test the simulation tool by propagating and diffracting a  $\text{TEM}_{00}$  mode beam during beam/grating displacement. We determine whether



the resulting phase in the 1st diffractive order exhibits a periodic change in phase of  $2\pi$  radians. This would also corroborate with the findings in [76]. The method is repeated using a  $\text{TEM}_{10}$  mode beam during grating displacement, and phase measurements are obtained for each diffraction order at both intensity peaks. Again, we resolve for signs of a periodic change in phase of  $2\pi$  radians in the 1st diffractive order.

After studying the modes independently, Section 4.4 explores the effects of combining a  $\text{TEM}_{00}$  beam and  $\text{TEM}_{10}$  beam, and hence replicating a displaced beam/grating through modal decomposition. The aim of this section is to establish if the phase in the combined modes continues to display a change over  $2\pi$  radians, through means of an equivalent beam/grating displacement. Subsequently, we also determine whether the phase of a diffracted  $\text{TEM}_{00}$  beam and  $\text{TEM}_{10}$  beam is the same by comparing the phase of the combined beams (through modal decomposition) with that of the geometric beam/grating displacements, in support of the experimental findings in the previous chapter.

## 4.1. Introduction to the finite-difference time-domain tool

The Finite-Difference Time-Domain (FDTD) is a comprehensive analytical technique which can be utilised to create a powerful two-dimensional simulation tool to solve Maxwell's equations rigorously in the time-domain [90]. The basic principle for the FDTD tool is to solve the time-domain evolution of electric and magnetic fields over time for a given spatial domain. In the framework of this thesis, an implementation of the FDTD tool was used to investigate how diffraction grating displacements coupled into the phase of diffraction orders [91, 92].

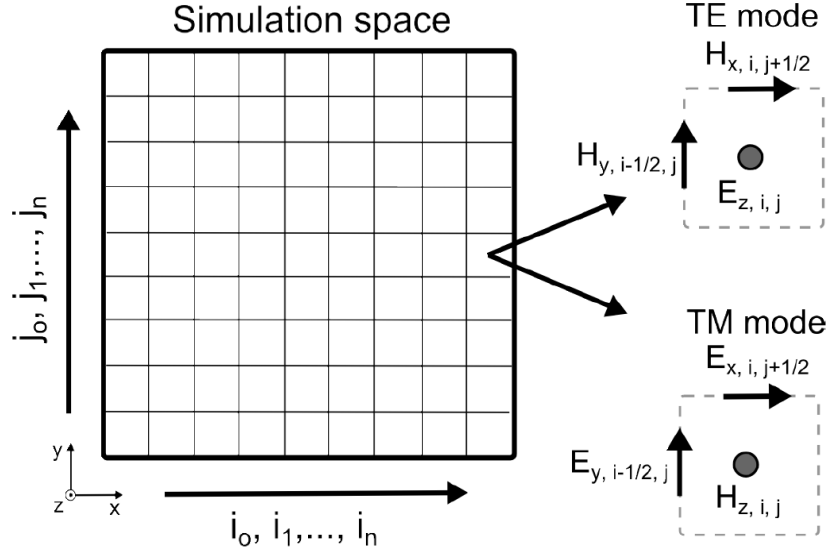


Figure 4.1.: The simulation space depicted as a grid of cells. Configurations for electric ( $\vec{E}$ ) and magnetic ( $\vec{H}$ ) field components are shown for both transverse electric (TE) and transverse magnetic (TM) polarisations.[91]

#### 4.1.1. Concept of the simulation tool

Electromagnetic (EM) fields are propagated through a simulated flat and finite spatial domain, which itself consists of discrete cells. Each cell contains information defining the properties of the space-time it occupies, including the EM field, at a specific point. Using Maxwell's equations, a set of 'update' equations are created and applied to each cell with forward iterations in time. The cells are solved numerically using the Yee algorithm [93], which separates the electric ( $\vec{E}$ ) and magnetic ( $\vec{H}$ ) field components both spatially (Spatial Staggering) and in time (Temporal Staggering). The result is a staggered grid composed of  $\vec{E}$  and  $\vec{H}$  components, seen in Figure 4.1.

The spatial differential of one cell can be calculated using the known values around it, a technique known as the Finite-Difference (FD) differential approximation. FD approximations are derived from Taylor expansions of a function containing a small

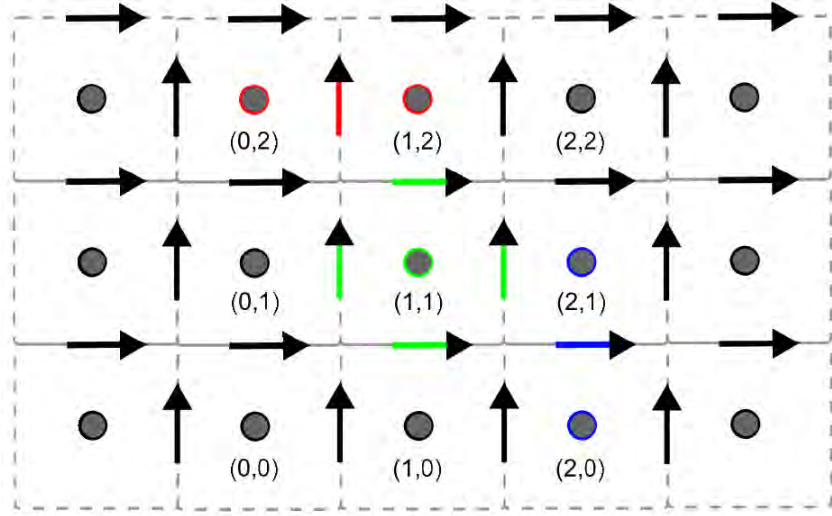


Figure 4.2.: FD differential approximation for transverse electric cells:  $H_y$  (red) is updated using the surrounding  $E_z$  values;  $E_z$  (green) is updated using the surrounding  $\vec{H}$  values;  $H_x$  (blue) is updated using the surrounding  $E_z$  values.[91]

deviation. The approximations are then applied to a set of boundary conditions to produce a list of ‘update’ equations for transverse electric (TE) and transverse magnetic (TM) polarisations. This is better visualised in Figure 4.2 (for TE cells): the change in the  $E_z$  component is dependant on the way the surrounding  $\vec{H}$  field components vary, and vice versa. The field components of each cell are then ‘updated’ at incremental timesteps, thereby specifying the optical layout one cell at a time. The update equations also contain the constants  $\epsilon$  and  $\mu$ , which are responsible for determining the properties of the diffraction grating, including the grating material and grating period.

Cell size, $\Delta$	25 nm
Simulation dimension	$1300\Delta \times 1800\Delta$ $= 32.5 \mu\text{m} \times 45 \mu\text{m}$
Wavelength, $\lambda$	1064 nm
Grating period, $d$	$60\Delta = 1500 \text{ nm}$
Beam propagation distance, $z$	$1200\Delta = 30 \mu\text{m}$
Waist size, $\omega_0$	$100\Delta = 2500 \text{ nm}$

Table 4.1.: Parameter values used to simulate beam diffraction for 0th and 1st diffraction orders.

## 4.2. Main parameters and defining the optical layout

Since the simulation is two-dimensional, it is assumed that there are no spatial changes along the  $z$ -axis. The cell size,  $\Delta$ , determines the resolution of the simulation space - the smaller the cell size, the higher the resolution. Table 4.1 outlines various parameter values, some of which are in terms of  $\Delta$ . For the purpose of this work, the simulation considers the diffraction orders  $m = 0$  and  $m = \pm 1$  only. The diffraction angle is set at  $\pm 45^\circ$  so as to minimise anisotropic dispersion. For illustration purposes, a  $\text{TEM}_{00}$  beam was simulated using the parameter values set out in Table 4.1, propagating through a diffraction grating while the grating remained fixed in one position (i.e. grating displacement  $\Delta x = 0$ ). Figure 4.3 demonstrates the resulting diffraction pattern at an instantaneous point in time. The beam travels in the direction indicated by the red arrow through a diffraction grating (grey dashed line), resulting in 0th and 1st diffraction orders.

After grating diffraction, each diffracted beam is propagated along its own respective  $z$ -axis for a specified distance before encountering reference planes, as depicted in Figure 4.3. These reference planes are transverse to the direction of beam propagation, each of which are infinite in length along the  $x$  and  $y$ -directions within the

simulation space. Probes are positioned along the reference planes to measure the amplitude of the beam at the position  $z$ . The reference plane is placed at the waist of the 0th diffraction order beam so as to avoid additional effects caused by the Gouy phase. This is due to the fact that the Gouy phase is dependent on the beam mode, and the waist position of a Gaussian beam is unique because the Gouy phase is always zero for all beam modes. By positioning the reference plane at the beam waist for a given diffraction order, we can compare the change in phase of a  $\text{TEM}_{00}$  with a  $\text{TEM}_{10}$  mode beam during grating displacement without having to consider extra Gouy phase effects for the different modes. The reference planes of the 1st diffraction orders are then placed the same optical distance away from the grating. Note that the beam propagation distance in Table 4.1 refers to the distance between the grating and the reference plane in the 0th diffraction order.

For each diffraction order, the absolute phase of the passing beam is measured by a probe which lies along the reference planes (solid pink lines). In the case of a  $\text{TEM}_{00}$  mode, the probe sits at the centre of each reference line (i.e. on the optical axis of the beam). It should be noted that the reference planes are located away from the grating to avoid any near-field interference effects which may occur at the grating. For measurements involving grating displacements, the grating is translated in small steps and the probes record the phase at each grating position (Section 4.3 provides more details). Note that at each grating position, the simulation is run for some time to allow for better averaging (typically 8 hours).

According to Figure 4.3, the reference plane for the 0th order is clearly situated at the waist. However, a closer inspection of the 1st diffraction orders reveals that the positions of the reference planes and waists do not coincide - the waist positions are situated much closer to the grating, as indicated in Figure 4.3. This phenomena is examined in further detail below.

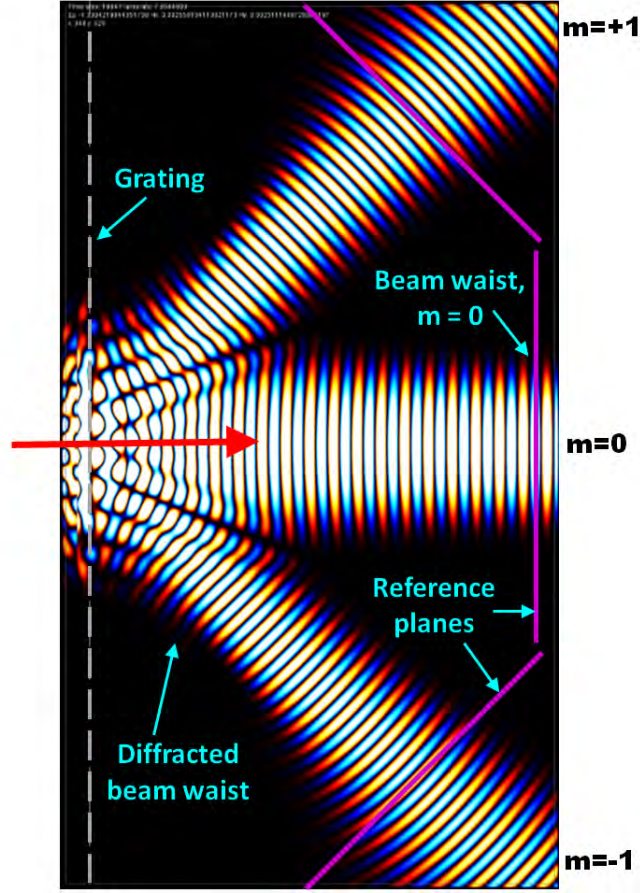


Figure 4.3.: A simulation snapshot view during the propagation of a  $\text{TEM}_{00}$  beam resulting in a diffraction pattern, without grating displacement ( $\Delta x = 0$ ). The beam propagates through the diffraction grating (grey dashed line). Probes lie in the centre of the reference planes (visible as pink lines) and are used to measure the phase in the  $m = 0$  and  $m = \pm 1$  diffraction orders. Notice that the waist position of the 1st diffraction orders are not co-located with the reference planes.

#### 4.2.1. Waist position discrepancy

The effect of the differing waist positions between the 0th and 1st diffraction orders can be explained using simple trigonometry, illustrated in Figure 4.4. The size of the beam spot,  $2\omega$ , for the 0th order beam is perpendicular to the optical axis ( $z$ -axis), but this length becomes the diagonal (or the hypotenuse) of the 1st order diffracted beam, where  $2\omega' = 2\omega\sqrt{2}$ . Not only does this introduce a reduction in the

waist size of the diffracted beam (and hence a higher divergence angle), but its waist position is forced closer to the grating. It could be argued that the reference plane could simply be moved closer to the grating in order to match the waist position. Although convenient, it is not ideal - as mentioned previously, the light in close proximity to the grating suffers near-field interference effects, clearly observed in Figure 4.3. Instead, the waist position of the diffracted beams are moved further away from the grating, thereby ensuring that the coinciding reference planes are unaffected by near-field effects. This, however, introduces another complication: without knowing the true waist size or waist position of the diffracted beam, we have no clear description of the beam parameters, making the task of setting the reference plane at the required waist position extremely difficult.

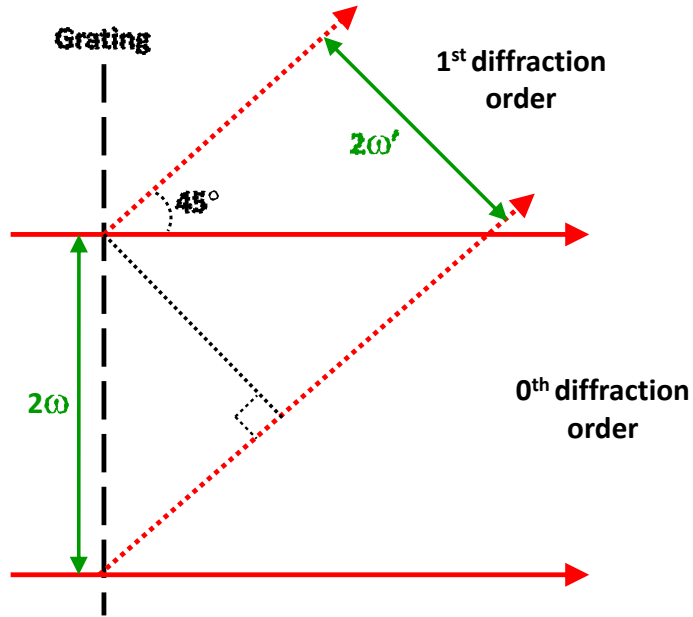


Figure 4.4.: Waist size discrepancy due to diffraction. The beam spot size,  $2\omega'$ , of the 1st order diffracted beam is not the same as the 0th order beam spot size,  $2\omega$ .

### The sagitta parameter

It is, however, possible to derive expressions for the waist parameters using the *sagitta* parameter, as seen in Figure 4.5. The beam radius,  $\omega$ , and the radius of curvature,  $R_C$ , for the 0th order beam at the grating (position  $z$ ) is proportional to its sagitta,  $s$ , which itself is the same value for the 1st order beam. For the diffracted beam,  $s$  and  $\omega'$  gives the radius of curvature,  $R'_C$ , at the grating. A thorough computation is presented in Appendix D, which ultimately results in the following expressions for the distance of the the waist position from the grating,  $z'$ , and the waist size,  $\omega'_0$ , of the diffracted beam:

$$z' = \frac{(\omega'^2\pi)^2 R'_C}{R_C'^2\lambda^2 + (\omega'^2\pi)^2}, \quad (4.1)$$

and

$$\omega'_0 = \frac{\omega'\lambda R'_C}{\left(R_C'^2\lambda^2 + (\omega'^2\pi)^2\right)^{\frac{1}{2}}} = \frac{\lambda}{\omega'\pi} \sqrt{R'_C z'}. \quad (4.2)$$

Taking into account the waist position discrepancy, the simulation parameters were adjusted accordingly. The simulation space was increased so that the waist in the 0th diffraction order was situated much further away from the grating, allowing the waist (and therefore the reference planes) in the 1st diffraction order to be ideally located further away from the grating, away from any near-field effects. This is displayed in Figure 4.6, whereby the waist positions and reference planes in the 1st diffraction orders are clearly situated away from the grating.



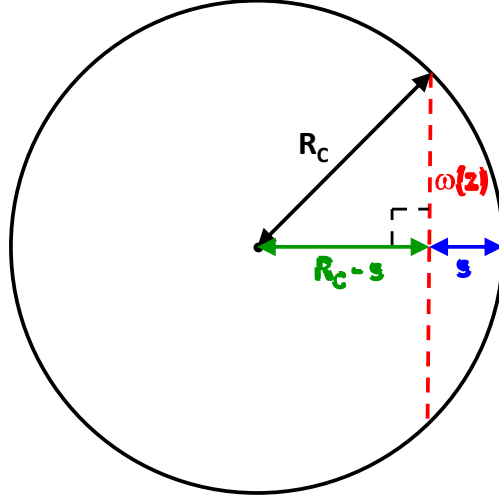


Figure 4.5.: The sagitta,  $s$ , of a beam at point  $z$  is related to the beam spot radius  $\omega$  and the radius of curvature  $R_C$  at  $z$ . The sagitta has the same magnitude for both 0th and 1st diffraction orders.

### 4.3. Phase change for grating/beam displacement

In this section, we propagate a Gaussian beam through a diffraction grating and measure the phase in each diffraction order as the grating is displaced and observe the change in phase. The aim of this task is to substantiate the phase changes associated with the intrinsic phase factor, and simultaneously ascertain that the simulation tool does indeed produce the correct results.

We recall that the expression describing the change in phase due to a geometric grating/beam displacement was given in Section 1.5.3 as

$$\Delta\theta = -\Delta x' \frac{2\pi m}{d}. \quad (4.3)$$

When a grating or beam is displaced by an amount  $\Delta x = d$ , then according to Equation (4.3), a diffracted beam will undergo a total phase shift of  $2\pi m$  radians, with a dependency on the diffraction order  $m$ . This phase change is referred to

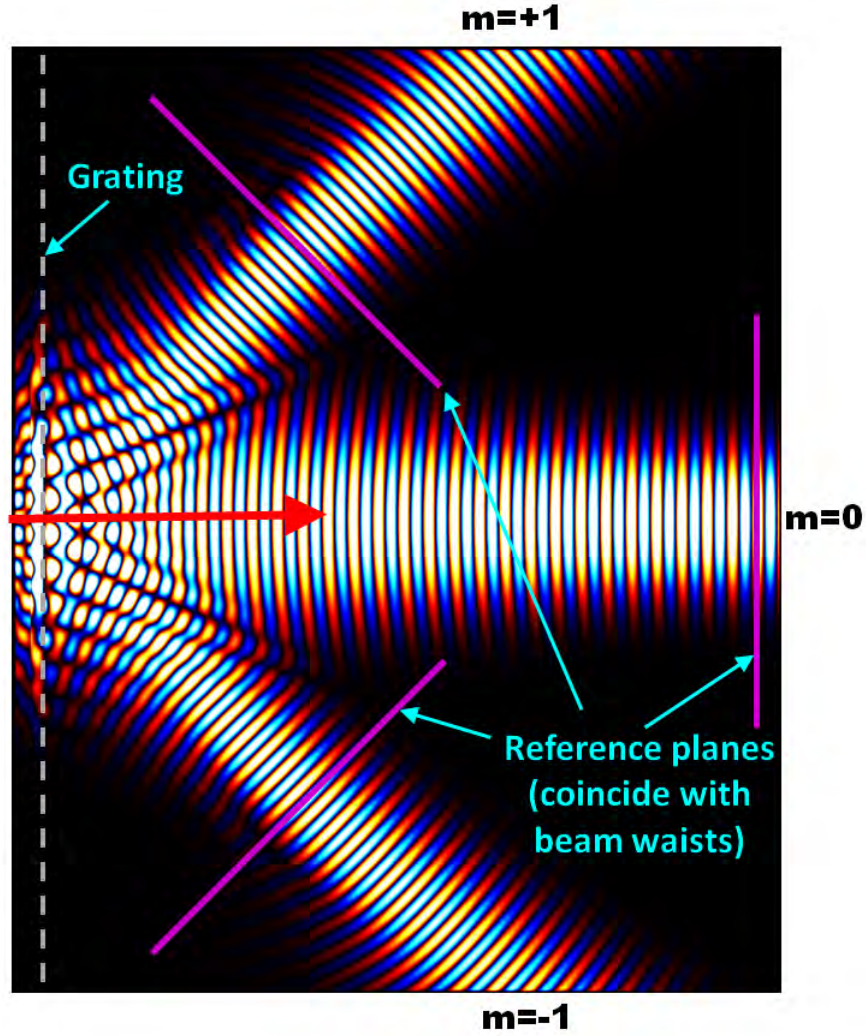


Figure 4.6.: Simulated 0th and 1st order diffraction pattern of a  $\text{TEM}_{00}$  beam, correcting for the waist position in the 1st diffraction orders. The reference planes for the  $m = \pm 1$  diffraction orders now coincide with the waist positions.

as the intrinsic phase factor. We implemented this grating movement (along the vertical direction) into the FDTD tool, incrementing the distance  $d$  into 40 steps, and placing probes in the 0th and 1st diffraction orders. The model was run 40 times, each time displacing the grating by a distance of  $d/40$  and obtaining phase information from each probe. We expect to see a linear relationship between the

grating displacement and measured phase for  $m = \pm 1$ , and a constant phase for  $m = 0$ .

### 4.3.1. Grating displacement

#### TEM<sub>00</sub> beam

A simple TEM<sub>00</sub> beam is subjected to grating diffraction, as shown in Figure 4.6, and the resulting phase measured during grating displacement can be seen in Figure 4.7 for the zeroth and first diffraction orders for a TEM<sub>00</sub> beam.

In the case of  $m = 0$  (green trace), the phase remains constant, which is consistent with Equation (4.3). For  $m = +1$  (red trace) and  $m = -1$  (blue trace), the phase changes linearly by  $2\pi$  radians over a displacement of  $1.5\ \mu\text{m}$ , or one grating period  $d$ , as predicted.

It is also interesting to note that the 1st diffraction orders display slopes with opposite signs: the  $m = +1$  beam shows a gradual decrease in phase (negative), whereas the  $m = -1$  beam gradually increases in phase (positive). This is simply due to the fact that as the grating is translated in one direction, the optical path length of one of the diffracted beams decrease and for the other diffracted beam the optical path length increase. This in turn requires the phase change to also increase or decrease, leading to a negative and positive slope.

It is important to remember that we are interested in the *change* in phase, and not the *absolute* phase. The absolute phase can be considered as an offset and is affected by factors such as the specific location of the probe along the optical axis. The position of the traces for  $m = +1$  and  $m = -1$  relative to each other along the

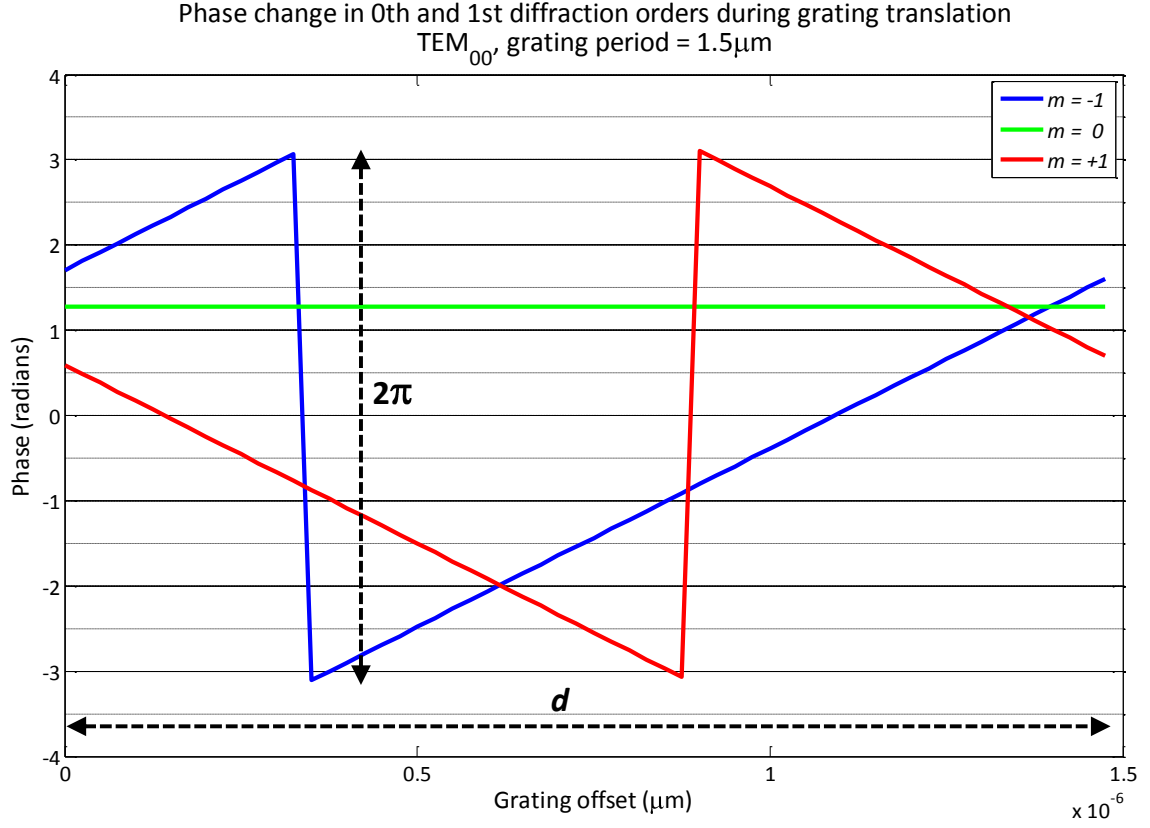


Figure 4.7.: Phase change for the 0th and 1st diffraction orders during grating displacement for a  $\text{TEM}_{00}$  beam. No phase change is present for  $m = 0$  beam (green), while the diffracted beams  $m = +1$  (red) and  $m = -1$  (blue) show a total change in phase of  $2\pi$  radians over a displacement of  $1.5\mu\text{m}$  (one grating period,  $d$ ).

$x$ -axis is irrelevant, but the shape of each trace is significant.

### **$\text{TEM}_{10}$ beam**

We now repeat the process described in the previous section, this time using a  $\text{TEM}_{10}$  beam. Figure 4.8 depicts a simulation snapshot during the propagation of a  $\text{TEM}_{10}$  beam passing through a diffraction grating, generating diffraction orders of  $m = 0, \pm 1$ . Each  $\text{TEM}_{10}$  beam consist of two intensity spots, or lobes, which are always 180 degrees out of phase. Each reference plane therefore consists of a pair of

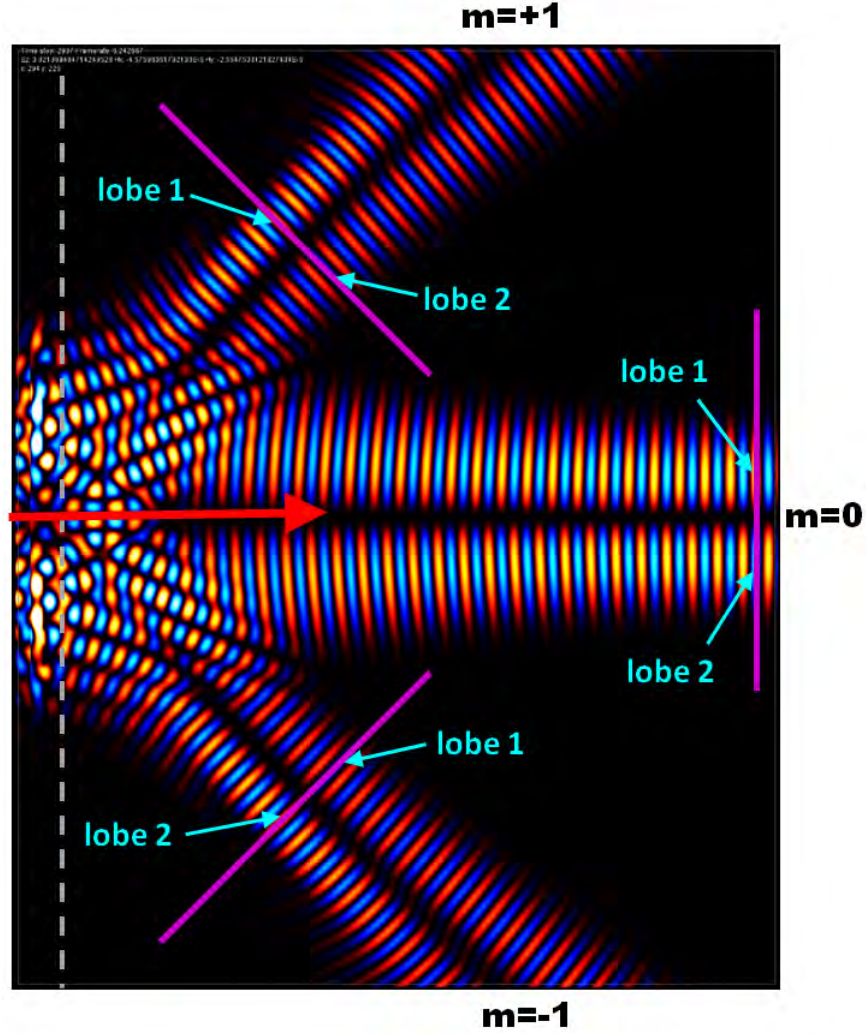


Figure 4.8.: Simulated 0th and 1st order diffraction pattern of a  $\text{TEM}_{10}$  beam. Each diffraction order now contains two intensity peaks; to account for this, the phase is measured at two points along each reference plane, lobes 1 and 2.

probes, marked lobe 1 and lobe 2, to measure the phase.

The phase measurements for each lobe are displayed in Figure 4.9. The 0th diffraction orders are shown in green: solid line for lobe 1 and dashed line for lobe 2. In addition to being flat, both traces are  $\pi$  radians out of phase, as expected. The

$m = -1$  diffraction order is indicated in blue: the solid blue line is lobe 1 and the dashed blue line is lobe 2. Lobe 1 is  $\pi$  radians out of phase with lobe 2, as should be the case for a first-order Gaussian beam. Both lines also reveal the same profile as seen in Figure 4.7 for  $m = -1$  (also in blue): the phase is seen to change linearly by  $2\pi$  radians over one grating period, with a gradual increase in phase. For the  $m = +1$  diffraction order, lobe 1 is represented by the solid red line and lobe 2 is the dashed red line. Once again, both lobes are seen to be  $\pi$  radians out of phase with each other, and the phase exhibits a linear change by  $2\pi$  radians over a grating period, with the phase decreasing gradually, and this is consistent with  $m = +1$  in Figure 4.7 (red trace).

In the case of a diffracted  $\text{TEM}_{10}$  beam, the phase measurements exhibit the correct profile with the phase shift of  $2\pi$  radians. We can therefore conclude that it is appropriate to combine a  $\text{TEM}_{10}$  mode with a  $\text{TEM}_{00}$  mode for the purpose of modal decomposition (see Section 4.4), since each mode displays the correct phase behaviour.

### 4.3.2. Beam displacement

In order to substantiate that a grating displacement and beam displacement are identical situations, the simulations described in Section 4.3.1 were repeated but applying incremental displacements to the incident beam (also along the vertical axis, parallel to the grating in Figure 4.6) instead of shifting the grating. For consistency in phase measurements, the reference planes were also required to be displaced simultaneously in the vertical direction.

The resulting phase in each diffraction order for beam displacement was found to be exactly the same as that generated by grating displacement, for each  $\text{TEM}_{00}$  and

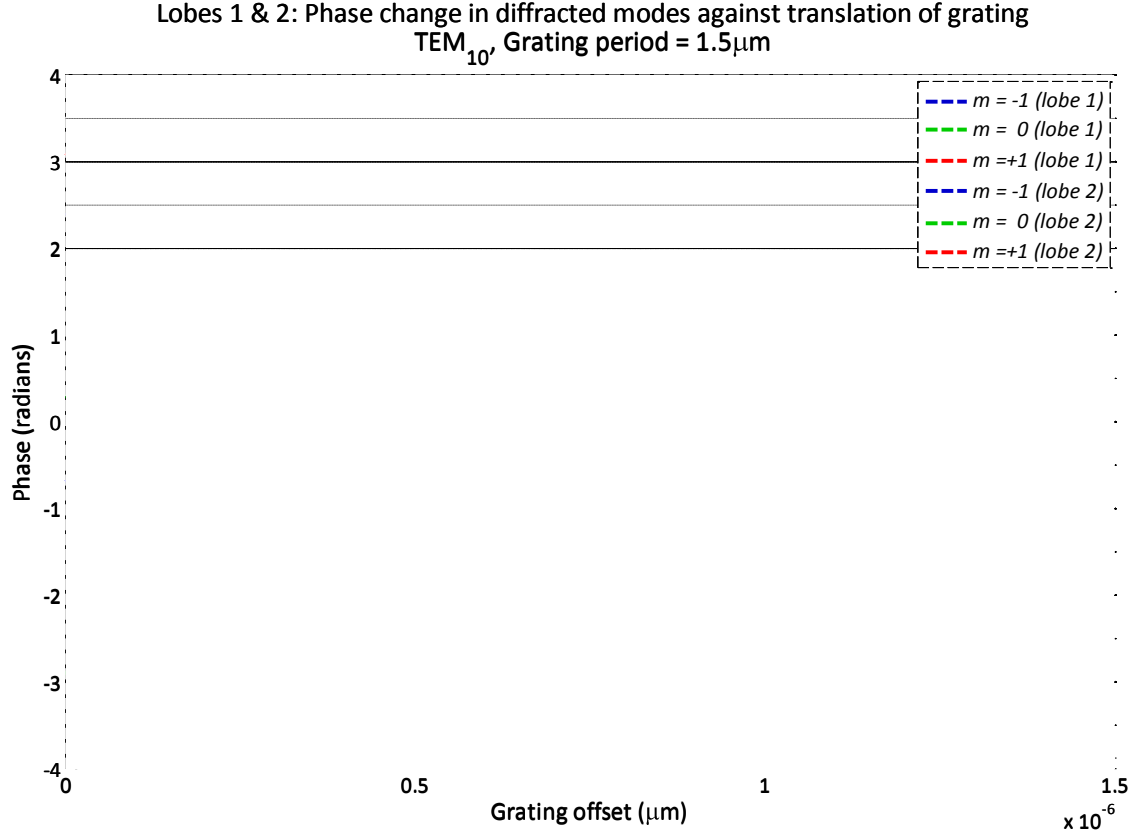


Figure 4.9.: Phase change for the 0th and 1st diffraction orders during grating displacement for a  $\text{TEM}_{10}$  beam.

$\text{TEM}_{10}$  beam. In addition to proving the equivalency between beam and grating displacement, this also assured that the simulation tool was producing legitimate phase results. Confident with the simulation output, we look to the next task of investigating the phase output of a modally decomposed beam.

## 4.4. Modal decomposition

In the previous section, we showed that the diffracted  $\text{TEM}_{00}$  and  $\text{TEM}_{10}$  beams displayed phase profiles consistent with the intrinsic phase factor, in the case of either grating or beam displacements. Keeping the grating stationary, we can now use

the concept of modal decomposition by combining zero-order and first-order modes to reproduce beam displacements and examine the phase effects. The incremental beam displacements are replicated by an incremental addition of the *amplitude* of the  $\text{TEM}_{10}$  mode to the  $\text{TEM}_{00}$  mode (as described in Equation (2.22)). The addition of the two modes can be performed within the simulation tool in two ways: firstly by combining the modes before propagation, and secondly by propagating each mode separately before combining the modes, outlined as follows.

#### 4.4.1. Mode combination

##### **Combine the $\text{TEM}_{00}$ and $\text{TEM}_{10}$ modes before propagation**

This method involves adding the  $\text{TEM}_{10}$  mode to the  $\text{TEM}_{00}$  mode at the beginning of the simulation. For each effective beam displacement, the  $\text{TEM}_{10}$  input is incrementally increased in amplitude. For each incremental increase, the corresponding  $\text{TEM}_{10}$  mode is combined with the  $\text{TEM}_{00}$  mode and then propagated through the diffraction grating, and the phase is measured at the reference planes for each increment.

##### **Propagate the $\text{TEM}_{00}$ and $\text{TEM}_{10}$ modes independently before combining**

In this case, each  $\text{TEM}_{00}$  and  $\text{TEM}_{10}$  mode is propagated in full through the diffraction grating and then combined. The amplitude of the  $\text{TEM}_{10}$  mode is increased in small increments and propagated each time, before coupling with the fully propagated  $\text{TEM}_{00}$  mode. For every increase in amplitude, the phase of the summed propagation is measured at the reference planes (where maximum intensity occurs in the resulting diffracted beams).



Both of the modal decomposition methods described above were simulated for a displacement equivalent to  $h/\omega_0 = 0.3$ . The diffraction patterns produced were identical, as illustrated by the left and centre images in Figure 4.10. The absolute error in phase between the two diffraction patterns can be seen in the right-hand image in Figure 4.10; the difference is almost zero, and indicates an equal phase pattern between the two modal techniques. This result validates the superposition principle for linear optics, and since both modal decomposition techniques are identical, either method can be applied. All modal decomposition computations described from now on will use the second method.

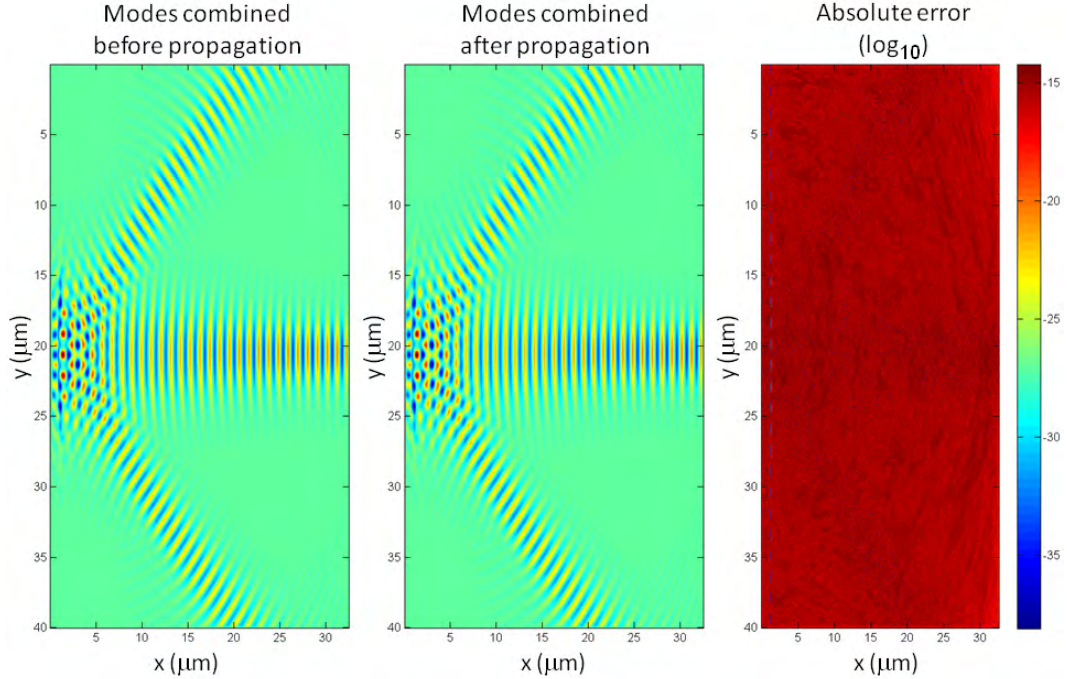


Figure 4.10.: Diffraction pattern of a modally decomposed beam for a displacement equivalent to  $h/\omega_0 = 0.3$ . *Left*:  $\text{TEM}_{00}$  and  $\text{TEM}_{10}$  modes combined and then propagated through the diffraction grating. *Centre*: Each mode propagated separately and then merged. *Right*: Absolute error in phase between the two methods.

#### 4.4.2. Translation of reference planes

Since the addition of a higher-order mode to a zero-order mode induces an effective beam displacement, it follows that the reference planes must also be displaced in the same direction as the effective beam displacement (as was the case in Section 4.3.2), ensuring that the geometry of the layout with respect to the grating is consistent. This is a requirement that must be met by *each* of the  $\text{TEM}_{00}$  and  $\text{TEM}_{10}$  mode propagations before they are combined.

To demonstrate the importance of translating the reference planes for both mode propagations, Figure 4.11 displays the phase change resulting from a modal decomposition where the reference planes for only the  $\text{TEM}_{10}$  mode is shifted, and those for the  $\text{TEM}_{00}$  remain fixed in position. The black dashed lines represent the ideal phase change according to the intrinsic phase factor for an analytical planewave model, and the  $m = 0$  diffraction order (green trace) maintains a flat line. However, the diffraction orders for  $m = +1$  (red trace) and  $m = -1$  (blue trace) do not follow the predicted dashed lines, instead displaying phase changes close to zero.

When the simulation is performed while shifting the reference planes for both the  $\text{TEM}_{00}$  and  $\text{TEM}_{10}$  mode propagations equally and in sync with the effective beam displacement  $h$ , we obtain the phase changes shown in Figure 4.12. As well as the anticipated flat green trace for the  $m = 0$  diffraction order, the phase profiles for the  $m = +1$  and  $m = -1$  diffraction orders (red and blue traces, respectively) are evidently perfectly aligned with the black dashed lines predicted by the intrinsic phase factor. It is therefore imperative to shift the reference planes for both modes during a modal decomposition in order to obtain the correct phase changes. In addition, the accuracy of the simulation tool is verified by the results presented in Figure 4.12.

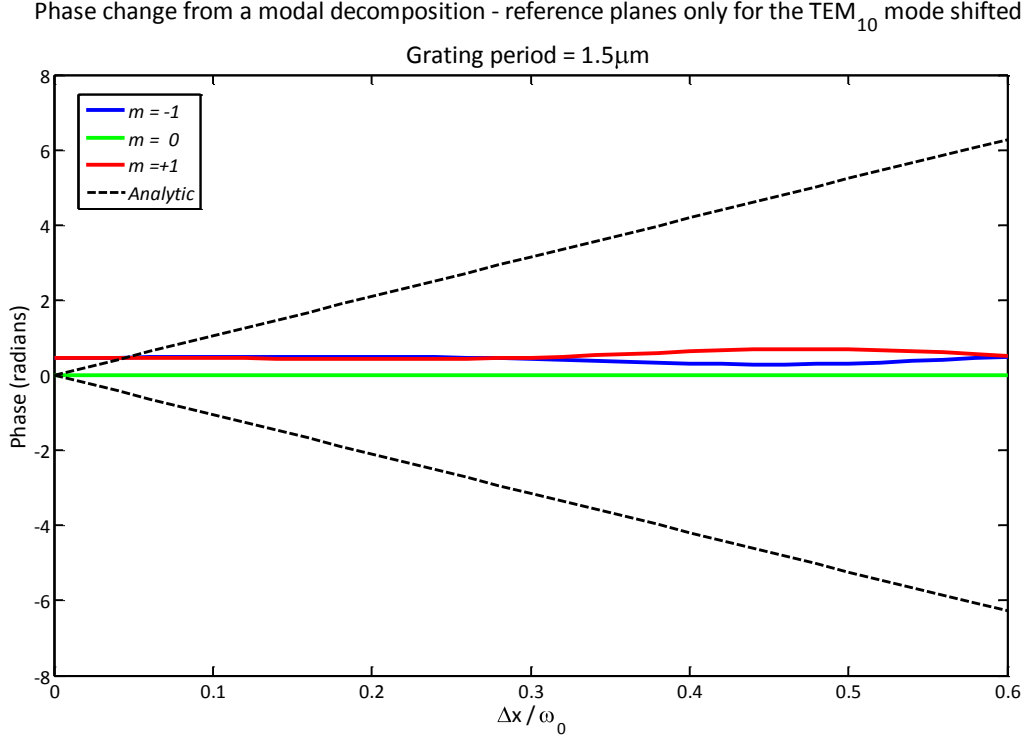


Figure 4.11.: Phase change due to modal decomposition with moving reference planes for one mode. Only the reference planes for the  $\text{TEM}_{10}$  mode propagation are translated simultaneously with the effective beam displacement, while those for the  $\text{TEM}_{00}$  mode remain stationary. The black dashed lines denote the phase change due to the intrinsic phase factor for  $m = \pm 1$ .

According to Figure 4.12, the beam is displaced by a total distance of one grating period  $d$ , which is equivalent to  $\Delta x / \omega_0 = 0.6$  (where  $\Delta x = 1.5\mu\text{m}$  and  $\omega_0 = 2.5\mu\text{m}$ ). Note that by this point, the  $m = \pm 1$  diffraction orders have undergone a total phase change of  $2\pi$  radians, with a positive slope for  $m = -1$  and a negative slope for  $m = +1$ . This periodic phase change is in *exact agreement* with the intrinsic phase changes for an analytical planewave model (and as seen in Figure 4.7).

Now that we have established the phase behaviour for geometrical beam/grating displacements and modal decomposition, we can now make a direct comparison in the following section.

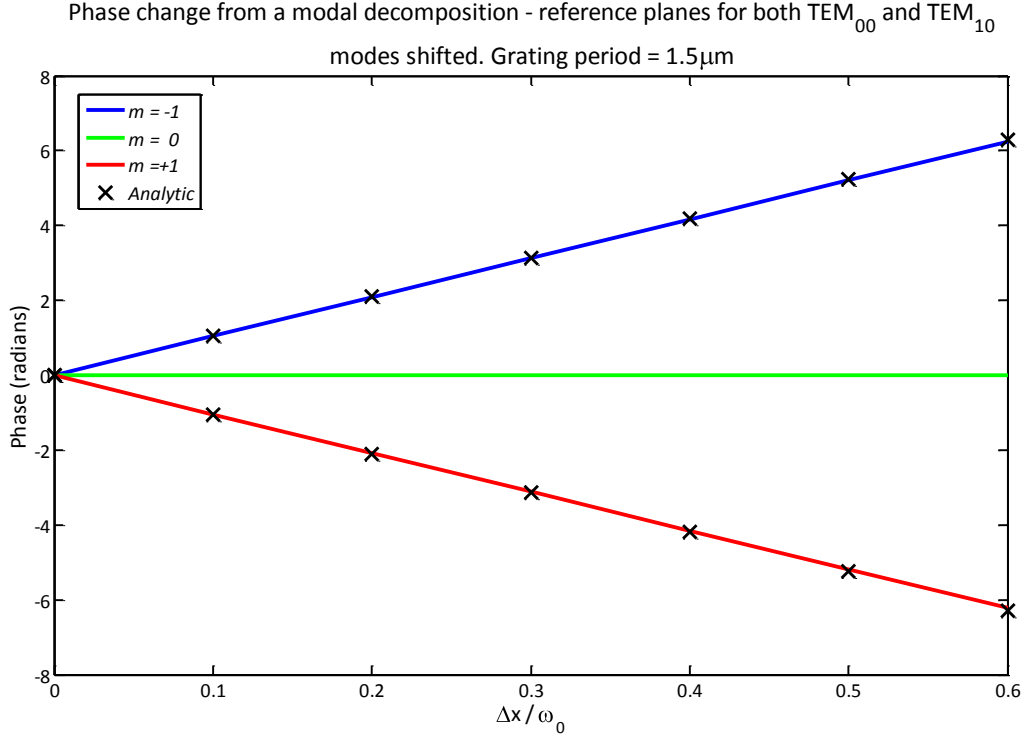


Figure 4.12.: Phase change due to modal decomposition with moving reference planes in both modes. The reference planes for both the  $TEM_{00}$  and  $TEM_{10}$  mode propagations are translated simultaneously with the equivalent beam displacement. The  $m = \pm 1$  diffraction orders (red and blue traces) follow the precise linear profile given by the analytical modal model (black dashed line with crosses)

## 4.5. Grating/beam displacement vs. modal decomposition

We investigated the phase behaviour for a geometrical grating/beam displacement (Section 4.3) and for a modal decomposition (Section 4.4) and found both instances to be in agreement with Equation (4.3). However, a direct phase comparison between the two methods would provide a definitive and clearer understanding. To recap, the two scenarios considered are as follow:

1. A geometric translation of the incident  $\text{TEM}_{00}$  beam (or grating) in the vertical direction, noting that in the case of beam displacement, the reference planes are shifted simultaneously.
2. A modal decomposition, adding a  $\text{TEM}_{10}$  mode to the  $\text{TEM}_{00}$  mode to create an effective beam displacement in the vertical direction. This leads to two possibilities: (a) a corresponding shift of the reference planes vertically, and (b) keeping the reference planes fixed in position.

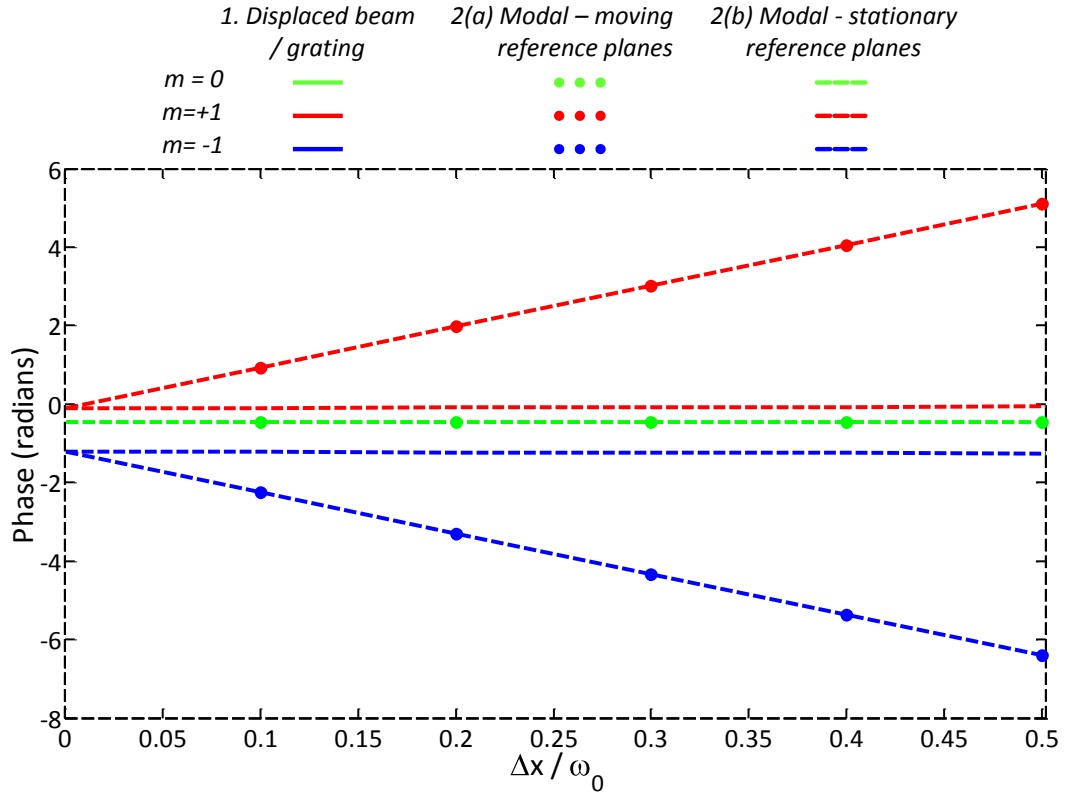


Figure 4.13.: Comparison of the change in phase of a displaced beam for various diffractive orders. Three cases are considered: a geometric beam/grating translation (solid), modal decomposition with adjusted reference planes (dotted) and modal decomposition with stationary reference planes (dashed). Note that the dashed green line is coincident with the solid green line.

The resulting phase changes in each diffraction order for the three cases outlined above in 1, 2 (a) and 2 (b) are illustrated in Figure 4.13, showing a clear distinction. The geometric beam/grating translation (case 1) is depicted by the solid lines, with the  $m = \pm 1$  diffraction orders (red and blue, respectively) exhibiting the correct linear change in phase of  $2\pi$  radians over a total displacement of  $d$ . The modal decomposition technique with moving reference planes (case 2 (a)) is identified by the dotted lines, and display exactly the same phase noise as observed in case 1. In contrast, the modal decomposition method with stationary reference planes (case 2 (b)) represented by the dashed lines exhibit zero phase change for the  $m = \pm 1$  diffraction orders.

## 4.6. Simulation results

We have established that the technique of modal decomposition into zero-order and first-order modes (with moving reference planes) describe a misaligned diffracted beam perfectly, and we interpret the identical phase profiles in Figure 4.13 as verification.

Figure 4.13 reveals that when a displaced diffracted beam is simulated, whether through a geometric translation or modal decomposition, the reference planes must also be shifted (in the same direction as the effective beam displacement) in order to measure the true phase, and this implies a change in the coordinate system. However, the modal decomposition method can be analysed in two possible ways: reference planes can either be moved or fixed.

For clarity, we refer to Figure 4.14 to demonstrate a beam displacement through modal decomposition for shifting and stationary reference planes. As in case 2 (a), a shifting of the reference plane simultaneous with the effective beam displacement

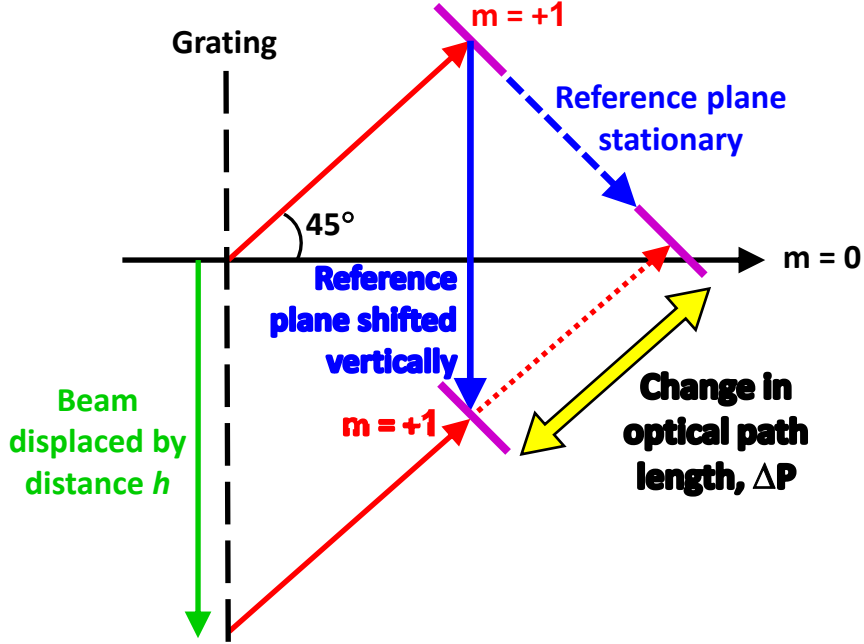


Figure 4.14.: Phase measurements resulting from modal decomposition are dependent on the movement of the reference planes (purple solid lines). A vertical shift of the reference plane (solid blue arrow) ensures that the optical path length of the beam remains constant, as specified in case 2(a). However, if the reference plane is stationary (blue dashed arrow), the optical path length of the displaced beam changes by  $\Delta P$  (red dotted arrow), thereby exactly cancelling the desired phase effect, described by case 2(b).

and in a vertical direction (indicated by the solid blue arrow) guarantees a constant optical path length of the beam, and therefore the geometry of the layout with respect to the grating remains consistent. In contrast for case 2(b), the stationary reference plane (which has an infinite length within the simulation space, depicted by the blue dashed arrow) instinctively intersects the displaced beam at a different position along the beam's optical axis. The change in the optical path length of the displaced beam, denoted as  $\Delta P$  (red dotted arrow) in Figure 4.14, acts to completely cancel the desired phase effect.

The findings from the simulations can initially be summarised as follows: in the case of modal decomposition, moving the reference planes simultaneously with effective beam displacement does indeed correspond to a phase shift in agreement with the intrinsic phase factor for a pure geometric planewave consideration. However, stationary reference planes have the effect of compensating for the phase change, and therefore resulting in a zero phase shift.

We have shown that a correct phase result can be obtained by the vertical shifting of the reference planes. But by shifting the reference planes, the user is in fact instinctively providing the extra information about the beam, such as the precise point where it interacts with the grating, which is required to provide the correct phase information for the diffracted beam.

The standard modal-based simulation tools used in the GW community for detector design and commissioning are based on a framework which have optics centred on one axis for analysing beam content and therefore rely on modal decomposition techniques to describe beam misalignments. Such modal-based simulation tools follow the case described in 2 (b), where the reference planes cannot be moved.

However, we have also shown that on the central optical axis used by these tools, any phase due to beam or grating displacements is not present. This allows for the models to be amended by explicitly adding the intrinsic phase factor as described in the planewave formalism as a feature of the optical component, i.e., the grating.



## Chapter 5.

# CONCLUSIONS

Within the scope of this work, I have validated the fundamental aspects of a modally decomposed beam using an analytical description. I developed an analytical framework which incorporated a Gaussian model for describing the phase changes due to beam misalignments through both geometric translation and modal decomposition into higher-order modes. I computed the phase terms for translated and modally decomposed beams and confirmed that they are the same. The approximation factor used to obtain the expression for the electric field of a modally decomposed beam was validated as an accurate method to describe small beam misalignments. I showed that the analytical framework for existing mode-based simulation tools lacks a full description for diffraction gratings for the beam to interact with. The absence of a grating structure means that the associated intrinsic phase factor (i.e. the periodic phase change resulting from lateral grating or beam displacement) does not exist within this analytical framework.

The purpose of the experiment was to observe a beam diffracted by an actual grating but without any lateral displacement of the beam or grating. I substantiated the

mode-independency of the phase of a beam to justify the concept of adding higher-order modes when describing misaligned beams. Using a table-top Mach-Zehnder setup with a diffraction grating placed in one of the arms, I compared the phase between zero-order and first-order beams. No phase changes were observed between the two mode-orders, and I showed for the first time that the phase of a diffracted Gaussian beam is entirely independent of the beam shape (or mode), and that the addition of higher-order modes has no effect on the overall phase of the beam.

By using a rigorous time-domain simulation tool, I was able to fully describe a grating structure and displace a diffracted beam (geometrically and through modal composition). This approach allowed for the setup to be described precisely and, provided the reference planes were set correctly, the expected phase changes in the displaced diffracted beam could be demonstrated in accordance with the intrinsic phase factor.

The research presented in this thesis confirms that in addition to the grating parameters such as angles and efficiencies, the intrinsic phase factor must also be described explicitly in order to obtain the correct phase changes for beam displacements. Analytical and numerical models which analyse beam content and are based on frameworks with the optics centred on one axis therefore require an explicit manual implementation of the intrinsic phase factor when dealing with small beam misalignments so as to acquire an accurate description of the beam phase upon interaction with diffractive elements.

## **Chapter 6.**

# **ADVANCED LIGO BOSEM DEVELOPMENT AND TESTING**

The LIGO detectors are currently undergoing a series of upgrade installations towards Advanced LIGO, with the aim of increasing sensitivity levels by a factor of ten and operating over a broader frequency bandwidth. Seismic noise limits initial LIGO at low frequencies to about 40 Hz; Advanced LIGO will push this seismic cut-off frequency down to about 10 Hz. This is achieved through a complex multiple pendulum suspension system and enhanced methods of sensing and control of the test mass position.

This chapter begins by providing a summary of the main suspension system components, with a focus on the combined sensors and actuators developed at the University of Birmingham. This is followed by a description of the various activities carried out in the framework of this thesis to support the sensor/actuator modifications. These include an evaluation of sensor flags mounted magnetically compared with Vacseal mounts (Section 6.2), burn-in and screening of the infra-red light-emitting

diodes (IRLEDs) and photodiodes (PDs) (Section 6.3) and automated testing for fully assembled devices (Section 6.4). A total of 654 BOSEMs were produced by the University of Birmingham for the Advanced LIGO detectors.

## 6.1. Suspension system

### LIGO

In initial LIGO, fused silica test masses weighing 11kg were suspended as single pendulums on steel wire slings. Actuation was applied to damp the pendulum modes (local control), and to control the test masses directly through the use of coil and magnet systems, maintaining the interferometer's correct operating position (global control) [38].

### Advanced LIGO

The Advanced LIGO suspension system is based on the GEO 600 triple pendulum design [95]. There are a number of benefits associated with multiple pendulum stages; firstly, the seismic vibration isolation of the test mass in the horizontal direction is increased. The transfer function of the pendulum falls off at each stage as  $f^{-2}$  above its pendulum resonance frequency, and by choosing resonances within the range of 0.4 Hz to 4 Hz [27], the multiple-stage pendulum can provide passive isolation above a few hertz. Secondly, any noise injected by the controllers at the suspension point or due to thermal effects are reduced because the pendulum acts as a mechanical filter, and control forces exerted on the test mass are reduced considerably [96].

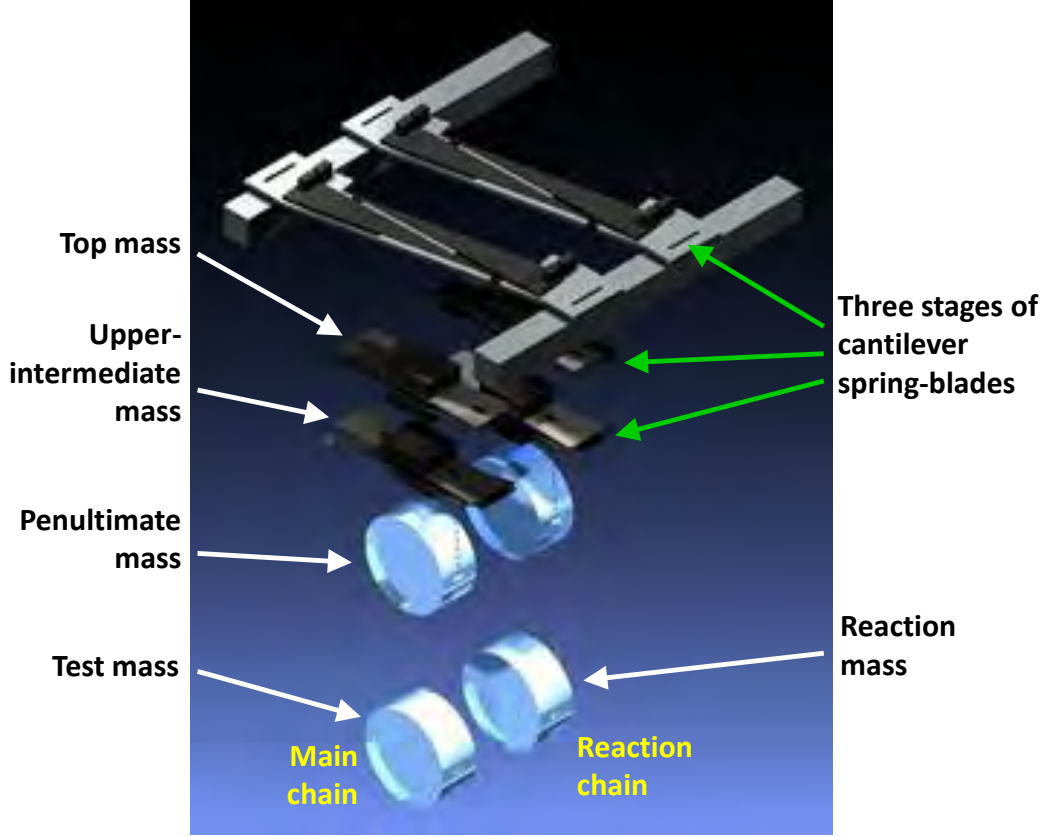


Figure 6.1.: Structure of a quadruple suspension system, displaying the main chain and reaction chain. The stages from top to bottom are: top mass, upper-intermediate mass, penultimate mass and test mass, with the first three stages suspended from cantilever spring-blades [94].

The optics within different subsystems of the Advanced LIGO interferometer will have various seismic noise suppression requirements, and so a mixture of triple and quadruple suspensions will be used. The most sensitive optics will be supported by quadruple suspensions, including the ETMs, ITMs, BS and folding mirrors. The triple suspensions will support the PRM, SRM and the three MC mirrors [34].

The configuration for a quadruple suspension can be seen in Figure 6.1. Three stages of cantilever support the top, upper-intermediate and penultimate masses (only two stages are required in the triple suspensions), with the purpose of increasing vertical vibration isolation. The top and upper-intermediate masses consist of rectangular

stainless steel plates. The test mass is formed from fused silica, weighing 40 kg. In terms of mass and size, the penultimate mass is identical to the test mass, however, the silica material of the penultimate mass is of a lower quality (as its optical properties are not relevant for the interferometric measurements). With the exception of the final stage, the masses in each stage will be suspended by steel music wire. Since the test mass is the least isolated from the last pendulum stage, it will be suspended from the penultimate mass by high-quality fused silica fibres which have a low mechanical loss [27].

The quadruple suspension system is actually composed of two parallel pendulum chains 5 mm apart: the *main chain*, which suspends the test mass, and the *reaction chain*, to support the reaction mass, as indicated in Figure 6.1. The mass and dimensions of the reaction chain are almost identical to the main chain, and its purpose is to apply actuation to the main chain from a quiet platform.

Actuation forces can be either *local*, for local damping of the suspension modes, or *global*, where actuators respond to the sensing and control signals from the interferometer for controlling the longitudinal and angular degrees of freedom of the test mass [97]. The application of these local and global forces are visible in Figure 6.2. Fine control forces are applied via an electrostatic drive (ESD), where an electrostatic force is produced by a gold pattern on the surface of the final reaction mass.

Larger control forces are generated between the top masses (for local control) and between the upper intermediate and penultimate masses (for global control) using coils and magnets. Initial LIGO employed a very simple version of these Optical Sensor and Electromagnetic Actuators, or *OSEMs*. The design evolved to produce two variations of the OSEM for Advanced LIGO: the Advanced LIGO OSEM (*AOSEM*), revised by the U.S. team, and the Birmingham OSEM (*BOSEM*), developed by the

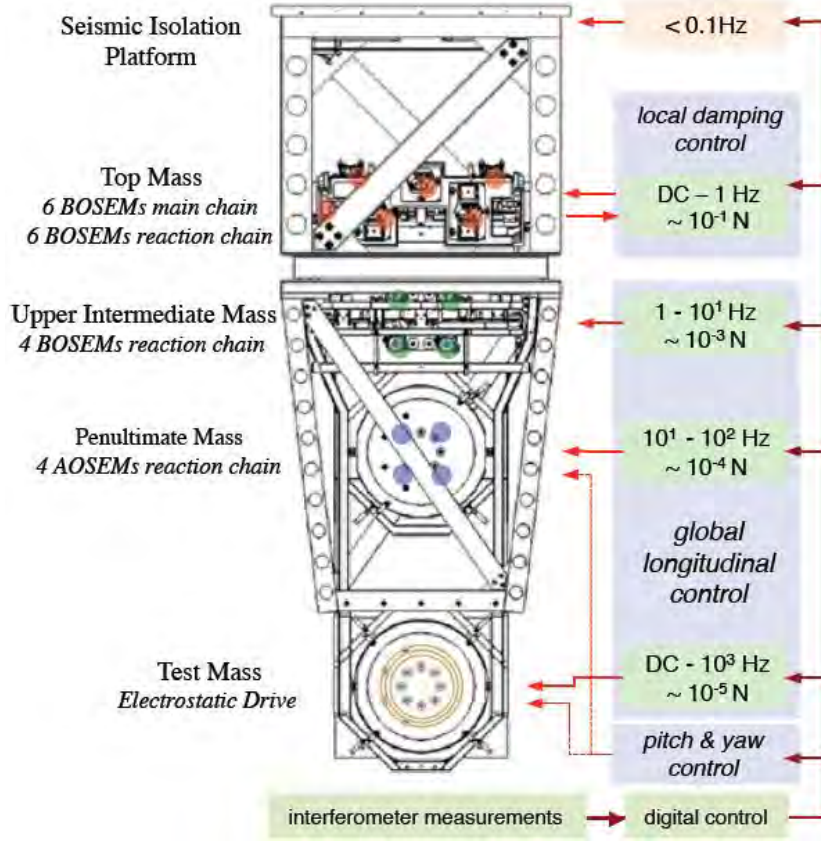


Figure 6.2.: Location of the different actuators and control forces on a quadruple suspension. Operating frequency ranges and maximum actuation forces are also shown [33].

team at the University of Birmingham.

The arrangement of the various actuators are shown in Figure 6.2: the top mass of the main and reaction chains each contain 6 BOSEMs, 4 BOSEMs are located on the upper-intermediate mass of the reaction chain, and 4 AOSEMs are attached to the penultimate mass of the reaction chain. We will now look at the BOSEMs in some further detail.

### 6.1.1. BOSEMs

Figure 6.3 is a computer-aided design (CAD) of a BOSEM, which is a position sensor with an integrated electro-magnetic actuator. It consists of an IRLED, quadrant PD, coil actuator, flexi-circuit and connectors to interface with the electronics.

Detection is carried out using a shadow-sensing technique, and the reference position is provided by a magnetic flag, such as the one shown in Figure 6.4(a). The design of the flag is the same as those used in the OSEMs for Initial LIGO, and is composed of a flag rod, magnet and spacer (although the method of mounting the flag to the spacer was modified during the development of the BOSEM - see Section 6.2). The flag is mounted on the main chain and is aligned with the BOSEM, which is attached to the reaction chain. The flag rests inside the centre of the BOSEM such that the tip of the flag partially obstructs the light between the IRLED and PD, as demonstrated by the CAD models in Figure 6.4(b). The magnetic portion of the flag sits within the coil, and actuation occurs from coil-drivers to maneuver the flag position, thus adjusting the position of the main suspension chain.

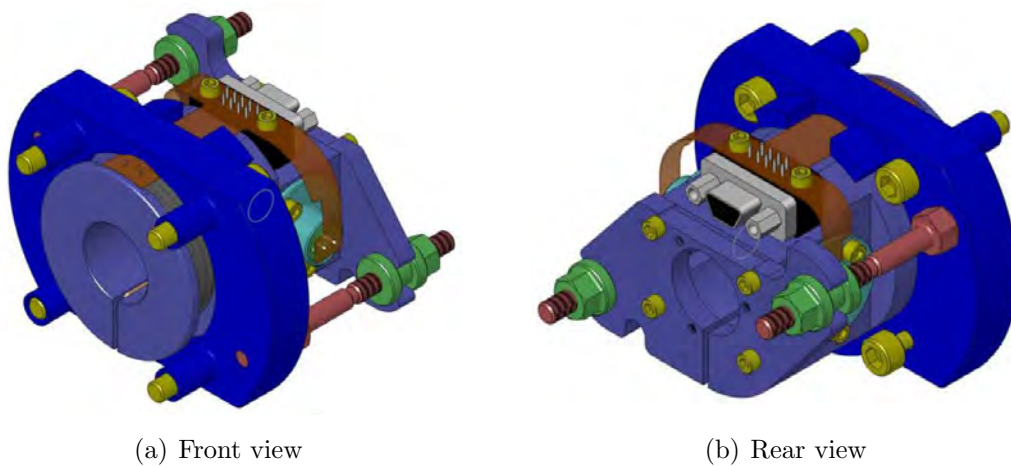


Figure 6.3.: A computer-aided design model of a BOSEM, showing front and rear views. [98]



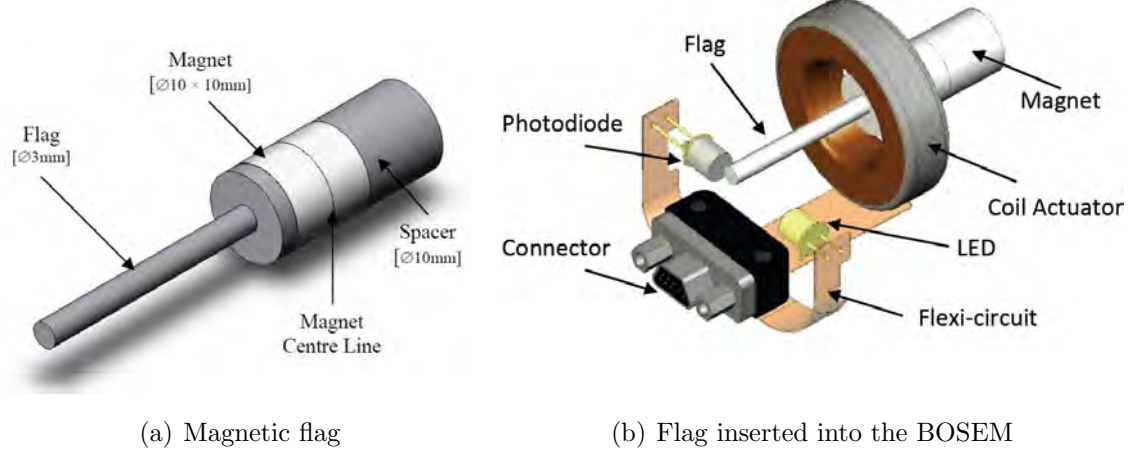


Figure 6.4.: Computer-aided design models of: (a) a close-up view of the magnetic flag constituents: flag rod, magnet and spacer [99], and (b) a partial BOSEM to illustrate the positioning of the magnetic flag [33].

The actuation force of the BOSEMs was 500 mN, much higher than the 50 mN in the Initial LIGO OSEMs. This was mainly achieved through a combination of an increased coil current, a larger number of coil windings and larger magnets.

## 6.2. Magnetic-mounted flag test

The flag used in initial LIGO (as shown in Figure 6.4(a)) was a construction of three parts: a flag rod, magnet and spacer. The flag rod and magnet were joined together using a vacuum leak sealant (Vacseal). The other end of the magnet was adhered to the spacer, also using Vacseal. The resulting flag can be seen in Figure 6.5(a).

The original Vacseal-mounted flags were extremely rigid and stiff, and this presented problems during installation or periods of high seismic activity such as an earthquake: if the flags exceeded their maximum displacement threshold, the flag rods were prone to snapping and breaking at one of the adhesion joints. Re-mounting

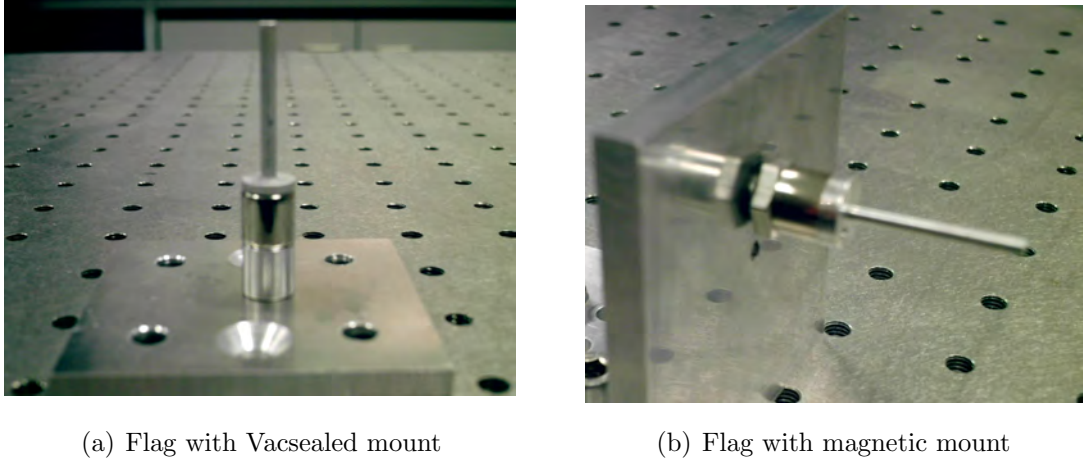


Figure 6.5.: (a) The flag assembled using Vacseal, as used in initial LIGO. (b) The proposed magnetic-mounted flag for Advanced LIGO.

the flag assembly was found to be very difficult and time-consuming.

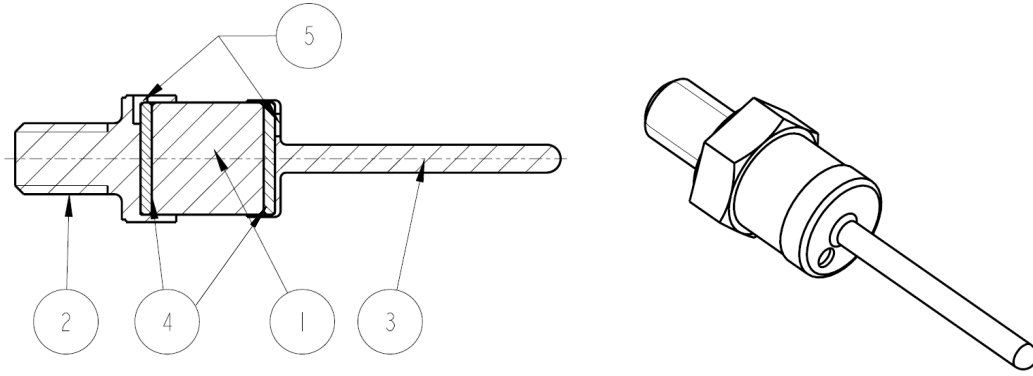
An alternative method of mounting the flag rod for Advanced LIGO was proposed - a new design was required which would allow the flag rod to return to its original position within the mount after incurring tiny displacements. A magnetic-mounted flag offered a versatile solution, as shown in Figure 6.5(b). The base of the new flag rod and the end of the spacer were both shaped as recessed caps, each containing a flat magnetic disc, illustrated by the cross-section Figure 6.6(a). The caps acted as magnetic plugs, allowing both ends of the magnet to fit securely within each cap. As an initial design, the spacer was in the form of a hexagonal screw, with a capped head. Figure 6.6(b) displays a 3-D image of the magnetic-mounted flag, and a detailed schematic can be found in Appendix E.1.

The capability of a magnetic-mounted flag to perform suitably in a BOSEM was assessed in terms of robustness, compared with the original Vacseal-mounted flag. Two qualities were investigated: *strength* and *maximum displacement*, and a description of each test and their results are given below.

## Strength testing

The strength of each flag was measured by fixing the flag horizontally and suspending weights from the end of the flag rod (5 mm from the tip), observed in Figure 6.7(a). Weights were added until either (a) the Vacseal bond broke, or (b) the magnetic force was overcome, causing the flag to detach from its mount.

The tests were repeated eleven times for the magnetic mount and three times for the Vacseal mount. The Vacseal-mounted flag was found to support a mean maximum weight of  $(2.00 \pm 0.05)$  kg before separating at the joint between the magnet and the spacer. In contrast, the magnetic-mounted flag could hold only a mean weight of  $(0.183 \pm 0.001)$  kg before the force between the magnet and the hexagonal screw gave way.



(a) Schematic of magnetic flag with magnetic mount

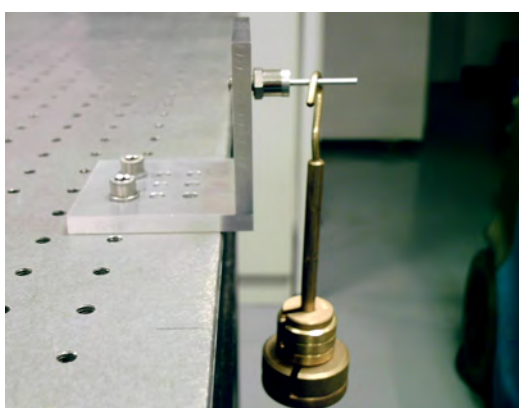
(b) 3-D view of the magnetic mount

Figure 6.6.: (a) Cross-section of the magnetic-mounted flag: ① Magnet, ② Hexagonal head screw, ③ Flag rod, ④ Magnetic plugs and ⑤ Vent holes. (b) A 3-D representation of the magnetic-mounted flag.

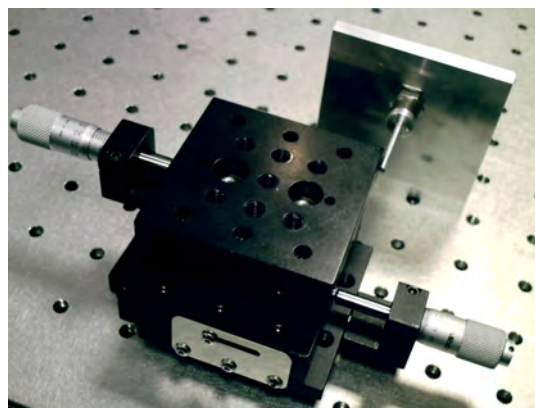
### Maximum displacement testing

Figure 6.7(b) demonstrates the setup used to determine the maximum displacement of the flag using a translation stage. Once again, the flags were secured horizontally, and the edge of the translation stage was aligned with the tip of the flag rod. Small displacements were made using micrometer adjusters, causing the translation stage to move in a direction perpendicular to the axis of the flag rod (parallel to the optics table). In the case of the Vacseal-mounted flag, the stage was translated until the Vacseal bond separated. For the magnetic-mounted flag, the translation stage was displaced a small amount and then returned to its starting point, causing the flag to tilt out and then snap back into its original position due to the magnetic force. The displacements were increased incrementally, until the flag and magnet were so tilted out of the hexagonal screw cap that they were prevented from returning to their neutral position.

The tests were repeated six times for the magnetic mount and three times for the Vacseal mount. The Vacseal-mounted flag underwent a mean maximum displace-



(a) Weight suspension



(b) Flag displacement

Figure 6.7.: (a) Weights suspended from the magnetic-mounted flag. (b) Displacement testing of the magnetic-mounted flag, with the translation stage at its starting reference position.

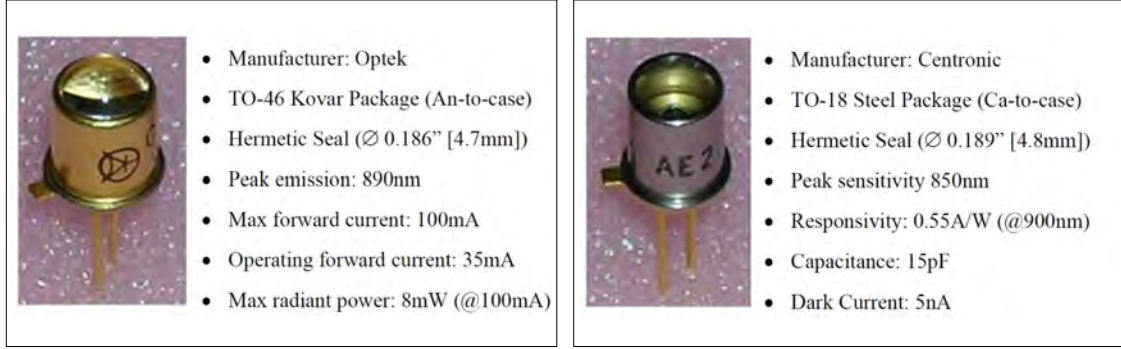
ment of  $(0.88 \pm 0.02)$  mm, with the breakage occurring between the magnet and spacer. The magnetic-mounted flag, on the other hand, sustained a mean maximum displacement of  $(12.85 \pm 0.01)$  mm.

## Conclusion

While the Vacseal-mounted flag was able to withstand a considerable amount of weight, the magnetic-mounted flag was able to tolerate a fairly large displacement force. In terms of preparation and assembly, the magnetic-mounted flag provided to be much easier and efficient to assemble. It also allowed control of the orientation of the flag (around the central axis of the flag rod) during installation, if necessary. If the flag were to separate from its mount, the magnetic-mounted flag can instantly be re-attached. In contrast, a Vacseal-mounted flag would require cleaning to remove any remaining Vacseal residue, followed by a bakeout over several days to cure the sealant before re-attachment. Based on these findings, the magnetic mount was therefore recommended for supporting the BOSEM flags in Advanced LIGO. Further details of the test procedures are reported in [100].

## 6.3. Infra-red LED and photodiode preparation

The BOSEM relies on shadow-sensing, where sensors are used to detect possible movement of the flag. These sensor components are displayed in Figure 6.8: the IRLED emits light, which is then detected by the PD. The flag rests orthogonal to the light path between the sensors such that the flag tip obstructs half of the light. Any increase or decrease in light is sensed by the PD, indicating that the flag (and therefore the main chain) position has moved, and actuation is applied via the BOSEM coil and flag magnet to move the main chain back to its original position.



(a) IRLED (OP232)

(b) PD (BPX65)

Figure 6.8.: Properties of the sensor devices used in the BOSEMs.[99]

According to the manufacturer's datasheet, the apertured radiant intensity of the IRLED was in the range of  $2\text{-}6\text{ mW/cm}^2$ , and unfortunately the devices could not be graded more specifically. Consequently, variations were found to occur in the output intensity of the IRLEDs during the early stages of sensor testing, sometimes as much as 50 %. Considering the high sensitivity levels required for the shadow-sensing technique, variations of this magnitude could result in uneven sensing and actuation of the suspensions. It was therefore essential that the IRLEDs installed in the detector retain minimum intensity variations. Although 654 BOSEMs were required, a batch of 2000 IRLEDs (OP232) and 2000 PDs (BPX65) were procured. Each IRLED device was subjected to a series of testing procedures in order that a suitable sample with relatively low intensity variations (between devices) could be selected.

### 6.3.1. Burn-in testing

A burn-in test was conducted to ensure that the output intensities of the IRLEDs were normalised. The test also helped to identify any faulty devices, since a failure



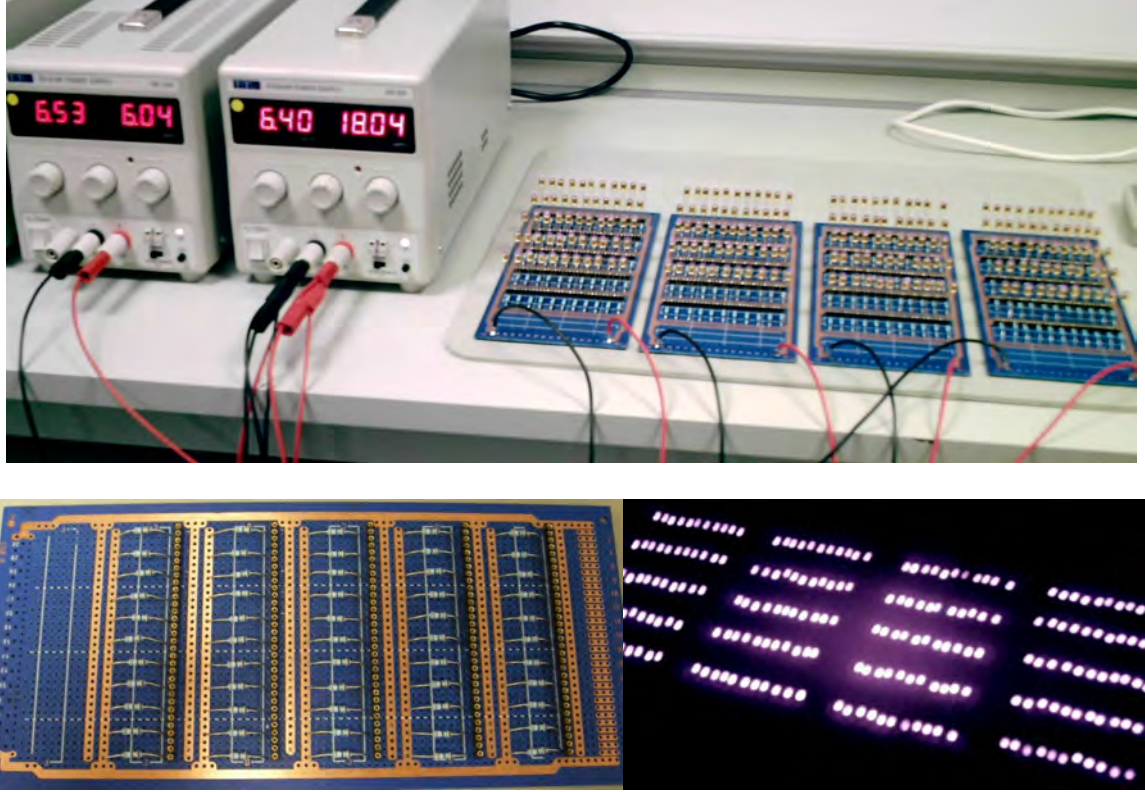


Figure 6.9.: Burn-in testing for the infra-red (IR) LEDs. *Top:* The setup for one batch of devices across four printed circuit boards (PCBs), powered at maximum current. *Bottom left:* PCB layout, capable of sustaining 55 IRLEDs. *Bottom right:* Powered IRLEDs during the the burn-in.

of an IRLED was most likely to occur well within 50 hours of operation, according to the manufacturer. Each device was powered at its maximum current (100 mA) continuously for 50 hours. The procedure was carried out over a period of about 21 days in batches of 200 devices using four printed circuit boards (PCBs), as seen in the top half of Figure 6.9. On the left are two power supplies, each connected to two PCBs. The design of the PCB is shown in the bottom left of Figure 6.9, with the IRLEDs plugged into dual in-line (DIL) sockets, enabling easy replacement of the devices, and 38 ohm resistors in parallel for each device. The infra-red light of the powered IRLEDs is visible in the bottom right of Figure 6.9. Every device passed

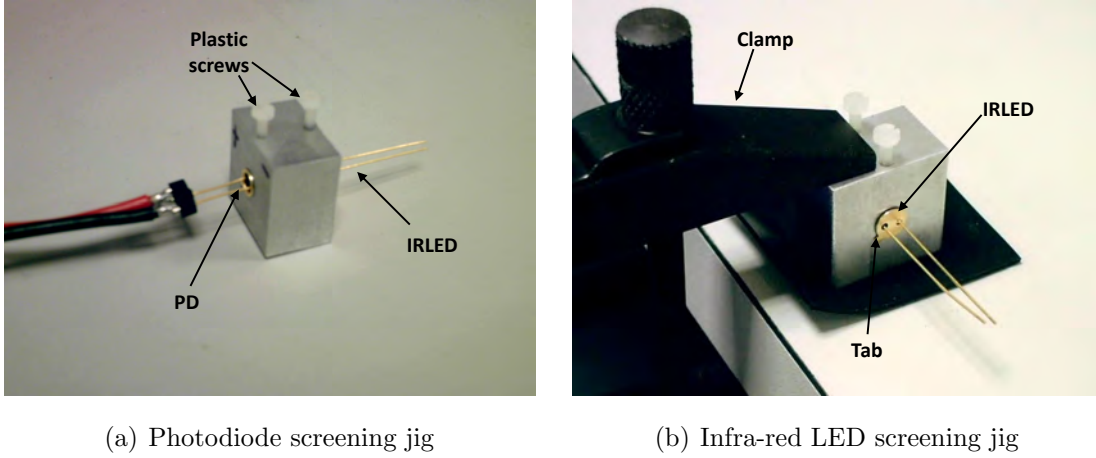


Figure 6.10.: A screening jig provided an efficient method of screening devices, with (a) a photodiode inserted on one side, and (b) an infra-red LED inserted on the other side.

the burn-in process successfully without any failures, and all IRLEDs continued to emit at maximum intensity.

### 6.3.2. Screening

The screening procedure for all IRLEDs was performed by driving each device at 35 mA<sup>1</sup> and observing its output intensity as detected by a single PD. Depending on the measured intensities, the IRLEDs were then separated into ‘bins’. An aluminium jig was created to aid the screening process in terms of time and accuracy. It accommodated one PD and one IRLED, positioned the same distance apart as they would be in a BOSEM (6.35 mm). Figure 6.10(a) displays the PD inserted into one side of the screening jig, with the legs connected to an ammeter. For consistency, the same PD device was used throughout the entire screening process for the IRLEDs. Figure 6.10(b) shows an IRLED inserted into the other side of the jig, and the exposed legs were then easily connected to a power supply. The jig was clamped to

---

<sup>1</sup>The supply current is at 35 mA during operation in Advanced LIGO



the table for stability, while two white plastic screws on top of the jig ensured that the inserted PD and IRLEDs remained steady.

The flanges on both the PDs and IRLEDs incorporated a tiny tab, just visible in Figure 6.10(b) at the base of the IRLED (in the ‘8 o’clock’ position). The location of these tabs was identical for every device, thereby serving as a reliable reference point. This allowed all screened devices to be orientated in exactly the same way, also for consistency.

A sample of about 200 devices were screened first to establish the range of intensities. The range for each bin spanned  $1\ \mu\text{A}$ , with the lowest bin range of  $47\text{--}48\ \mu\text{A}$  and the highest bin range of  $77\text{--}78\ \mu\text{A}$ . For extreme cases, two extra bins were included for devices with intensity values which were unusually low ( $< 47\ \mu\text{A}$ ) or high ( $> 78\ \mu\text{A}$ ). The nominal value was quoted by the manufacturer to be  $60\ \mu\text{A}$ ; each bin therefore offered an intensity variance of about 2% around this nominal value, well within the permitted range of 15%<sup>2</sup>. This meant that devices from seven consecutive bins could be selected, since a single bin was unlikely to contain a sufficient number of 654 IRLEDs.

Figure 6.11 shows the distribution of IRLED intensities after completion of the screening process for all 2000 devices. The orange bars indicate seven consecutive bins with the highest population of devices, ranging from  $58\text{--}65\ \mu\text{A}$  - these bins contained 698 devices in total, which were selected for installation in the BOSEMs. A detailed breakdown of the number of BOSEMs required for various parts of the Advanced LIGO detector is given in Appendix E.2.

---

<sup>2</sup>This figure of 15% was computed by the Suspensions group at the Rutherford Appleton Laboratory.

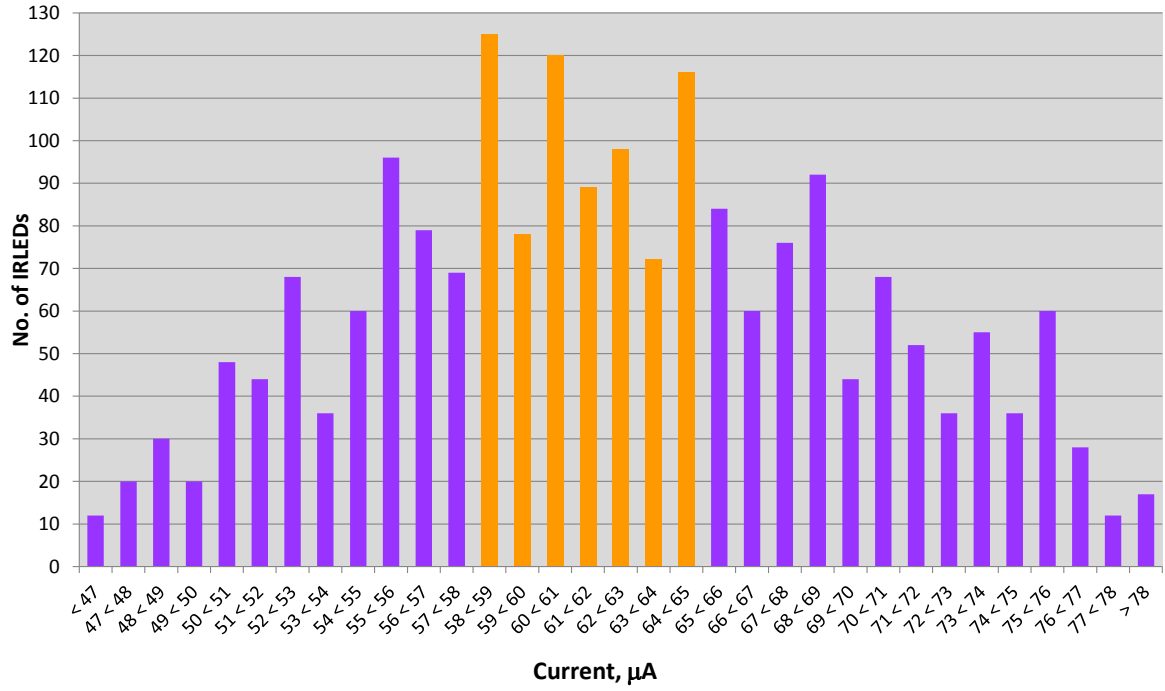


Figure 6.11.: Distribution of measured intensities for 2000 infra-red LEDs. The orange bars represent the bins containing the largest number of devices, with intensity variations well within the acceptable range of 15%.

## 6.4. BOSEM testing procedure

The BOSEMs were fabricated and assembled in cleanrooms at the University of Birmingham ([101] provides a specification). Once assembled, it was essential to test the BOSEMs thoroughly and verify that they met the performance requirements (which can be found in [99]). A specific automated test procedure was developed, intended to be carried out on every BOSEM in two stages: on the *part-assembled* coil-former (Figure 6.12(a)) and the *fully-assembled* BOSEM (Figure 6.12(b)). Note that all testing procedures were carried out in a clean-room environment. A fully detailed description of the procedure is given in [102], while the account below focuses on my input.

### 6.4.1. Part-assembled testing

The first stage of testing involved measuring the coil continuity and coil insulation using a digital voltmeter (DVM), as seen in Figure 6.13. This was to identify any faults between the coil and the flexi-circuit. The resistance between the body and the coil start/end points were measured and compared to the criteria specified in [102].

### 6.4.2. Fully-assembled testing

The second test stage was conducted in two parts: the first was to test the high-voltage (HV) insulation breakdown, and the second was the parameter testing using the Automated Test Equipment (ATE).



(a) Part-assembled coil-former



(b) Fully-assembled BOSEM

Figure 6.12.: Automated testing was performed in two stages: on a (a) part-assembled coil-former, and (b) fully-assembled BOSEM.

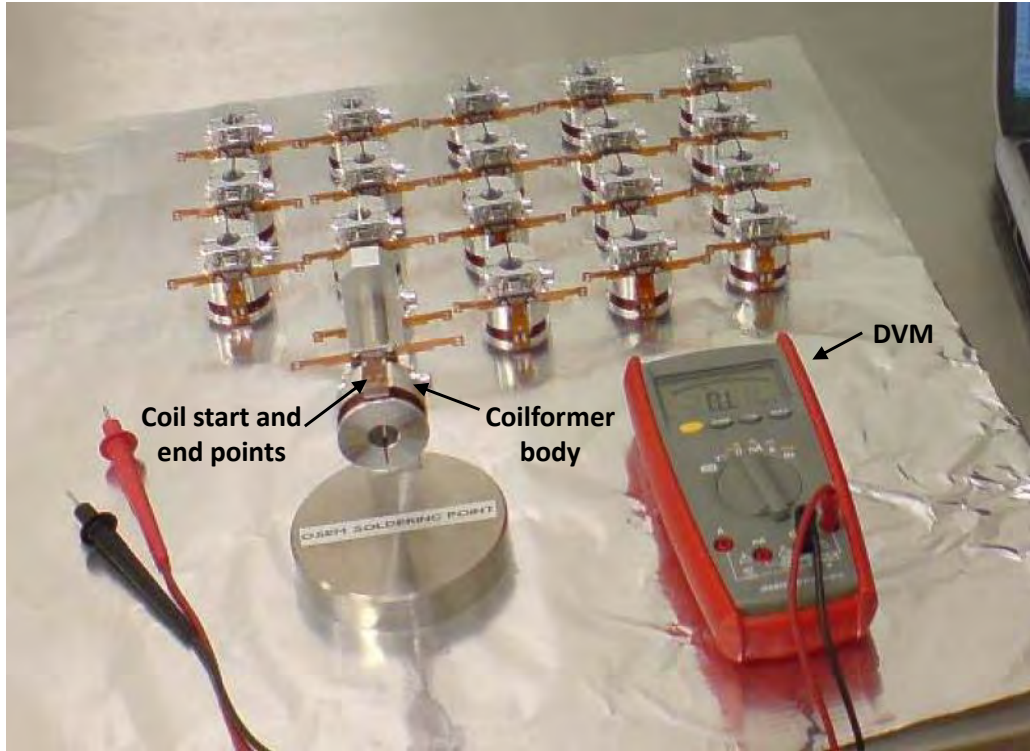


Figure 6.13.: The part-assembled BOSEMs are tested between the coil and the flexi-circuit [102].

### HV insulation breakdown

The purpose of this test was to ensure that the coil insulation did not deteriorate and to eliminate any risk of short-circuiting with the coilformer. Figure 6.14 reveals the setup, where 200 V at 20 mA were applied to each BOSEM via a power supply and a remote activation switch. If there was any fault with the coil, the blue light in the indicator box would light up to indicate that the BOSEM had failed the test.

### ATE

The next phase in testing was to measure key parameters of each fully-assembled BOSEM using the ATE setup shown in Figure 6.15. A general purpose interface bus

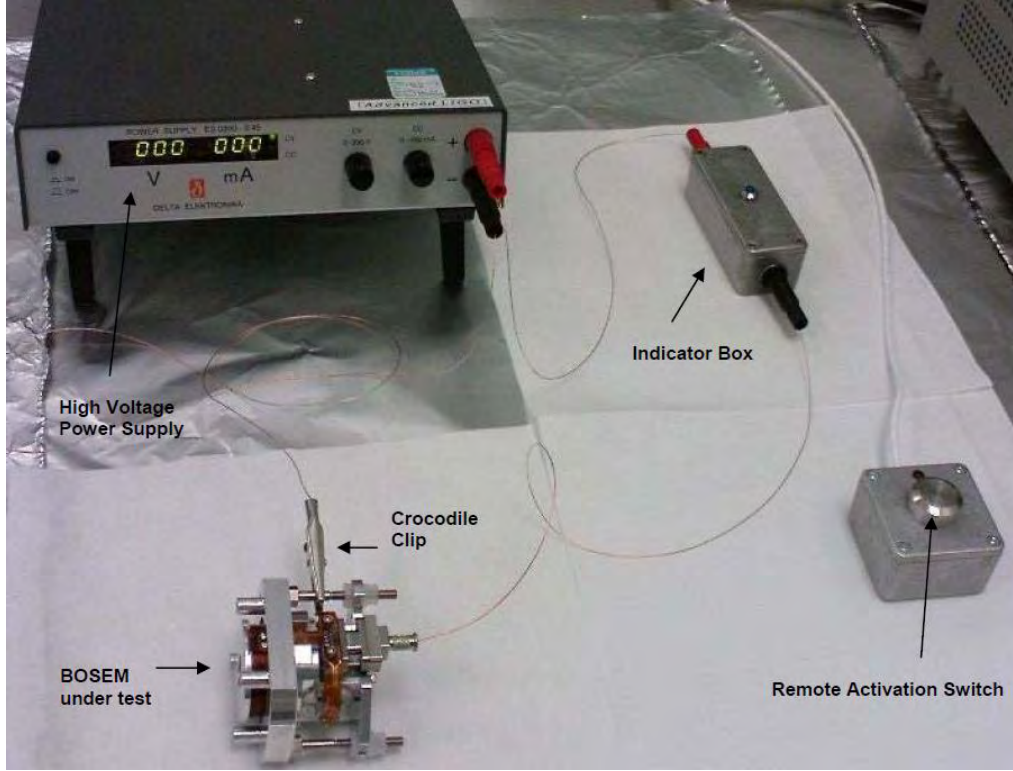


Figure 6.14.: The first test performed on a fully-assembled BOSEM is for high-voltage insulation breakdown [102].

(GPIB) enabled a connection between the Keithley digital multimeter (DMM) and Wayne Kerr LCR<sup>3</sup> meter, and then interfaced with a laptop using a USB-to-GPIB controller. The Keithley meter, Wayne Kerr meter (via a junction box), low-voltage power supply, laptop and BOSEM were combined at a central interface box. It should be noted that the automated testing described here can also be performed on AOSEMs and noise-prototype OSEMs (NPOSEMs). [102]

Testing of each BOSEM lasted for around 30 seconds, and the data was processed using the ATE software installed on the laptop. The readings were displayed on-screen in the form of a graphical user interface (GUI), as illustrated in Figure 6.16. The measurements were also saved in a log file in a similar format, seen in Figure 6.17. The heading contains information relating to the directory in which the data is

<sup>3</sup>LCR is an abbreviation for inductance (L), capacitance (C) and resistance (R)

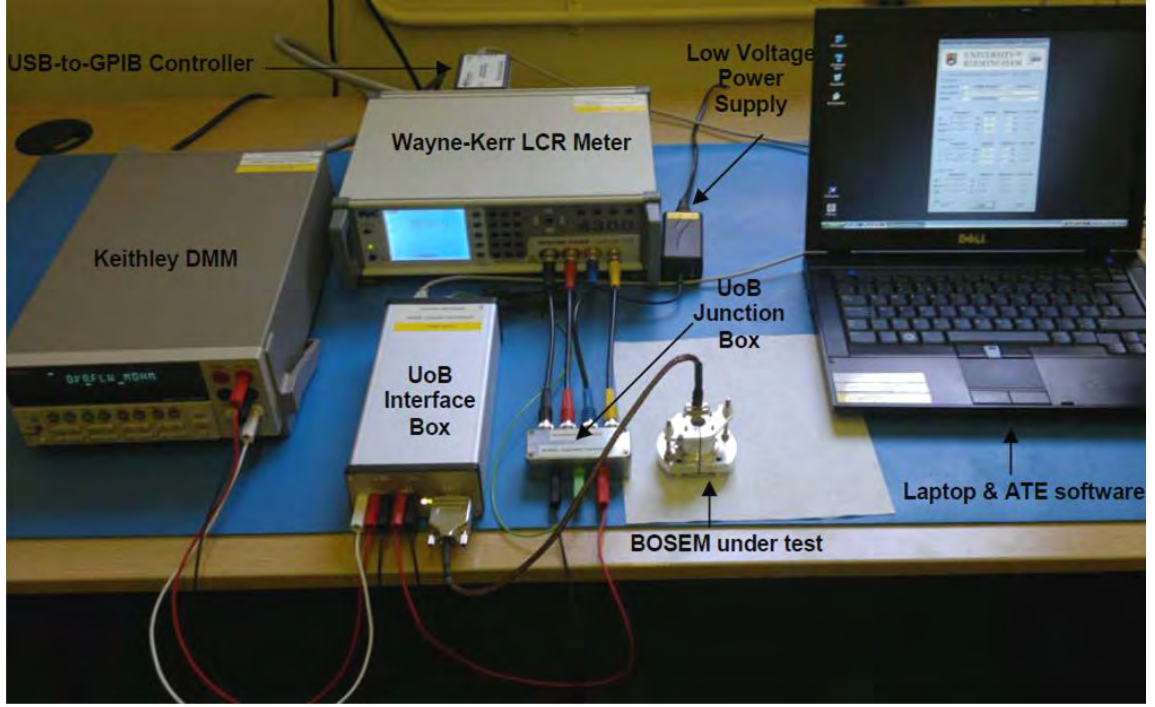




Figure 6.15.: The second test involved the automated test equipment to test a range of key parameters in a fully-assembled BOSEM [102].

stored, date and time stamp, initials of the user and the location of the testing. Below the heading, the parameters are given in the first column and the corresponding measurements are recorded. The requirements, provided by the nominal values in the third column and the tolerances in the fourth column, must be satisfied. If the measured values fell either within or outside the specified range, then that particular parameter automatically passed or failed respectively, indicated in the fifth column. The BOSEM was deemed successful when all parameters were passed.

Note that the nominal values and tolerance ranges were set manually, and some figures were later revised, for example the nominal value of the intensity (detected by the PD) was adjusted from  $60 \mu\text{A}$  to  $62.5 \mu\text{A}$ , and the tolerance range was increased from 15 % to 28 % (as observed in Figure 6.16 and [102]). This particular amendment was due to the focusing effects of the lens inside the IRLED carrier ([101]), and as a



Advanced LIGO - OSEM Automated Test Equipment - Version 3.4


**UNIVERSITY OF BIRMINGHAM**


S.Aston, R.Parry and D.Lodhia. For assistance refer to [LIGO-T070107](mailto:LIGO-T070107)

Configuration:

Com Port #  Initials  Serial #  Auto Inc. ☐

Description

Directory

OSEM Type ☒ IPOSEM ☐ BOSEM ☐ AOSEM ☐

Sensor Tests

	Measured	Nominal	Tolerance	Pass/Fail
PD	<input type="text"/>	$\mu\text{A}$ <input type="text" value="62.5"/>	<input type="text" value="28"/> %	
IRLED	<input type="text"/>	$\text{mA}$ <input type="text" value="35"/>	<input type="text" value="2"/> %	
Ratio	<input type="text"/>	% <input type="text" value="0.17857"/>	<input type="text" value="28"/> %	

Actuator Tests

	Measured	Nominal	Tolerance	Pass/Fail
L	<input type="text"/>	$\text{mH}$ <input type="text" value="14.7"/>	<input type="text" value="7"/> %	
Q	<input type="text"/> @ <input type="text"/>	$\text{Hz}$ <input type="text" value="0.243"/>	<input type="text" value="10"/> %	
R	<input type="text"/>	$\Omega$ <input type="text" value="37.6"/>	<input type="text" value="8"/> %	

Insulation Tests

	Measured	Nominal	Tolerance	Pass/Fail
PD	<input type="text"/>	$\Omega$ <input type="text" value="1E9"/>	<input type="text" value="250E6"/>	
IRLED	<input type="text"/>	$\Omega$ <input type="text" value="1E9"/>	<input type="text" value="250E6"/>	
Coil	<input type="text"/>	$\Omega$ <input type="text" value="1E9"/>	<input type="text" value="250E6"/>	

Status:

Figure 6.16.: Test measurements obtained using the automated test equipment are displayed as a GUI [102].

result the IRLED was found to emit a slightly increased light intensity as detected by the paired PD within a fully-assembled BOSEM.

This automated test was designed to be repeated as necessary over the lifetime of the BOSEM, especially when shipped overseas to check for possible damage. Each BOSEM was engraved with a unique serial number, which was logged each time it was tested (see the top of Figures 6.16 and 6.17). The data was automatically

Advanced LIGO - BOSEM Automated Test Equipment - Version 3.0				
C:\ATE\Test Data\D060218-C\SERIAL_No001.txt      2008/11/26   12:07:33				
SMA      Final UHV-clean assembled BOSEM tests at Uni. of Birmingham				
Parameter	Measured	Nominal	Tolerance	Pass/Fail
Sensor				
PD(uA)	65.83	60	15%	PASS
IRLED(mA)	35.00	35	5%	PASS
Ratio(%)	0.19	0.17	15%	PASS
Actuator				
L(mH)	14.75	14.7	5%	PASS
Q@100(Hz)	0.242	0.243	5%	PASS
R(Ohms)	37.69	37.6	5%	PASS
Insulation				
PD(Ohms)	>250E6	1E9	250E6	PASS
IRLED(Ohms)	>250E6	1E9	250E6	PASS
Coil(Ohms)	>250E6	1E9	250E6	PASS

Figure 6.17.: The log file generated by the automated test equipment. If the measured values for all parameters meet the requirements given by the nominal and tolerance values, the BOSEM passes the test.

stored in the same log file corresponding to that particular BOSEM, allowing the performance of that BOSEM to be monitored over time.

### ATE statistical analysis

Once the log files were obtained for each BOSEM, subsequent analyses on the intensities, resistances and inductances were performed. The log files were imported into separate Excel spreadsheets and data was collated using a script (detailed in Appendix E.3) which treated the entire Excel workbook as 3-dimensional. This was possible because the value of each parameter was stored in the same cell coordinates, despite being in separate worksheets. For example, all current values were



accumulated into a separate table, with the first column represented the BOSEM serial numbers and the second column contained the measured current values. This enabled a plot of the distribution of data to be generated efficiently, and the spread of values could be examined.

I performed the ATE statistical analysis technique described above on the first batch of one hundred fully-assembled BOSEMs using the ATE. Figure 6.18 shows the spread of measured intensities, resistances and inductances respectively. Note that once I demonstrated the results of the analysis successfully, analysis of the remaining 554 BOSEMs was continued by other colleagues. A total of 654 BOSEM devices were eventually collected, all having passed the testing using the ATE.

### 6.4.3. BOSEM characterisation

It is important to note that the ATE testing was performed in ‘free-air’ in a clean-room environment, and did not reflect a complete analysis of the performance of the BOSEM. A full quality check required the BOSEM to be tested in the same environment as that in which it would be operating. This final characterisation procedure involved testing the noise performance of all 654 BOSEMs through a range of frequencies while the light emitted by its IRLED was half obscured by a flag, imitating the true setup for Advanced LIGO (a further description of the characterisation method can be found in [103]). These tests were performed both in free-air and in-vacuum, and the resulting BOSEM displacement sensitivity noise measurements were found to be consistent.

However, the BOSEMs were displaying displacement sensitivity noise levels of up to  $3 \times 10^{-10} \text{ m Hz}^{-1/2}$  at 10 Hz, and were not meeting the requirement of  $1 \times 10^{-10} \text{ m Hz}^{-1/2}$  at 10 Hz. The cause of this extra noise was due to the Optek IRLEDs

- it was discovered that excess amounts of epoxy were bridging the cathode part of the IRLED to its anode casing, and as a result the IRLEDs were exhibiting high photo-current noise. An alternative IRLED, the Vishay TSTS7100, were newly available commercially, and after testing were found to be comparable to the Optek devices but revealed lower levels of photo-current noise. All Optek IRLEDs in the BOSEMs were replaced with the Vishay devices, re-tested using the ATE (with a 100% pass rate) and re-characterised - all BOSEMs displayed displacement sensitivity noise levels well below the requirement of  $1 \times 10^{-10} \text{ m Hz}^{-1/2}$  at 10 Hz. More details can be found in [103].

A total of 654 BOSEMs were successfully delivered to the U.S. for testing and installation, with the final batch shipped in March 2011. Upon arrival in the U.S., a random sample of 100 BOSEMs were selected from the total amount to be re-characterised in-vacuum to ensure that they were still fully functional, and a 100 % pass rate was reported [103].

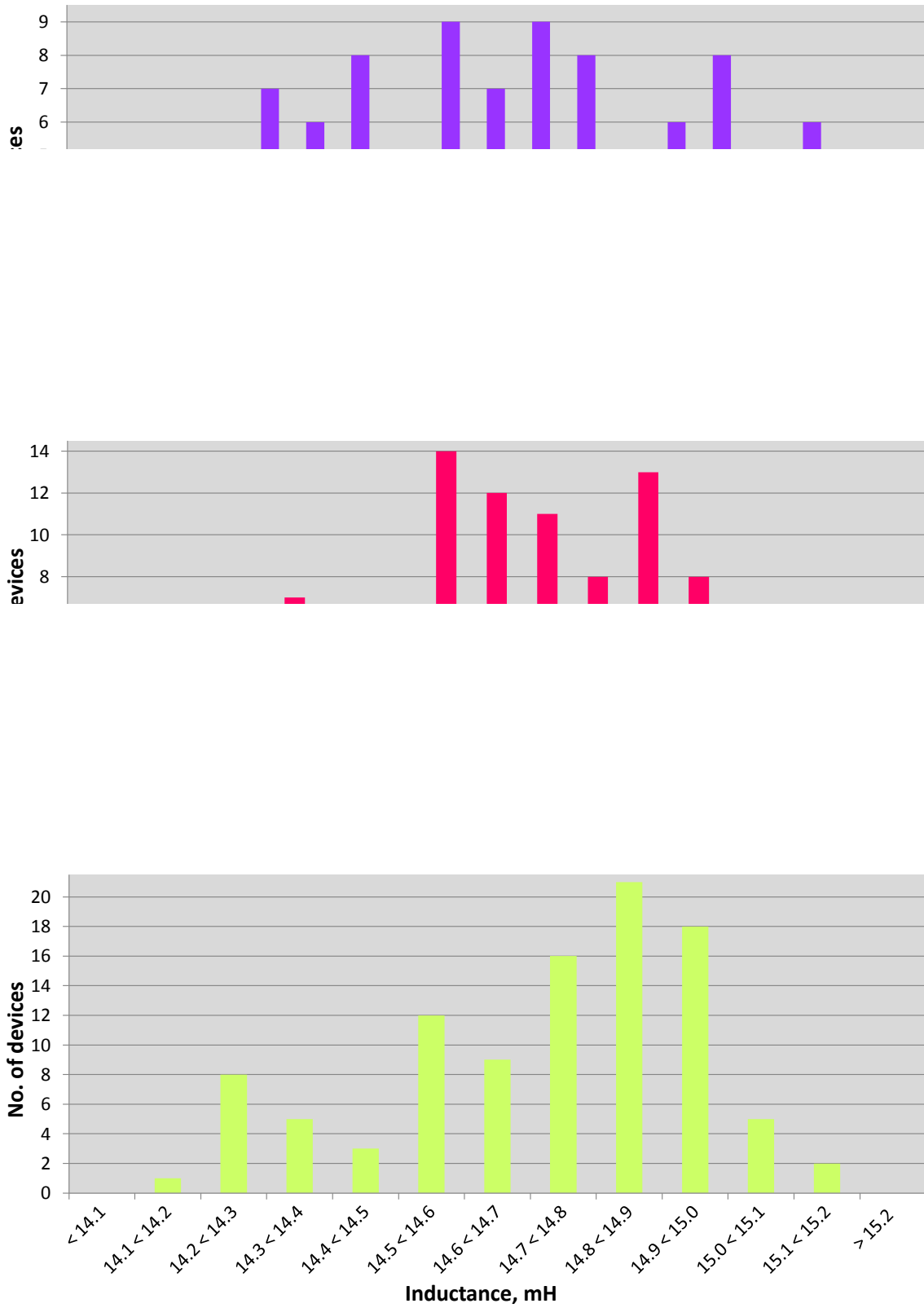


Figure 6.18.: Distribution of intensities (top), resistances (middle) and inductances (bottom), resulting from the automated testing procedure on 100 BOSEMs.

# Appendix A.

## Beam profile and parameters

### A.1. Mode-matching the beam

*Just another mode matching tool* (JamMt) [87] is an application developed for the purpose of mode-matching. It was used in the context of this work to determine the appropriate combination of lenses to mode-match the laser beam into the MC, as described in Section 3.2.1, and the result can be seen in Figure A.1.

The mode-matching tool was also used to compute a suitable combination of cylindrical lenses in the PZT arm of the MZ setup in Section 3.2.3, ensuring that the circular beam shape was transformed to match the elliptical beam along the grating arm. Figure A.2 displays the outcome.

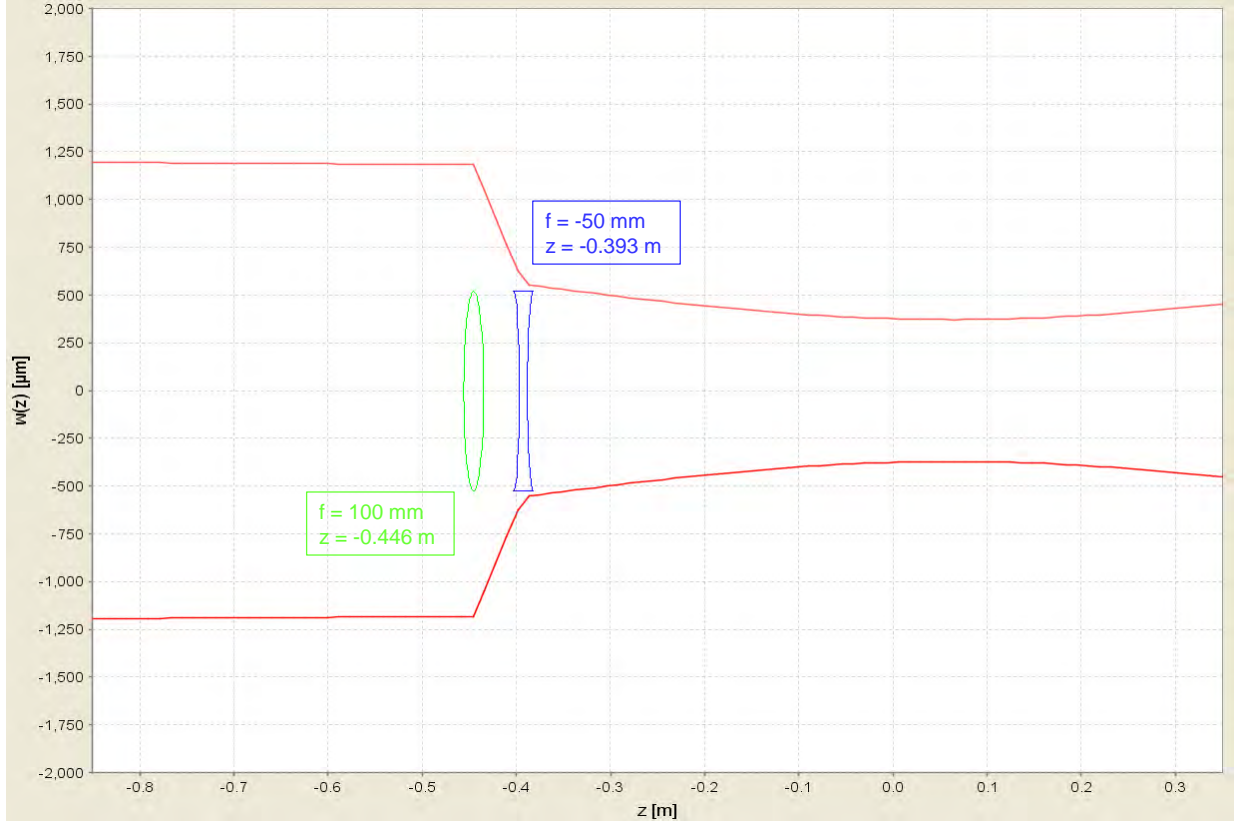


Figure A.1.: JamMt simulation tool for mode-matching the beam into the mode cleaner to give the desired beam waist size and location. Initial beam:  $\omega_0 = 1183 \mu\text{m}$ ,  $z_0 = -0.255 \text{ m}$ ; resulting beam:  $\omega_0 = 371.221 \mu\text{m}$ ,  $z_0 = 0.064 \text{ m}$ .

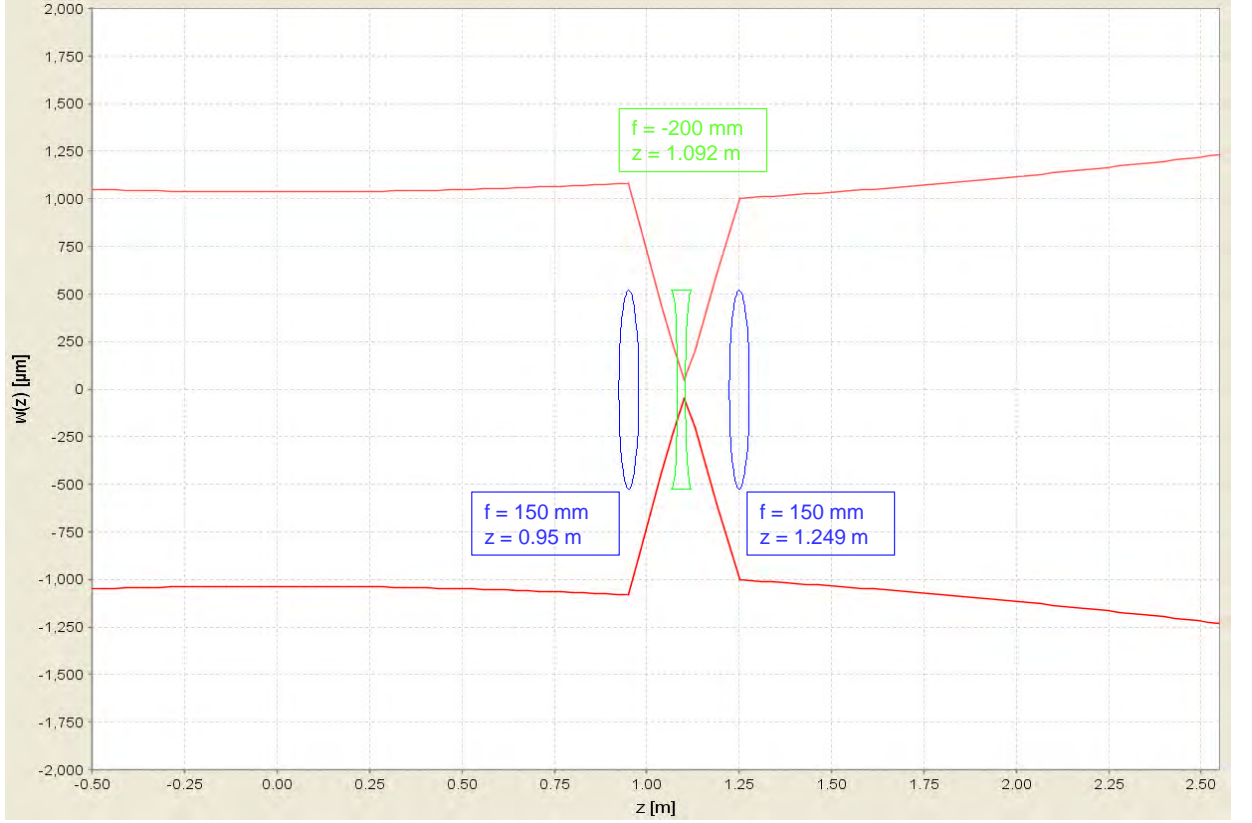


Figure A.2.: JamMt simulation tool for mode-matching the circular beam in the PZT path to match the elliptical beam shape in the grating path using cylindrical lenses. Initial beam:  $\omega_0 = 1036 \mu\text{m}$ ,  $z_0 = 0 \text{ m}$ ; resulting beam:  $\omega_0 = 950.472 \mu\text{m}$ ,  $z_0 = 0.356 \text{ m}$ .

## A.2. Beam characterisation

After exiting the MC, the laser beam passed through a set of collimating lenses, as mentioned in Section 3.2.1. To ensure that the resulting beam was fairly well collimated, a beam profiler was used to measure the beam shape at various distances of propagation and determine the waist size, waist position and Rayleigh range along the  $x$ -axis (horizontal direction) and  $y$ -axis (vertical direction), as illustrated in Figure A.3.

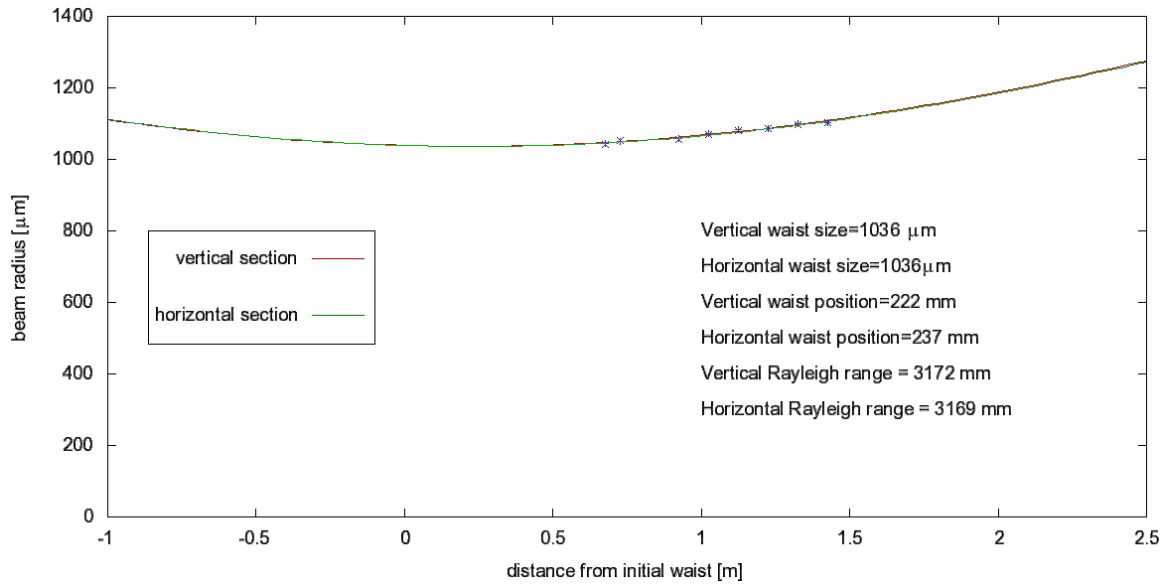


Figure A.3.: Measured beam profile after the mode cleaner and collimating lenses and before entering the main interferometer setup.

### A.3. Matlab script to determine new beam parameters after grating diffraction

The script below was developed using Matlab to compute new beam parameters after a beam is diffracted by a grating. Any input values can be chosen for the incident beam using the following beam parameters: wavelength, index of refraction, waist size radius and the distance of the grating from the waist position. The angles of incidence and reflection of the beam are set to  $10^\circ$  and  $28^\circ$  respectively, as required by my table-top experimental setup. The new waist size and waist position along the  $x$ -axis are computed for the diffracted beam.

```
%-----  
-----  
  
% Script which computes the new position and waist size of a beam (in  
% the x and y axis) after propagating a distance z, reflected off a  
% grating, and propagated further where it reaches an end beamsplitter.  
%  
% The input arguments are the wavelength (lambda), index of refraction  
% (nr), original waist size (w0), and distance from the waist to the  
% grating (z).  
%  
% The grating reflection causes a change in the beam size in the x-  
% direction (the y-direction remains unchanged).  
% The new beam size (and hence new q parameter) in the x-direction  
% is computed.  
%  
% At the end beamsplitter, the resulting q parameters (in x and y)
```



```
% yields the new corresponding waist sizes and positions (also in
% x and y).
%
clear all;

% input arguments
lambda = 1064e-9;
nr = 1;
w0 = 1036e-6;
z = 1.152;
[0.5pt]
% beam is propagated to the grating
gp=FT_init_gauss_param(lambda,nr,'w0',w0,'z',z);

% computing new beam size in x-direction when reflected at grating
new_w = gp.w*(cos(28*pi/180)/cos(10*pi/180));

% computing new q parameter when reflected at grating
gp3 = FT_init_gauss_param(lambda,1,'w',new_w,'Rc',gp.Rc);

% q parameter in the x-direction (at grating)
q3(1)=gp3.q(1);

% q parameter in the y-direction (at grating)
q3(2)=gp.q(2);

% propagates the beam (along distance of 1.14m) to reach the end
% beamsplitter and computes the new q parameter at the end beamsplitter
```

```
gp4=FT_init_gauss_param(lambda,nr,'q',q3);

gp5=gp4;
gp5.q=gp5.q+1.14;
gp5 = FT_update_gauss_param(gp5,gp5.q,1);

% takes the new q parameters and computes the new corresponding waist
% sizes (in x and y), and also calculates respective waist positions
disp(sprintf('beam at BS is:\ n'));
disp(sprintf('w0x=%.5g, z0x=%.5g\ n',gp5.w0(1),gp5.z(1)));
disp(sprintf('w0y=%.5g, z0y=%.5g\ n',gp5.w0(2),gp5.z(2)));

% compute values for JamMt
```

## Appendix B.

# Pound-Drever-Hall laser frequency stabilisation

### B.1. Modulation concept

By operating on one side of these resonances, a small change in laser frequency would result in a large change in transmitted light. The transmitted intensity could be measured and fed back to the MC PZT, thus holding this intensity constant. However we encounter the problem that the transmission intensity is symmetric around the resonance peak. Any drift out of resonance is difficult to correct if we cannot distinguish which side of resonance the frequency had drifted to, making it unclear whether an increase or decrease in the frequency was required to return to resonance.

We overcome this by looking at the *derivative* of the transmitted intensity, which is antisymmetric about resonance. By dithering (or modulating) the laser frequency  $\omega_0$  by a very small amount, we can identify which side of resonance the frequency is on.

From Figure 3.4(b) we see that below resonance, the derivative of the transmitted intensity is positive, meaning that the intensity increases with increasing frequency. Modulating the frequency sinusoidally means that the transmitted intensity will vary sinusoidally in phase. Above resonance, the derivative is negative, i.e. the transmitted intensity decreases with increasing frequency, and a sinusoidal modulation will cause the transmitted intensity to vary sinusoidally  $180^\circ$  out of phase. Note that on resonance, the transmitted intensity remains unchanged when a small frequency variation is applied.

## B.2. Carrier and sidebands

When the laser (carrier) frequency,  $\omega_0$ , is modulated at a frequency of  $\Omega$ , sidebands are created; this is the result of interfering two waves with different frequencies. The lower sideband has a frequency of  $\omega_0 - \Omega$ , and the upper sideband has a frequency of  $\omega_0 + \Omega$ . Interfering the modulation sidebands with the reflected beam produces a beat pattern at the modulation frequency, and it is the phase of this beat pattern which provides the phase of the reflected beam. It can then be determined how much the laser frequency is above or below resonance, as shown in Figure B.1.

The electric field of a laser beam can be written as  $E_0 e^{i\omega_0 t}$ . After passing through the EOM, the electric field becomes

$$E_{inc} = E_0 e^{i(\omega_0 t + \beta \sin \Omega t)}. \quad (\text{B.1})$$

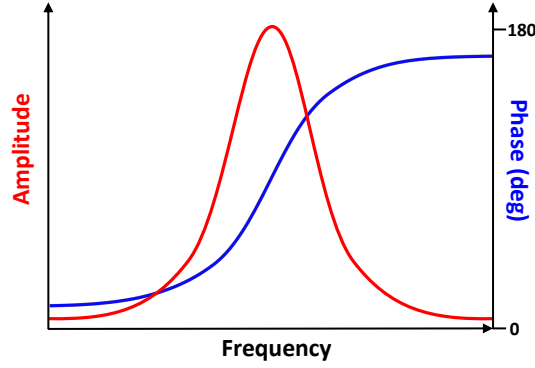


Figure B.1.: Phase (blue) of the beat pattern generated by the interference of the modulation sidebands. On either side of beam resonance (red), the derivative of the phase has opposite signs, thus enabling the system to correctly return to resonance.

This expression can be expanded using Bessel functions to give

$$\begin{aligned} E_{inc} &\approx E_0 [J_0(\beta) + 2iJ_1(\beta) \sin \Omega t] e^{i\omega_0 t} \\ &= E_0 [J_0(\beta)e^{i\omega t} + J_1(\beta)e^{i(\omega_0+\Omega)t} - J_1(\beta)e^{i(\omega_0-\Omega)t}], \end{aligned} \quad (\text{B.2})$$

where  $\Omega/2\pi$  is the phase modulation frequency, and  $\beta$  is the modulation index<sup>1</sup>. Three different fields can be seen in this expression: a carrier (with frequency  $\omega_0/2\pi$ ), and two sidebands (with frequencies  $(\omega_0 \pm \Omega)/2\pi$ ). If the total power is  $P_0 = |E_0|^2$ , then power in the carrier  $P_c$  and the power in each of the first-order sidebands  $P_s$  are given as

$$P_c = J_0^2(\beta)P_0, \quad \text{and} \quad P_s = J_1^2(\beta)P_0 \quad (\text{B.3})$$

If the modulation depth is small ( $\beta < 1$ ), it means that almost all of the power lies in the carrier and the first-order sidebands,  $P_c + P_s \approx P_0$ .

---

<sup>1</sup>The modulation index describes how much the modulated variable varies around the carrier.

### B.3. Power in the reflected beam

We now look at how the appropriate terms are isolated from the PD signal. The reflected beam from a Fabry-Perot cavity has the same electric field as the incident beam multiplied by the *reflection coefficient*,  $F$ :  $E_{ref} = F E_{inc}$ . In the case of several fields (one carrier and two sidebands), each field in the reflected beam is multiplied by the reflection coefficient as follows:

$$\begin{aligned} E_{ref} = & E_0 [F(\omega_0) J_0(\beta) e^{i\omega_0 t} \\ & + F(\omega_0 + \Omega) J_1(\beta) e^{i(\omega_0 + \Omega)t} \\ & - F(\omega_0 - \Omega) J_1(\beta) e^{i(\omega_0 - \Omega)t}], \end{aligned} \quad (\text{B.4})$$

from which the power of the reflected beam can be derived. Before continuing, let us denote the terms to simplify the algebra as follows:

$$\begin{aligned} F_0 &= F(\omega_0) e^{i\omega_0 t} \\ F_+ &= F(\omega_0 + \Omega) e^{i(\omega_0 + \Omega)t} \\ F_- &= F(\omega_0 - \Omega) e^{i(\omega_0 - \Omega)t}, \end{aligned}$$

and their complex conjugates as

$$\begin{aligned} F_0^* &= F^*(\omega_0) e^{-i\omega_0 t} \\ F_+^* &= F^*(\omega_0 + \Omega) e^{-i(\omega_0 + \Omega)t} \\ F_-^* &= F^*(\omega_0 - \Omega) e^{-i(\omega_0 - \Omega)t}. \end{aligned}$$

The power in the reflected beam is given by  $P_{ref} = |E_{refl}|^2 = E^*E$ . Using Equation (B.4), this gives us:

$$\begin{aligned} E^*E &= |F_0|^2 + |F_+|^2 + |F_-|^2 \\ &+ [F_0F_+^*] - [F_0^*F_-] + [F_0^*F_+] - [F_0F_-^*] - \underbrace{[F_+F_-^*] - [F_-F_+^*]}_{2\Omega \text{ terms}}. \end{aligned} \quad (\text{B.5})$$

The last two terms can be shown to partly cancel:

$$\begin{aligned} F_+F_-^* &= e^{i(\omega_0+\Omega)t}e^{-i(\omega_0-\Omega)t} \\ &= e^{i\omega_0t}e^{i\Omega t}e^{-i\omega_0t}e^{i\Omega t} = e^{2\Omega t} \\ F_-F_+^* &= e^{i(\omega_0-\Omega)t}e^{-i(\omega_0+\Omega)t} \\ &= e^{i\omega_0t}e^{-i\Omega t}e^{-i\omega_0t}e^{-i\Omega t} = e^{-2\Omega t}. \end{aligned}$$

This leaves us with two  $\Omega$  terms. Equation (B.5) can be rewritten as:

$$\begin{aligned} E^*E &= |F_0|^2 + |F_+|^2 + |F_-|^2 \\ &+ \underbrace{[F_0F_+^*] - [F_0^*F_-]}_C + \underbrace{[F_0^*F_+] - [F_0F_-^*]}_{C^*} + (2\Omega \text{ terms}). \end{aligned} \quad (\text{B.6})$$

In order to prove that  $C^*$  is the complex conjugate of  $C$ , we first expand the terms in  $C$ :

$$\begin{aligned} F_0F_+^* &= F(\omega_0)e^{i\omega_0t}F^*(\omega_0 + \Omega)e^{-i\omega_0t-i\Omega t} \\ &= F(\omega_0)F^*(\omega_0 + \Omega)e^{-i\Omega t} \\ F_0^*F_- &= F^*(\omega_0)e^{-i\omega_0t}F(\omega_0 - \Omega)e^{i\omega_0t-i\Omega t} \\ &= F^*(\omega_0)F(\omega_0 - \Omega)e^{-i\Omega t}. \end{aligned}$$

Next, we expand the terms in  $C^*$ :

$$\begin{aligned}
 F_0^* F_+ &= F^*(\omega_0) e^{-i\omega_0 t} F(\omega_0 + \Omega) e^{i\omega_0 t + i\Omega t} \\
 &= F^*(\omega_0) F(\omega_0 + \Omega) e^{i\Omega t} \\
 F_0 F_-^* &= F(\omega_0) e^{i\omega_0 t} F^*(\omega_0 - \Omega) e^{-i\omega_0 t + i\Omega t} \\
 &= F(\omega_0) F^*(\omega_0 - \Omega) e^{i\Omega t}.
 \end{aligned}$$

It is clear that the exponential terms in  $C^*$  are simply complex conjugates of the exponential terms in  $C$ . We can treat  $C$  and  $C^*$  as follows

$$\begin{aligned}
 C + C^* &= \left( \text{Re}(C) + \text{Im}(C) \right) + \left( \text{Re}(C) - \text{Im}(C) \right) = 2\text{Re}(C) \\
 &= 2\text{Re}([F_0 F_+] - [F_0^* F_-]) \\
 &= 2\text{Re} \left\{ \left( [F(\omega) F^*(\omega + \Omega)] - [F^*(\omega) F(\omega - \Omega)] \right) e^{-i\Omega t} \right\}. \tag{B.7}
 \end{aligned}$$

We can also use the relation

$$C e^{-i\Omega t} = \text{Re}[C] \cos(\Omega t) + \text{Im}[C] \sin(\Omega t),$$

allowing us to rewrite Equation (B.7) as

$$\begin{aligned}
 C + C^* &= 2 \left\{ \text{Re} \left[ F(\omega) F^*(\omega_0 + \Omega) - F^*(\omega_0) F(\omega_0 - \Omega) \right] \cos(\Omega t) \right. \\
 &\quad \left. + \text{Im} \left[ F(\omega_0) F^*(\omega_0 + \Omega) - F^*(\omega_0) F(\omega_0 - \Omega) \right] \sin(\Omega t) \right\}.
 \end{aligned}$$



Substituting for  $C + C^*$ , and for  $F_0$ ,  $F_+$  and  $F_-$ , Equation (B.6) now becomes:

$$\begin{aligned}
 E^* E &= |F(\omega_0)|^2 + |F(\omega_0 + \Omega)|^2 + |F(\omega_0 - \Omega)|^2 \\
 &+ 2 \left\{ \text{Re} \left[ F(\omega_0) F^*(\omega_0 + \Omega) - F^*(\omega_0) F(\omega_0 - \Omega) \right] \cos(\Omega t) \right. \\
 &+ \left. \text{Im} \left[ F(\omega_0) F^*(\omega_0 + \Omega) - F^*(\omega_0) F(\omega_0 - \Omega) \right] \sin(\Omega t) \right\} \\
 &+ (2\Omega \text{ terms}).
 \end{aligned} \tag{B.8}$$

Finally, we introduce the factors corresponding to the carrier and sideband powers,  $P_c$  and  $P_s$  respectively, and obtain the following expression for the power in the reflected beam (as detected by the  $\text{PD}_{ref}$ ):

$$\begin{aligned}
 P_{ref} &= P_c |F(\omega_0)|^2 + P_s \{ |F(\omega_0 + \Omega)|^2 + |F(\omega_0 - \Omega)|^2 \} \\
 &+ 2\sqrt{P_c P_s} \left\{ \text{Re} \left[ F(\omega_0) F^*(\omega_0 + \Omega) - F^*(\omega_0) F(\omega_0 - \Omega) \right] \cos(\Omega t) \right. \\
 &+ \left. \text{Im} \left[ F(\omega_0) F^*(\omega_0 + \Omega) - F^*(\omega_0) F(\omega_0 - \Omega) \right] \sin(\Omega t) \right\} \\
 &+ (2\Omega \text{ terms}).
 \end{aligned} \tag{B.9}$$

In other words, we are left with three fields at different frequencies: the carrier ( $\omega_0$ ) and the two sidebands ( $\omega_0 \pm \Omega$ ). When combined, the outcome is a wave with an apparent frequency of  $\omega_0$ , but is contained within an envelope with a beat pattern at two frequencies. The reflected power in Equation (B.9) contains three important frequency components: the carrier results in direct current (DC) power, the interference between the carrier and the sidebands produce the sine and cosine terms which oscillate at the modulation frequency ( $\Omega$ ), and lastly the sidebands interfering with each other to yield the ‘ $2\Omega$ ’ terms (higher-order components).







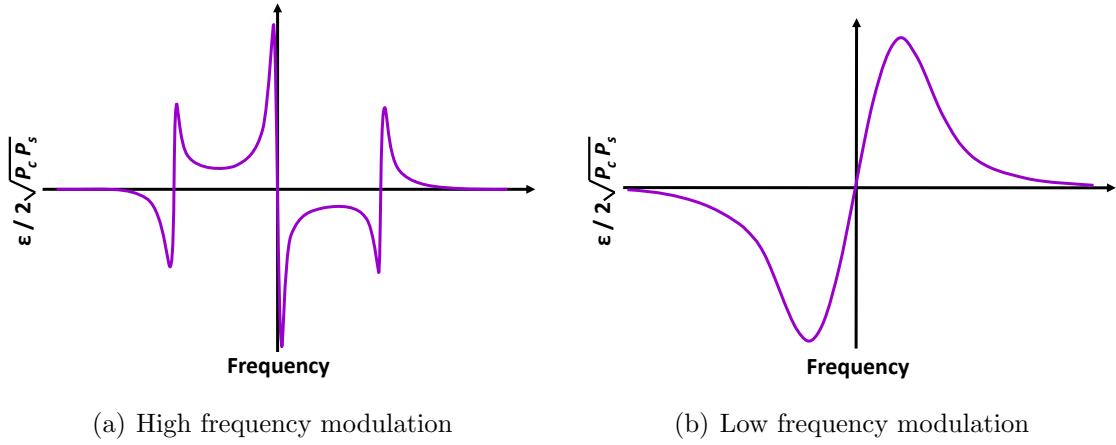


Figure B.2.: The Pound-Drever-Hall error signal,  $\varepsilon/2\sqrt{P_c P_s}$ , versus frequency for a Fabry-Perot cavity at (a) high modulation frequency, and (b) low modulation frequency. The cavity is assumed to be lossless with identical mirrors, and the cavity finesse is  $\sim 500$ .

## **Appendix C.**

### **Electronic schematics for the servo**

The electronics for the feedback control systems were produced at the University of Birmingham. The servo was built by the author using the specifications shown in Figures C.1 to C.4. Circuit board schematics were adopted from designs by H. Vahlbruch and B. Hage at the AEI Max Planck Institute for Gravitational Physics in Hannover, Germany.



## Appendix C. Electronic schematics for the servo

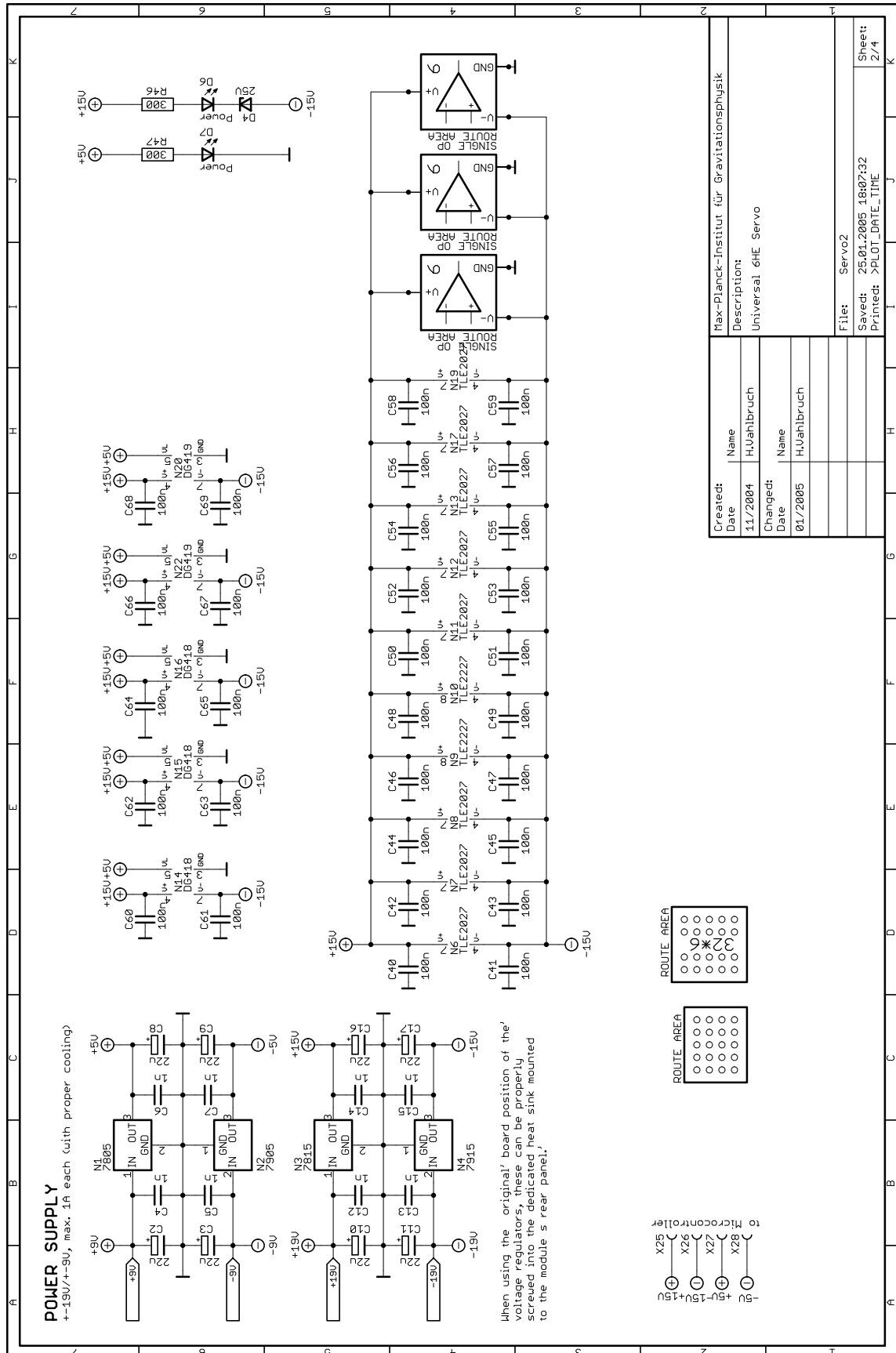


Figure C 2: Servo schematic 2/4  
Figure 2: Project circuit diagram (sheet 2)



164

**Figure 4:** Project circuit diagram (sheet 4)

## Appendix D.

# Parameter computation using the sagitta

Following on from Section 4.2.1, we will show how the radius of curvature,  $R_C$ , and the beam spot radius,  $\omega(z)$ , for a 0th diffraction order beam can lead to expressions describing the distance of the waist position from the grating,  $z'$ , and the waist size,  $\omega'_0$ , for a beam in the 1st diffraction order. For the purpose of this computation, primed parameters refer to the diffracted beam. Note that we consider all parameter descriptions *at the grating* i.e.  $z$  is at the grating position.

### Defining the sagitta

First we look at the relationship between the radius of curvature, the radius of the beam spot and the sagitta. Circle geometry is used to treat the curvature of a Gaussian wavefront [104], as depicted in Figure D.1. Each wavefront is considered to be part of a circle with a radius,  $R_C$ , the sagitta,  $s$ , and the semi-chord length which is in fact the radius of the beam spot,  $\omega(z)$ . The sagitta of the wavefront of

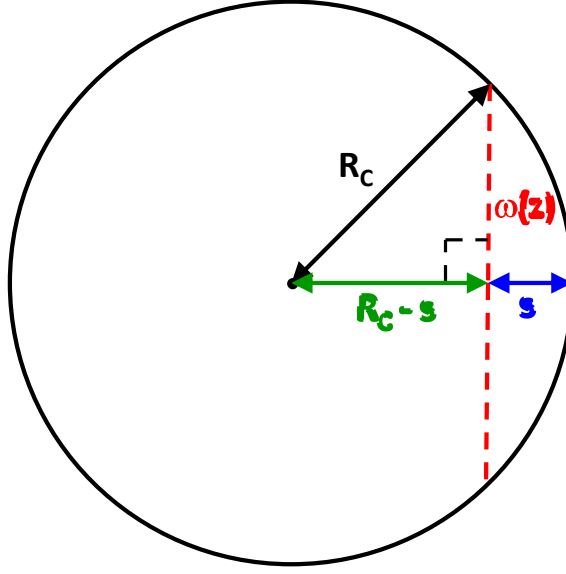


Figure D.1.: The radius of curvature,  $R_C$ , of a Gaussian beam wavefront can be defined in terms of its sagitta,  $s$ , (blue) and the beam spot radius,  $\omega(z)$ , (solid red).

both the incident and diffracted beams at point  $z$  always remain the same, ensuring that the frequency of the beam is preserved. From Figure D.1 we can define the radius of curvature as  $R_C = s + (R_C - s)$ , and simple trigonometry gives:

$$\begin{aligned}
 R_C^2 &= \omega(z)^2 + (R_C - s)^2 \\
 &= \omega(z)^2 + R_C^2 - 2R_C s + s^2 \\
 0 &= \omega(z)^2 - 2R_C s + s^2.
 \end{aligned} \tag{D.1}$$

Using the quadratic equation, we obtain the following solution for  $s$ :

$$\begin{aligned}
 s &= \frac{2R_C \pm \sqrt{(-2R_C)^2 - 4\omega(z)^2}}{2} \\
 &= \frac{2R_C \pm \sqrt{4R_C^2 - 4\omega(z)^2}}{2} \\
 &= R_C \pm \sqrt{R_C^2 - \omega(z)^2}.
 \end{aligned} \tag{D.2}$$

The negative solution of Equation (D.2) corresponds to the sagitta (the positive solution is the distance from the chord to the opposite side of the circle). Hence the sagitta is given by:

$$s = R_C - \sqrt{R_C^2 - \omega(z)^2}, \quad (\text{D.3})$$

and rearranging for  $R_C$  gives:

$$R_C = \frac{\omega(z)^2 + s^2}{2s}. \quad (\text{D.4})$$

### Beam spot radius in the diffracted beam

We can determine the beam spot radius of the diffracted beam,  $\omega'(z)$ , at the grating if we know the following: beam spot radius of the incident beam,  $\omega(z)$  (at the grating), the angle of incidence,  $\alpha$ , and the angle of diffraction,  $\beta$  (where both angles are measured from the grating normal). In the case of the simulation (Chapter 4),  $\alpha = 0^\circ$  and  $\beta = 45^\circ$ . We also have the following relation between  $\omega'(z)$  and  $\omega(z)$ :

$$\omega'(z) = \omega(z) \left( \frac{\cos \beta}{\cos \alpha} \right). \quad (\text{D.5})$$

### Radius of curvature in the diffracted beam

Since the sagitta remains the same for both the incident and diffracted beam, we can use Equation (D.4) to determine the radius of curvature in the reflected beam,  $R'_C$ , at the grating as:

$$R'_C = \frac{\omega'(z)^2 + s^2}{2s}. \quad (\text{D.6})$$

Substituting for  $\omega'(z)$  from Equation (D.5), we can rewrite this expression as:

$$R'_C = \frac{\omega^2(z) \left( \frac{\cos \beta}{\cos \alpha} \right)^2 + s^2}{2s}. \quad (\text{D.7})$$

### Waist position in the diffracted beam

We now derive an expression for the waist position,  $z'$ , for the diffracted beam - this is the distance of the diffracted beam's waist,  $\omega'_0$ , from the grating. We assume that the waist position is such that  $z_0 = 0$ .

The waist radius of the incident beam is:

$$\omega_0 = \sqrt{\left( \frac{z_R \lambda}{\pi} \right)}. \quad (\text{D.8})$$

Using the relationship between the waist size and spot size, and substituting for  $\omega_0$  gives:

$$\begin{aligned} \omega &= \omega_0 \sqrt{1 + \frac{z^2}{z_R^2}} \\ &= \sqrt{\left( \frac{z_R \lambda}{\pi} \right) \left( 1 + \frac{z^2}{z_R^2} \right)} \\ &= \sqrt{\frac{\lambda}{\pi z_R} (z_R^2 + z^2)}, \end{aligned} \quad (\text{D.9})$$

which can be rearranged to

$$\frac{\omega^2 \pi z_R}{\lambda} = z_R^2 + z^2. \quad (\text{D.10})$$

Using the equations  $R_C z = z_R^2 + z^2$  and  $z_R = \sqrt{R_C z - z^2}$ , we can substitute as follows:

$$\frac{\omega^2 \pi}{\lambda} \sqrt{R_C z - z^2} = R_C z. \quad (\text{D.11})$$

Squaring both sides and rearranging the  $\lambda$  term gives:

$$\begin{aligned} (\omega^2 \pi)^2 (R_C z - z^2) &= R_C^2 \lambda^2 z^2 \\ (\omega^2 \pi)^2 R_C - (\omega^2 \pi)^2 z &= R_C^2 \lambda^2 z \\ (\omega^2 \pi)^2 R_C &= z (R_C^2 \lambda^2 + (\omega^2 \pi)^2). \end{aligned} \quad (\text{D.12})$$

Since we are considering the diffracted beam, the parameters  $\omega$ ,  $R_C$  and  $z$  are designated as  $\omega'$ ,  $R'_C$  and  $z'$  and we are left with the following solution to describe the distance of the waist from the grating:

$$\boxed{z' = \frac{(\omega'^2 \pi)^2 R'_C}{R'^2_C \lambda^2 + (\omega'^2 \pi)^2}}. \quad (\text{D.13})$$

### Waist size of the diffracted beam

The waist size of the diffracted beam,  $\omega'_0$ , can now be computed by using the parameters  $z'$ ,  $R'_C$  and  $\omega'$ . We know that:

$$R'_C z' = \frac{\omega'^2(z) \pi z'_R}{\lambda}. \quad (\text{D.14})$$

We use the definition for the Rayleigh range:

$$z'_R = \frac{\omega_0'^2 \pi}{\lambda}, \quad (\text{D.15})$$

and substitute for  $z'_R$  in Equation (D.14), giving:

$$R'_C z' = \frac{\omega'^2 \pi}{\lambda} \frac{\omega_0'^2 \pi}{\lambda}. \quad (\text{D.16})$$

Rearranging for  $\omega_0'$ , it follows that:

$$\omega_0'^2 = \frac{R'_C z' \lambda^2}{\omega'^2 \pi^2}, \quad (\text{D.17})$$

and we obtain the expression:

$$\boxed{\omega_0' = \frac{\lambda}{\omega' \pi} \sqrt{R'_C z'}}. \quad (\text{D.18})$$

If  $z'$  is unknown, we can compute  $\omega_0'$  in terms of only  $\omega'$  and  $R'_C$  by substituting for  $z'$  from Equation (D.13):

$$\begin{aligned} \omega_0' &= \frac{\lambda}{\omega' \pi} \sqrt{\frac{R_C'^2 (\omega'^2 \pi)^2}{(R_C'^2 \lambda^2 + (\omega'^2 \pi)^2)}} \\ &= \frac{\lambda R'_C}{\omega' \pi} \frac{(\omega'^2 \pi)}{\sqrt{(R_C'^2 \lambda^2 + (\omega'^2 \pi)^2)}}. \end{aligned} \quad (\text{D.19})$$



The solution for the waist radius of the diffracted beam becomes:

$$\omega'_0 = \frac{\omega' \lambda R'_C}{\left(R'^2_C \lambda^2 + (\omega'^2 \pi)^2\right)^{\frac{1}{2}}}. \quad (\text{D.20})$$

## **Appendix E.**

# **BOSEM testing and distribution**

### **E.1. Cross-section of the magnetic-mounted flag**

Shown here is a CAD drawing depicting the cross-section of the magnetic-mounted flag, proposed for Advanced LIGO in replacement of the Vacseal-mounted flags from Initial LIGO (see Section 6.2). The flag comprises of a hexagonal head screw, magnet, flag rod and two magnetic plugs (each inserted within the screw and flag rod).

This technical note was produced by Ian Wilmut, Rutherford Appleton Laboratories, on behalf of the Suspensions Working Group for Advanced LIGO.



## **E.2. BOSEM count**

Figure E.1 displays a count of BOSEMs which were due to be delivered by the University of Birmingham (see Section 6.3). The acronyms represent various divisions of the Advanced LIGO detectors in which the BOSEMs would be installed: BSC (beamsplitter chamber), HAM (horizontal access module), ITM (input test mass), CP (compensation plate), FM (folding mirror), ETM (end test mass), BS (beamsplitter), RM (recycling mirror), IMC (input modecleaner), OMC (output modecleaner), NP (noise prototypes), and Aux (Auxiliary Optics). Some noise prototypes remained in the UK and were also delivered to LASTI (LIGO Advanced System Test Interferometer) at the Massachusetts Institute of Technology for testing purposes. Note that LIGO-1 OSEMs refer to the original OSEMS used in Initial LIGO.

Figure E.1 was taken from the technical note in [105], produced by Justin Greenhalgh, Rutherford Appleton Laboratories, on behalf of the Suspensions Working Group for Advanced LIGO.

Table 2. Count of OSEMs.																							
OSEMs which are to be provided by LIGO labs are included only to allow calculation of channel numbers for electronics																							
BSC										HAM										Total			
ITM + CP		FM	ETM	Noise prot		BS		RM	IMC	OMC	RM	IMC	OMC	Aux NP	Aux NP	Aux NP	Bham	LIGO	Gla + Bham	Overall			
				LASTI		UK																	
production sus qty		6	2	6	1	1	3	6	9	3	3	1	1	2	4	30							
spare sus qty		2	1	2			1	3	3	3						0							
B-OSEMs		16	10	16	16	6	10	6	6	6	6	6	6	6	4	0							
LIGO-1 OSEMs		4	0	4	4	1	0	8	8	0	8	8	8	0	5	5							
B-OSEMs		128	30	128	16	6	40	54	72	36	6	6	12	16	0								
LIGO-1 OSEMs		32	0	32	4	1	0	72	96	0	8	8	0	20	150								
Spares level (hybrid)		20%	20%	20%	20%	20%	33%	33%	33%	33%	33%	33%	20%	20%	20%								
Spare level (LIGO 1)		20%	20%	20%	20%	20%	20%	20%	20%	20%	20%	20%	20%	20%	20%								
B-OSEMs		154	36	154	20	8	48	72	96	48	8	8	15	20	0								
LIGO-1 OSEMs		39	0	39	5	2	0	87	116	0	10	10	0	24	180								
Total numbers																	without spares						
																	62	0	488	550			
																	0	423	0	423			
Total numbers with system spares																	with spares						
																	79	0	608	687			
																	0	512	0	512			
Key		Black	RAL																				
		Blue	Birmingham																				
		Red	LIGO Labs																				
UK provides these Electronics channels (no spares shown here; see table 3)																							
ETM/ITM				BOSEM		278		total quad		347													
				LIGO1		69																	
FM/BS				BOSEM		70		total triple		476													
				LIGO1		0																	
HAM				BOSEM		202																	
				LIGO1		204																	
Aux (not UK)				LIGO1		150																	
Note on OSEM deliverables																							
The UK will be supplying a total of 654 OSEMs as per version C of this document.																							

Figure E.1.: Table to show the number of BOSEMs due to be delivered for installation in the Advanced LIGO detectors [105].

© 2006 The Authors  
Journal compilation © 2006 Blackwell Publishing Ltd

Response	Percentage
Yes	85%
No	15%

Responsibility	Percentage
Current government	85%
Previous government	10%
Neither	5%







# Bibliography

- [1] E.D. Black. An introduction to pound–drever–hall laser frequency stabilization. *American Journal of Physics*, 69:79, 2001. , 78
- [2] Allen Wyatt. Importing multiple files to a single workbook. ”[http://excel.tips.net/T003148\\_Importing\\_Multiple\\_Files\\_to\\_a\\_Single\\_Workbook.html](http://excel.tips.net/T003148_Importing_Multiple_Files_to_a_Single_Workbook.html)”. , 177
- [3] A. Einstein. Die grundlage der allgemeinen relativitätstheorie. *Annalen der Physik*, 354(7):769–822, 1916. 1
- [4] RA Hulse and JH Taylor. Discovery of a pulsar in a binary system. *The Astrophysical Journal*, 195:L51–L53, 1975. 1
- [5] C.W. Misner, K.S. Thorne, and J.A. Wheeler. *Gravitation*, volume 1. 1973. 4
- [6] Jordan B Camp and Neil J Cornish. Gravitational wave astronomy\*. *Annu. Rev. Nucl. Part. Sci.*, 54:525–577, 2004. 4
- [7] B.F. Schutz. Gravitational waves on the back of an envelope. *American Journal of Physics*, 52:412–419, 1984. 4
- [8] P. R. Saulson. *Fundamentals of interferometric gravitational wave detectors*.

- World Scientific, 1994. 4, 10, 18, 21
- [9] BS Sathyaprakash and B.F. Schutz. Physics, astrophysics and cosmology with gravitational waves. *Living Rev. Relativity*, 12(2), 2009. 4
  - [10] L.P. Grishchuk, VM Lipunov, K.A. Postnov, M.E. Prokhorov, and BS Sathyaprakash. Gravitational wave astronomy: in anticipation of first sources to be detected. *Physics-Uspekhi*, 44:1, 2001. 5
  - [11] Bernard Schutz. *A First Course in General Relativity*. Cambridge University Press, Second edition, 2009. 5, 6
  - [12] LIGO. Ligo scientific collaboration. <http://www.ligo.org/science/GW-Stochastic.php>. 6
  - [13] M.P. Edgar. *Experimental investigations into diffractive optics and optomechanical systems for future gravitational wave detectors*. PhD thesis, University of Glasgow, 2011. 6
  - [14] M. Pitkin, S. Reid, S. Rowan, and J. Hough. Gravitational wave detection by interferometry (ground and space). *Living Reviews in Relativity*, 14(5), 2011. 7, 11, 12, 20
  - [15] B. Willke, N. Uehara, EK Gustafson, RL Byer, PJ King, SU Seel, RL Savage Jr, et al. Spatial and temporal filtering of a 10-w nd: Yag laser with a fabry-perot ring-cavity premode cleaner. *Optics letters*, 23(21):1704–1706, 1998. 8
  - [16] Virgo. Advanced virgo baseline design. *Virgo document number VIR-0027A-09* (*Virgo documents can be accessed via the Virgo technical documentation system: <https://tds.ego-gw.it/>*), 2009. 12

- [17] T. Accadia, F. Acernese, F. Antonucci, P. Astone, G. Ballardin, F. Barone, M. Barsuglia, A. Basti, T.S. Bauer, M. Bebronne, et al. Status of the virgo project. *Classical and Quantum Gravity*, 28:114002, 2011. 12
- [18] B. Willke, P. Aufmuth, C. Aulbert, S. Babak, R. Balasubramanian, BW Barr, S. Berukoff, S. Bose, G. Cagnoli, M.M. Casey, et al. The geo 600 gravitational wave detector. *Classical and Quantum Gravity*, 19:1377, 2002. 12
- [19] H. Grote. The status of geo 600. *Classical and Quantum Gravity*, 25:114043, 2008. 12
- [20] S. Miyoki. Large scale cryogenic gravitational wave telescope. *Nuclear Physics B-Proceedings Supplements*, 138:439–442, 2005. 12
- [21] K. Kuroda. Status of lgt. *Classical and Quantum Gravity*, 27:084004, 2010. 12, 13
- [22] JR Smith and L.S. Collaboration. The path to the enhanced and advanced ligo gravitational-wave detectors. *Classical and Quantum Gravity*, 26(11):4013, 2009. 12
- [23] J. Marx, K. Danzmann, J. Hough, K. Kuroda, D. McClelland, B. Mours, S. Phinney, S. Rowan, B. Sathyaprakash, F. Vetrano, et al. The gravitational wave international committee roadmap: The future of gravitational wave astronomy. 2011. 13
- [24] LIGO Scientific Collaboration, Virgo Collaboration, J Aasi, J Abadie, BP Abbott, R Abbott, TD Abbott, M Abernathy, T Accadia, F Acernese, et al. Prospects for localization of gravitational wave transients by the advanced ligo and advanced virgo observatories. *arXiv preprint arXiv:1304.0670*, 2013.

- 13, 16
- [25] Indigo. <http://www.gw-indigo.org/>. 13
- [26] G. Losurdo. Ground-based gravitational wave interferometric detectors of the first and second generation: an overview. *Classical and Quantum Gravity*, 29(12):124005, 2012. 13
- [27] G.M. Harry. Advanced ligo: the next generation of gravitational wave detectors. *Classical and Quantum Gravity*, 27:084006, 2010. 13, 17, 25, 119, 121
- [28] D. Shoemaker. Advanced ligo reference design. Technical report, M060056-v2, 2009. 13, 14, 19
- [29] S. Sunil and DG Blair. Vacuum system requirement for a 5 km baseline of gravitational-wave detector. In *Journal of Physics Conference Series*, volume 114, page 2025, 2008. 14
- [30] T.T. Fricke, N.D. Smith-Lefebvre, R. Abbott, R. Adhikari, K.L. Dooley, M. Evans, P. Fritschel, V.V. Frolov, K. Kawabe, J.S. Kissel, et al. Dc readout experiment in enhanced ligo. *Classical and Quantum Gravity*, 29:065005, 2012. 15
- [31] H. Vahlbruch, S. Chelkowski, B. Hage, A. Franzen, K. Danzmann, and R. Schnabel. Demonstration of a squeezed-light-enhanced power-and signal-recycled michelson interferometer. *Physical review letters*, 95(21):211102, 2005. 15
- [32] C. Zhao, J. Degallaix, L. Ju, Y. Fan, D.G. Blair, BJJ Slagmolen, M.B. Gray, C.M.M. Lowry, DE McClelland, DJ Hosken, et al. Compensation of

- strong thermal lensing in high-optical-power cavities. *Physical review letters*, 96(23):231101, 2006. 15, 27, 30
- [33] L. Carbone, SM Aston, RM Cutler, A. Freise, J. Greenhalgh, J. Heefner, D. Hoyland, NA Lockerbie, D. Lodhia, NA Robertson, et al. Sensors and actuators for the advanced ligo mirror suspensions. *Classical and Quantum Gravity*, 29(11):115005, 2012. 15, 19, 122, 124
- [34] N.A. Robertson, M. Barton, G. Cagnoli, C.A. Cantley, D. Coyne, D. Crooks, E. Elliffe, P. Fritschel, S. Goßler, A. Grant, A. Heptonstall, J. Hough, et al. Advanced ligo suspension system conceptual design. Technical report, T010103-04-D, 2005. 15, 120
- [35] Frederick J Raab. Overview of ligo instrumentation. In *Astronomical Telescopes and Instrumentation*, pages 11–24. International Society for Optics and Photonics, 2004. 16
- [36] L.S. Finn. Gravitational wave interferometer noise calculator. <http://gwastro.org/>, 1997. 16
- [37] N. Mavalvala, N.R. Hunter-Jones, et al. *Novel approaches to Newtonian noise suppression in interferometric gravitational wave detection*. PhD thesis, Massachusetts Institute of Technology, 2011. 18, 19
- [38] N.A. Robertson, B. Abbott, R. Abbott, R. Adhikari, G.S. Allen, H. Armandula, S.M. Aston, A. Baglino, M. Barton, B. Bland, et al. Seismic isolation and suspension systems for advanced ligo. In *Society of Photo-Optical Instrumentation Engineers (SPIE) Conference Series*, volume 5500, pages 81–91, 2004. 19, 119

- [39] MG Beker, G. Cella, R. DeSalvo, M. Doets, H. Grote, J. Harms, E. Hennes, V. Mandic, DS Rabeling, J.F.J. van den Brand, et al. Improving the sensitivity of future gw observatories in the 1–10 hz band: Newtonian and seismic noise. *General Relativity and Gravitation*, 43(2):623–656, 2011. 19, 20
- [40] J. Harms, R. DeSalvo, S. Dorsher, and V. Mandic. Simulation of underground gravity gradients from stochastic seismic fields. *Physical Review D*, 80(12):122001, 2009. 20
- [41] A. Buonanno and Y. Chen. Quantum noise in second generation, signal-recycled laser interferometric gravitational-wave detectors. *Physical Review D*, 64(4):042006, 2001. 20
- [42] G. Lovelace. The dependence of test-mass coating and substrate thermal noise on beam shape in the advanced Laser Interferometer Gravitational-Wave Observatory (advanced LIGO). *Arxiv preprint gr-qc/0610041*, 2006. 22
- [43] M. Evans, S. Ballmer, M. Fejer, P. Fritschel, G. Harry, and G. Ogin. Thermo-optic noise in coated mirrors for high-precision optical measurements. *Physical Review D*, 78(10):102003, 2008. 23
- [44] T. Tomaru, T. Suzuki, T. Uchiyama, A. Yamamoto, T. Shintomi, CT Taylor, K. Yamamoto, S. Miyoki, M. Ohashi, and K. Kuroda. Maximum heat transfer along a sapphire suspension fiber for a cryogenic interferometric gravitational wave detector. *Physics Letters A*, 301(3-4):215–219, 2002. 23
- [45] M. Punturo, M. Abernathy, F. Acernese, B. Allen, N. Andersson, K. Arun, F. Barone, B. Barr, M. Barsuglia, M. Beker, et al. The einstein telescope: a third-generation gravitational wave observatory. *Classical and Quantum Gravity*, 27:194002, 2010. 23

- [46] Y. Levin. Internal thermal noise in the LIGO test masses: A direct approach. *Physical Review D*, 57(2):659, 1998. 23
- [47] H.B. Callen and R.F. Greene. On a theorem of irreversible thermodynamics. *Physical Review*, 86:702–710, 1952. 24
- [48] E.C. Chalkley. Investigations of the properties of materials for the optics and suspensions of future gravitational wave detectors. 2010. 24
- [49] P.R. Saulson et al. Thermal noise in mechanical experiments. *Physical Review D*, 42(8):2437–2445, 1990. 24
- [50] G.M. Harry, A.M. Gretarsson, P.R. Saulson, S.E. Kittelberger, S.D. Penn, W.J. Startin, S. Rowan, M.M. Fejer, DRM Crooks, G. Cagnoli, et al. Thermal noise in interferometric gravitational wave detectors due to dielectric optical coatings. *Classical and Quantum Gravity*, 19:897, 2002. 25
- [51] P. Fulda, K. Kokeyama, S. Chelkowski, and A. Freise. Experimental demonstration of higher-order laguerre-gauss mode interferometry. *Physical Review D*, 82(1):012002, 2010. 25
- [52] F.Y. Khalili. Reducing the mirrors coating noise in laser gravitational-wave antennae by means of double mirrors. *Physics Letters A*, 334(1):67–72, 2005. 25
- [53] A. Bunkowski, O. Burmeister, D. Friedrich, K. Danzmann, and R. Schnabel. High reflectivity grating waveguide coatings for 1064 nm. *Classical and Quantum Gravity*, 23:7297, 2006. 25
- [54] E.D. Black, A. Villar, and K.G. Libbrecht. Thermoelastic-damping noise from sapphire mirrors in a fundamental-noise-limited interferometer. *Physical re-*

- view letters*, 93(24):241101, 2004. 25
- [55] HLL Châtelier. A general statement of the laws of chemical equilibrium. *Comptes rendus*, 99:786–789, 1884. 25
- [56] VB Braginsky, ML Gorodetsky, and SP Vyatchanin. Thermo-refractive noise in gravitational wave antennae. *Physics Letters A*, 271:303–307, 2000. 26
- [57] H.J. Kimble, B.L. Lev, and J. Ye. Optical interferometers with reduced sensitivity to thermal noise. *Physical Review Letters*, 101(26):260602, 2008. 27
- [58] M.L. Gorodetsky. Thermal noises and noise compensation in high-reflection multilayer coating. *Physics Letters A*, 372(46):6813–6822, 2008. 27
- [59] W. Winkler, K. Danzmann, A. Ruediger, and R. Schilling. Heating by optical absorption and the performance of interferometric gravitational-wave detectors. *Physical Review A*, 44(11):7022–7036, 1991. 28, 29
- [60] K.A. Strain, K. Danzmann, J. Mizuno, PG Nelson, A. Rüdiger, R. Schilling, and W. Winkler. Thermal lensing in recycling interferometric gravitational wave detectors. *Physics Letters A*, 194(1):124–132, 1994. 28, 30
- [61] W. Winkler, A. Rüdiger, R. Schilling, K.A. Strain, and K. Danzmann. Birefringence-induced losses in interferometers. *Optics communications*, 112(5-6):245–252, 1994. 30
- [62] P. Hello and J.Y. Vinet. Simulation of thermal effects in interferometric gravitational-wave detectors. *Physics Letters A*, 178(5):351–356, 1993. 30
- [63] R.C. Lawrence. *Active Wavefront Correction in Laser Interferometric Gravitational Wave Detectors*. PhD thesis, Massachusetts Institute of Technology,



2003. 30

- [64] D. Friedrich, O. Burmeister, A. Bunkowski, T. Clausnitzer, S. Fahr, E.B. Kley, A. Tünnermann, K. Danzmann, and R. Schnabel. Diffractive beam splitter characterization via a power-recycled interferometer. *Optics letters*, 33(2):101–103, 2008. 30
- [65] Stefan Hild, Harald Lück, Walter Winkler, Ken Strain, Hartmut Grote, Joshua Smith, Michaela Malec, Martin Hewitson, Benno Willke, James Hough, et al. Measurement of a low-absorption sample of oh-reduced fused silica. *Applied optics*, 45(28):7269–7272, 2006. 30
- [66] K.X. Sun and R.L. Byer. All-reflective Michelson, Sagnac, and Fabry–Perot interferometers based on grating beam splitters. *Optics letters*, 23(8):567–569, 1998. 30, 33
- [67] A. Bunkowski, O. Burmeister, P. Beyersdorf, K. Danzmann, R. Schnabel, T. Clausnitzer, E.B. Kley, and A. Tünnermann. Low-loss grating for coupling to a high-finesse cavity. *Optics letters*, 29(20):2342–2344, 2004. 30, 31
- [68] J. Franc, N. Morgado, R. Flaminio, R. Nawrodt, I. Martin, L. Cunningham, A. Cumming, S. Rowan, and J. Hough. Mirror thermal noise in laser interferometer gravitational wave detectors operating at room and cryogenic temperature. *Arxiv preprint arXiv:0912.0107*, 2009. 31
- [69] R Schnabel, M Britzger, F Brückner, O Burmeister, K Danzmann, J Duck, T Eberle, D Friedrich, H Luck, M Mehmet, et al. Building blocks for future detectors: Silicon test masses and 1550 nm laser light. In *Journal of Physics: Conference Series*, volume 228, page 012029. IOP Publishing, 2010. 31

- [70] BW Shore, MD Perry, JA Britten, RD Boyd, MD Feit, HT Nguyen, R. Chow, GE Loomis, and L. Li. Design of high-efficiency dielectric reflection gratings. *JOSA A*, 14(5):1124–1136, 1997. 31
- [71] F. Brückner. *Advanced mirror concepts for high-precision metrology*. PhD thesis, University of Jena, 2011. 32
- [72] RWP Drever. Concepts for extending the ultimate sensitivity of interferometric gravitational wave detectors using non-transmissive optics with diffractive or holographic coupling. In *Proceedings of the Seventh Marcel Grossman Meeting on recent developments in theoretical and experimental general relativity, gravitation, and relativistic field theories*, volume 1, page 1401, 1996. 33
- [73] S. Fahr, T. Clausnitzer, E.B. Kley, and A. Tünnermann. Reflective diffractive beam splitter for laser interferometers. *Applied optics*, 46(24):6092–6095, 2007. 33
- [74] R. Schnabel, A. Bunkowski, O. Burmeister, and K. Danzmann. Three-port beam splitters-combiners for interferometer applications. *Optics letters*, 31(5):658–660, 2006. 33
- [75] D. Friedrich, O. Burmeister, M. Britzger, A. Bunkowski, T. Clausnitzer, S. Fahr, E.B. Kley, A. Tünnermann, K. Danzmann, and R. Schnabel. Power-recycled michelson interferometer with a 50/50 grating beam splitter. In *Journal of Physics: Conference Series*, volume 122, page 012018. IOP Publishing, 2008. 33
- [76] S. Wise, V. Quetschke, AJ Deshpande, G. Mueller, DH Reitze, DB Tanner, BF Whiting, Y. Chen, A. Tünnermann, E. Kley, et al. Phase effects in the diffraction of light: Beyond the grating equation. *Physical review letters*,

- 95(1):13901, 2005. 35, 92
- [77] A. Freise, A. Bunkowski, and R. Schnabel. Phase and alignment noise in grating interferometers. *New Journal of Physics*, 9:433, 2007. 35, 36, 39
- [78] N. Mavalvala. *Alignment issues in laser interferometric gravitational-wave detectors*. PhD thesis, 1997. 39
- [79] A. Freise and K. Strain. Interferometer techniques for gravitational-wave detection. *Living Rev. Relativity*, 13, 2010. 39
- [80] Jonathan Mark Hallam. *Diffraction gratings in high-precision interferometry for gravitational wave detection*. PhD thesis, University of Birmingham, July 2011. 40, 41, 43
- [81] J. Hallam, S. Chelkowski, A. Freise, S. Hild, B. Barr, KA Strain, O. Burmeister, and R. Schnabel. Coupling of lateral grating displacement to the output ports of a diffractive fabry-perot cavity. *Journal of Optics A: Pure and Applied Optics*, 11:085502, 2009. 40, 42
- [82] A. Freise, G. Heinzl, H. Lück, R. Schilling, B. Willke, and K. Danzmann. Frequency-domain interferometer simulation with higher-order spatial modes. *Classical and Quantum Gravity*, 21:S1067, 2004. 44
- [83] D Lodhia, F Brückner, L Carbone, P Fulda, K Kokeyama, and A Freise. Phase effects in gaussian beams on diffraction gratings. In *Journal of Physics: Conference Series*, volume 363, page 012014. IOP Publishing, 2012. 45
- [84] Deepali Lodhia, Daniel Brown, Frank Brueckner, Ludovico Carbone, Paul Fulda, Keiko Kokeyama, and Andreas Freise. Phase effects due to beam misalignment on diffraction gratings. *Submitted to Optics Express*, also available

- at <http://arxiv.org/abs/1303.7016>, 2013. 45
- [85] Anthony E. Siegman. *Lasers*. University Science Books, 1st edition edition, 5 1986. 47
- [86] Bob Mellish. *Gaussianbeamwaist.svg*. ©, February 2009. 49
- [87] Andre Thüring and Nico Lastzka. Jammt - just another mode matching tool. "<http://www.sr.bham.ac.uk/dokuwiki/doku.php?id=geosim:jammt>". 70, 143
- [88] F. Brückner. Private communication, 2013. 71
- [89] RWP Drever, J.L. Hall, FV Kowalski, J. Hough, GM Ford, AJ Munley, and H. Ward. Laser phase and frequency stabilization using an optical resonator. *Applied Physics B: Lasers and Optics*, 31(2):97–105, 1983. 77
- [90] Allen Taflov and Susan C. Hagness. *Computational Electrodynamics: The Finite-Difference Time-Domain Method, Third Edition*. Artech House, 3 edition, 6 2005. 92
- [91] Daniel Brown. Finite-difference time-domain analysis of diffraction and waveguide coating displacement phase shifts. Msci 4th yr project, School of Physics & Astronomy, University of Birmingham, UK, April 2011. 92, 93, 94
- [92] Daniel Brown, Daniel Friedrich, Frank Brückner, Ludovico Carbone, Roman Schnabel, and Andreas Freise. Invariance of waveguide grating mirrors to lateral displacement phase shifts. *Submitted to Optics letters*, also available at <http://arxiv.org/abs/1303.0544>, 2013. 92
- [93] K. Yee. Numerical solution of initial boundary value problems involving

- maxwell's equations in isotropic media. *Antennas and Propagation, IEEE Transactions on*, 14(3):302–307, 1966. 93
- [94] Peter Fritschel. Second generation instruments for the laser interferometer gravitational wave observatory (ligo). In *Society of Photo-Optical Instrumentation Engineers (SPIE) Conference Series*, volume 4856, pages 282–291, 2003. 120
- [95] MV Plissi, CI Torrie, ME Husman, NA Robertson, KA Strain, H. Ward, H. Lück, and J. Hough. Geo 600 triple pendulum suspension system: Seismic isolation and control. *Review of scientific instruments*, 71:2539, 2000. 119
- [96] D. Shoemaker. Advanced ligo: Context and overview (proposal to the nsf). ligo document. Technical report, M030023-0-M, 2003. 119
- [97] SM Aston, MA Barton, AS Bell, N Beveridge, B Bland, AJ Brummitt, G Cagnoli, CA Cantley, L Carbone, AV Cumming, et al. Update on quadruple suspension design for advanced ligo. *Classical and Quantum Gravity*, 29(23):235004, 2012. 121
- [98] D. Bridges and J. Romie. Bosem, magnet (10mm x 10mm) and flag arrangement. Technical report, D1001794-v2, 2012. 123
- [99] S. Aston. Bosem design document & test report. Technical report, T050111-04-K, 2009. 124, 129, 133
- [100] D. Lodhia. Osem alternative magnetic flag mount test report. Technical report, T060017-00-K, 2006. 128
- [101] S. Aston and D. Lodhia. Bosem assembly specification. Technical report, T060233-03-K, 2008. 133, 137

## Bibliography

---

- [102] S. Aston and D. Lodhia. Bosem test specification. Technical report, T070107-07-K, 2012. 133, 134, 135, 136, 137, 138
- [103] S. Aston. *Optical Read-out Techniques for the Control of Test-masses in Gravitational Wave Observatories*. PhD thesis, University of Birmingham, 2011. 140, 141
- [104] Milton Katz. *Introduction to Geometrical Optics*. World Scientific Pub Co Inc, 1 edition, 4 2003. 166
- [105] J. Greenhalgh. Bosem uk scope document. Technical report, M030162-D-K, 2010. 175, 176